



Chair of Physical Metallurgy

Master's Thesis

Hydrogen embrittlement in steels: state-of-the-art in theory and practice



Maximilian Graf, BSc

December 2023



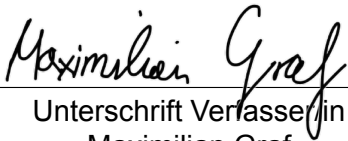
**EIDESSTÄTTLICHE ERKLÄRUNG**

Ich erkläre an Eides statt, dass ich diese Arbeit selbständig verfasst, andere als die angegebenen Quellen und Hilfsmittel nicht benutzt, und mich auch sonst keiner unerlaubten Hilfsmittel bedient habe.

Ich erkläre, dass ich die Richtlinien des Senats der Montanuniversität Leoben zu "Gute wissenschaftliche Praxis" gelesen, verstanden und befolgt habe.

Weiters erkläre ich, dass die elektronische und gedruckte Version der eingereichten wissenschaftlichen Abschlussarbeit formal und inhaltlich identisch sind.

Datum 20.12.2023



---

Unterschrift Verfasser/in  
Maximilian Graf



# Danksagung

Ich möchte mich bei Herrn Univ.-Prof. Dipl.-Ing. Dr. mont. Ronald Schnitzer für das Bereitstellen des Themas dieser Masterarbeit sowie für die Ratschläge und Korrekturen bedanken. Des Weiteren möchte ich mich für das Unterstützen meiner Interessen bei allen Firmenbesprechungen ganz herzlich bedanken.

Ganz besonders möchte ich mich bei Frau Dipl.-Ing. Dr. mont. Anna Jelinek und Herrn Dr. mont. Bak. fk. Oleksandr Glushko bedanken, die mich im Zuge dieser Masterarbeit stets nach bestem Wissen und Gewissen betreut haben. Vielen Dank für die äußerst wertvollen Anregungen und Gespräche und auch dafür, dass es während der gemeinsamen Zeit ständig ein äußerst kollegiales Umfeld sowie gegenseitige Wertschätzung gegeben hat. Weiters möchte ich mich bei Frau Dipl.-Ing. Dr. mont. Anna Jelinek für die großartige Unterstützung bei der Durchführung der Experimente bedanken.

Ganz besonders möchte ich mich auch bei Herrn Dipl.-Ing. Andreas Rosenauer für das Bereitstellen der Proben und der dazugehörigen Daten sowie für die vielen anregenden Gespräche und Ratschläge im Laufe der experimentellen Arbeit bedanken.

Ich möchte mich ganz herzlich bei Herrn Ing. AR Bruno Krajnc für die wertvolle Unterstützung bei der Durchführung der Zugversuche, die vielen anregenden Gespräche sowie die guten Ideen und deren schnelle Durchführung bei der experimentellen Arbeit bedanken.

Ebenfalls möchte ich mich bei Frau FOI Silvia Pölzl für die Anleitung und tatkräftige Unterstützung bei der Durchführung der Schiffe ganz herzlich bedanken.

Ich möchte mich bei meiner Oma, meinen Geschwistern Alex und Katrin, sowie bei Stefan, Konstantin und Cosma ganz herzlich bedanken, da sie mich stets unterstützt und motiviert haben, dieses Studium abzuschließen. Einen ganz besonderen Dank möchte ich an meine Mutter aussprechen, die mich mein ganzes Leben lang unterstützt hat, immer sehr stolz auf mich war und mir bei allen wichtigen Lebensentscheidungen mit gutem Rat zur Seite gestanden hat. Vielen Dank, dass du mir dieses Studium ermöglicht hast!

Zu guter Letzt möchte ich mich bei meinen Freunden bedanken, die meine Zeit in Leoben zu einer schönen und lustigen Erfahrung gemacht haben und mich sowohl akademisch als auch persönlich oft unterstützt haben.

# Kurzfassung

Um die enormen CO<sub>2</sub>-Emissionen bei der Eisen- und Stahlerzeugung zu reduzieren, wird in Zukunft die Direktreduktion von Eisenerz mit Wasserstoff angestrebt. Dies kann bei metallischen Bauteilen, die bei der Stahlherstellung mit Wasserstoff in Berührung kommen, zu einer Verschlechterung der mechanischen Eigenschaften führen, die als Wasserstoffversprödung bekannt ist. Um einen erfolgreichen Übergang von kohlenstoffhaltigen Reduktionsmitteln auf reinen Wasserstoff zu ermöglichen, werden Normen und Standards benötigt, die bei der Auslegung und Dimensionierung von Komponenten den schädigenden Einfluss von Wasserstoff auf metallische Bauteile berücksichtigen. Darüber hinaus werden Normen und Standards benötigt, die die Werkstoffprüfung von metallischen Proben in wasserstoffhaltigen Atmosphären standardisieren.

Im theoretischen Teil dieser Arbeit wurden dafür relevante Normen und Standards untersucht und die wichtigsten Punkte zusammengefasst. Des Weiteren wurden verschiedene Werkstoffprüfverfahren hinsichtlich ihrer Eignung zur Beurteilung des Werkstoffverhaltens unter Wasserstoffeinfluss analysiert. Darüber hinaus wurden verschiedene Stähle hinsichtlich der Verschlechterung ihrer mechanischen Eigenschaften unter Wasserstoffeinfluss untersucht. Im experimentellen Teil dieser Arbeit wurden Zugversuche an unbeladenen und mit Wasserstoff beladenen Proben durchgeführt, um den Einfluss von Wasserstoff auf einen martensitischen *PH13-8Mo* und auf einen austenitischen *AISI303* Stahl zu untersuchen. Die Zugproben wurden elektrochemisch mit Wasserstoff beladen und der Gesamtwasserstoffgehalt in den beladenen und unbeladenen Proben mittels Thermodesorptionsspektroskopie gemessen. Die Bruchflächen wurden mittels Stereo- und Rasterelektronenmikroskopie charakterisiert.

Eine ausgeprägte Anfälligkeit für Wasserstoffversprödung wurde für *PH13-8Mo* festgestellt, was hauptsächlich auf die hohe Festigkeit, die martensitische Matrix und den geringen Austenitgehalt zurückzuführen ist. Aufgrund eines unzureichenden Nickelgehalts und eines hohen Anteils an Mangansulfideinschlüssen konnte auch für *AISI303* eine hohe Anfälligkeit für Wasserstoffversprödung festgestellt werden. Der martensitische Stahl *PH13-8Mo* zeigte im Vergleich zum austenitischen Stahl *AISI303* eine deutlich höhere Wasserstoffdiffusionsrate, jedoch eine viel geringere Wasserstofflöslichkeit. Es konnte gezeigt werden, dass nur diffusionsfähige Wasserstoffatome zu Wasserstoffversprödung führen, da die nach der Beladung geglühten Proben das gleiche mechanische Verhalten wie die unbeladenen Proben zeigten.

# Abstract

In order to reduce the enormous CO<sub>2</sub> emissions in the iron and steel production, the direct reduction of iron ore with hydrogen will be targeted in the future. This results in an increased hydrogen content in the metal components exposed to hydrogen during steel production, which may lead to a deterioration of the mechanical properties of the structural metal components, known as hydrogen embrittlement. To enable a successful transition from carbon-containing reducing agents to pure hydrogen, codes and standards are required that take into account the detrimental effects of hydrogen on structural metals in the design and dimensioning of components. In addition, codes and standards are necessary to standardize the materials testing of metallic specimens in hydrogen-containing atmospheres.

In the theoretical part of this thesis, relevant codes and standards have been reviewed and the most important points have been summarized. Additionally, various materials testing methods have been evaluated for their suitability in assessing material behavior under the influence of hydrogen. Furthermore, various steels have been reviewed regarding their deterioration of mechanical properties under the influence of hydrogen. In the experimental part of this thesis, tensile tests were performed on uncharged and hydrogen-charged specimens to investigate the influence of hydrogen on a martensitic *PH13-8Mo* and an austenitic *AISI 303* steel. The tensile specimens were subjected to electrochemical hydrogen charging and the total hydrogen content in the charged and uncharged specimens was determined by thermal desorption spectroscopy. The fracture surfaces were characterized by stereo microscopy and scanning electron microscopy.

A pronounced sensitivity to hydrogen embrittlement was found for *PH13-8Mo* mainly due to its high strength, martensitic matrix and low austenite content. A high susceptibility to hydrogen embrittlement was also observed for *AISI 303*, mainly due to its insufficient nickel content and high fraction of manganese sulfide inclusions. Compared to the austenitic steel *AISI 303*, the martensitic steel *PH13-8Mo* showed a significantly higher hydrogen diffusion rate, but a lower hydrogen solubility. It has been shown that only diffusible hydrogen atoms lead to hydrogen embrittlement, since specimens, which were annealed after hydrogen charging exhibited the same mechanical behavior as uncharged specimens.

# List of abbreviations

AIDE	Adsorption-induced dislocation emission
API	American Petroleum Institute
BCC	Body-centered cubic
EAF	Elongation at fracture
EIGA	European Industrial Gases Association
FCC	Face-centered cubic
FEPA	Federation of European Producers of Abrasives
HAC	Hydrogen-assisted cracking
HCF	High cycle fatigue
HE	Hydrogen embrittlement
HEDE	Hydrogen-enhanced decohesion
HEE	Hydrogen environment embrittlement
HEI	Hydrogen embrittlement index
HELP	Hydrogen-enhanced localized plasticity
HESIV	Hydrogen-enhanced strain-induced vacancy generation
HMPF	Hydrogen material performance factor
HTHA	High temperature hydrogen attack
IHE	Internal hydrogen embrittlement
LCF	Low cycle fatigue
RNTS	Relative notched tensile strength
ROA	Reduction of area
RPI	Rate of pressure increase
SEM	Scanning electron microscope
SMYS	Specified minimum yield strength
TDS	Thermal desorption spectroscopy
TMHE	Temperature of maximum hydrogen embrittlement
UTS	Ultimate tensile strength

# Content

<b>1</b>	<b>Introduction</b>	<b>1</b>
<b>2</b>	<b>Theoretical background</b>	<b>3</b>
2.1	Hydrogen uptake	3
2.1.1	Adsorption	3
2.1.2	Solubility	5
2.2	Hydrogen mobility in metals	8
2.2.1	Basic diffusion principles of hydrogen in metals	8
2.2.2	Influence of trapping on the hydrogen mobility in metals	10
2.3	Hydrogen embrittlement mechanisms	12
2.3.1	Hydrogen-enhanced decohesion - HEDE	16
2.3.2	Hydrogen-enhanced local plasticity - HELP	17
2.3.3	Adsorption-induced dislocation emission - AIDE	18
2.3.4	Hydrogen-enhanced strain-induced vacancy mechanism - HESIV	18
2.4	Materials testing methods for hydrogen embrittlement	19
2.4.1	Tensile testing	20
2.4.2	Fracture mechanics testing	24
2.4.3	Fatigue testing	26
2.5	Codes and standards for hydrogen components	29
2.5.1	ASME B31.12	31
2.5.2	AD 2000 bulletin S2	35
2.5.3	European Industrial Gases Association guideline document	38
2.5.4	ASTM G142	39
2.5.5	ISO 11114-4	39
2.5.6	ANSI/CSA CHMC 1	40

<b>3</b>	<b>Methodological approach</b>	<b>42</b>
3.1	Material selection	42
3.1.1	Diffusion calculations	43
3.1.2	Sample preparation	44
3.1.3	Microstructural analysis	46
3.2	Experimental details	46
3.2.1	Specimen assignment	46
3.2.2	Hydrogen charging and annealing	47
3.2.3	Tensile testing	49
3.2.4	Thermal desorption spectroscopy - TDS	49
3.2.5	Fractographic analysis	50
<b>4</b>	<b>Results and discussion</b>	<b>51</b>
4.1	Diffusion calculations	51
4.2	Microstructural analysis	53
4.3	Tensile testing	54
4.4	Thermal desorption spectroscopy - TDS	61
4.5	Fractographic analysis	62
<b>5</b>	<b>Summary and outlook</b>	<b>69</b>
<b>6</b>	<b>Bibliography</b>	<b>i</b>
	<b>List of Figures</b>	<b>xi</b>
	<b>List of Tables</b>	<b>xiv</b>

# 1 Introduction

Steels are the most widely used structural materials in the world due to their good properties in terms of strength and ductility combined with a reasonable price and suitability for mass production. By changing the alloy composition and the applied heat treatment, a wide range of properties can be achieved for a variety of applications. However, in 2019, the iron and steel industry was responsible for approx. 25% of the global industrial CO<sub>2</sub> emissions [1]. For this reason, attempts have been made to reduce CO<sub>2</sub> emissions in the iron and steel production by using hydrogen as reducing agent in the processing of iron ore, as shown schematically in Figure 1.1. The substitution of carbon-containing reducing agents by hydrogen requires extensive investigations of the influence of hydrogen on the properties of construction materials, e.g. steels. Due to its small atomic size, hydrogen atoms can diffuse considerable distances into solid materials even at room temperature and deteriorate their mechanical properties. In order to achieve a large-scale hydrogen-based iron and steel production, it is important to ensure, that hydrogen can be handled safely and efficiently. For this reason, the degradation of mechanical properties of structural materials by hydrogen, known as hydrogen embrittlement (HE), is a research topic that has received increased attention over the last decades [2].

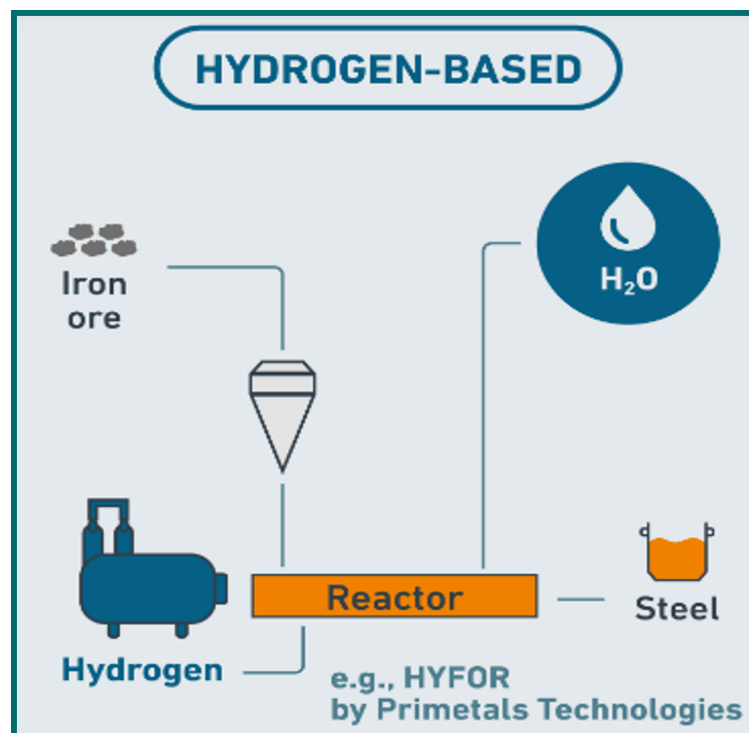


**Figure 1.1:** Principle of the hydrogen usage in a carbon-dioxide-free steel production [3].

The aim of this thesis is the review of current codes and standards covering the design and dimensioning of components in contact with hydrogen, as well as codes and standards specifying materials testing methods in hydrogen atmospheres. In addition, different classes of steels are reviewed with respect to their susceptibility to HE, as well as different materials testing methods, which are commonly used to evaluate the performance of materials in hydrogen-containing atmospheres. The theoretical background of hydrogen uptake, diffusion, trapping and their effects on HE are explained in the theoretical part of this thesis.

For the experimental part of this thesis, tensile tests were performed on uncharged and hydrogen-charged specimens of a martensitic (*PH 13-8 Mo*) and an austenitic (*AISI 303*) steel to investigate the influence of the crystal lattice on the HE susceptibility of the material by comparing various mechanical properties obtained for charged and uncharged specimens. The microstructures of the materials used were examined in an optical microscope after etching. Diffusion calculations were carried out, in order to be able to estimate reasonable hydrogen charging parameters. The specimens were electrochemically charged using either dilute sulfuric acid or sodium hydroxide as electrolyte. To verify the reversible embrittlement effect of hydrogen in the tensile specimens, some specimens were annealed after hydrogen charging, but before tensile testing. The fracture surfaces of the tensile specimens were examined using a stereo microscope and a scanning electron microscope (SEM). The amount of hydrogen in the uncharged and charged specimens was determined by thermal desorption spectroscopy (TDS) measurements.



## 2 Theoretical background

### 2.1 Hydrogen uptake

Hydrogen originating from the environment can enter the bulk of the solid by a combination of different processes, including adsorption, dissociation and absorption. The stable hydrogen configurations, which are present in the environment are its molecular form as  $H_2$  and as  $H_3O^+$  ion. The general process of the transition of gaseous  $H_2$  into two dissolved H atoms can be described according to Equation (1) [4]:



#### 2.1.1 Adsorption

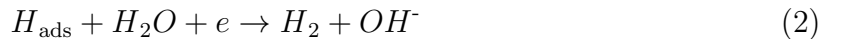
The adsorption process can be further classified as physisorption or dissociative chemisorption.

In physisorption, the chemically relatively inert hydrogen molecule can only form weak van der Waals bonds with the solid surface. The physisorption energy is normally very low (approximately in the range of 3-5 kJ/mole), therefore, liquid helium temperature is usually used to investigate physisorption processes. However, if there are other adsorbates in the vicinity of the surface approaching hydrogen molecule, physisorption is also possible up to room temperature. It is energetically more favorable, and therefore more commonly observed, that the hydrogen molecules are physisorbed on a pre-existing monolayer of atomic hydrogen on the surface, instead of on the metal surface itself [5].

In dissociative chemisorption, the hydrogen molecule dissociates at the crossover point, where the distance between the  $H_2$  molecule and the metal surface is small enough, e.g.  $\sim 2.6 \text{ \AA}$  or less for iron. This process can be explained by the electron density of the metal surface, which is transferred to the  $H_2$  molecule, weakening the bond between the two hydrogen atoms in the molecule [6]. The two now unbound hydrogen atoms can form chemically more stable bonds, mainly covalent bonds, with surface atoms than it would be possible via physisorption. The chemisorption of hydrogen can be either spontaneous or non-spontaneous, depending on the metal substrate and its characteristics, such as the presence of defects and impurities. However, for most systems, even for spontaneous processes, a small amount of activation energy must be supplied to overcome the low activation barriers. Surface defects, such as surface steps, lower the activation

energy barrier and thus promote the dissociation process. This behavior can be seen when comparing the chemisorption on high indexed surface planes, which tend to form surface steps more frequently, with low indexed planes, which are known to form such steps more seldom [7]. Both gaseous and surface contaminants have a dramatic effect on the adsorption process as well. Impurities on the surface can change the activation energy required to overcome the initial energy barrier. Furthermore, impurities can change the amount of energy required to keep the process ongoing, if it is a non-spontaneous process, or the energy released during adsorption, if it is a spontaneous reaction. More important in terms of HE are the gaseous impurities, which can greatly affect the amount of hydrogen adsorbed on the surface even at low concentrations, by blocking dissociation sites and thus reducing the dissociative chemisorption rate of hydrogen. These impurities are more active molecules than hydrogen, such as carbon monoxide or oxygen, and can therefore inhibit HE in this manner [5].

The generation of hydrogen atoms on the metal surface, or, vice versa, the recombination of hydrogen atoms, is possible by gaseous or electrochemical hydrogen charging [2]. The amount of hydrogen adsorbed depends on the prevailing hydrogen recombination mechanism. If Reaction (2) is the main recombination reaction, the applied electrochemical potential favors the hydrogen recombination and at the same time, the formation of atomic hydrogen according to Reaction (3) [8].



Therefore, depending on the dissociation and recombination reaction rates, either a slight increase or even a stagnation in the amount of hydrogen can be expected with increasing cathodic polarization. On the other hand, if Reaction (4) is the dominant recombination mechanism, the cathodic polarization will not significantly promote the hydrogen recombination. However, the cathodic polarization will again promote the generation of hydrogen at the metal surface, as described in Reaction (3). As a result, there is an increase in the amount of hydrogen that penetrates into the steel [8,9].



### 2.1.2 Solubility

When considering gaseous hydrogen charging, the hydrogen concentration in the charged solid can be calculated using Sievert's law for ideal gases, when the gaseous hydrogen is in equilibrium with the dissolved hydrogen [10]:

$$c = s * \sqrt{p}, \quad (5)$$

where  $c$  is the concentration of the dissolved hydrogen,  $s$  is a constant and  $p$  is the partial pressure of hydrogen. This equation can be used as an approximation for real gases at low pressures. For real gases, activities and fugacities must be considered instead of concentrations and pressures. This leads to an improved form of Sievert's law for real gases in the following form [10]:

$$c = \frac{K \sqrt{\Phi * p}}{\gamma}, \quad (6)$$

where  $K$  is the equilibrium constant of Equation (1),  $\Phi$  is the fugacity coefficient and  $\gamma$  is the activity coefficient, representing the ratio of fugacity to pressure and the ratio of activity to concentration, respectively.

In metals, the hydrogen atoms in solid solution are either located at regular lattice sites, such as tetragonal or octahedral sites, or at various lattice defects [4]. Da Silva et al. [11] describes, that the position of the hydrogen atoms in the regular lattice sites is strongly dependent on temperature, with the tetragonal sites being almost exclusively occupied at lower temperatures and a so-called dual site occupancy occurring at higher temperatures. According to the calculations carried out by Lee et al. [12] on ten transition metals, the most favorable hydrogen occupancy sites for body-centered cubic (BCC) and face-centered cubic (FCC) metals are tetragonal and octahedral lattice sites, respectively. However, platinum and gold are two exceptions, according to these calculations, which prefer tetragonal lattice sites instead.

The potential energy of the system is usually lower when hydrogen atoms are located at certain lattice defects, so called trap sites, instead of at regular lattice sites. The influence of the trap sites on the amount and effect of hydrogen in the material is of great scientific interest, since mechanical and thermal processing change the amount of lattice defects in the material and thus influences the hydrogen-material interaction. Typical hydrogen traps are: dislocations, vacancies, precipitates, grain boundaries, voids, and interfaces

[4, 13]. Therefore, the hydrogen solubility,  $S$ , consists of the hydrogen concentration at lattice sites,  $c_L$ , and the hydrogen concentration at trap sites,  $c_T$ , according to Equation (7) [14]:

$$S = c_L + c_T, \tag{7}$$

The solubility of hydrogen is primarily a function of temperature, binding energy and vibrational frequency of the hydrogen atom in solid solution. In general, hydrogen solubility in metals increases with decreasing vibrational frequency and with increasing binding strength of hydrogen in solid solution [12]. The temperature dependency is depicted for 0.1 MPa hydrogen gas in equilibrium for various metals in Figure 2.1. In this figure two main influence parameters on the temperature dependence of the hydrogen solubility can be seen. One is the thermodynamic's influence, represented by the slope of the different functions. Therefore, the hydrogen solubility increases for metals with a positive slope and decreases for metals with a negative slope. The influence of the lattice structure on the solubility of hydrogen can be seen in the case of iron. In the temperature range from 700 °C to 1400 °C a pronounced increase in hydrogen solubility is observed, which is attributed to the change in lattice structure from BCC to FCC [4]. This increase in solubility can be explained by the results of different simulations regarding the behavior of hydrogen atoms in different lattice structures. As an example for this, Ogawa [15] proposed a model that evaluates the solubility of hydrogen in metals in general. This model compares different crystal structures in terms of interstitial sites per metal atom available for hydrogen atoms. According to these calculations, FCC metals have more interstitial sites available for hydrogen atoms than BCC metals, which is consistent with the previous observations of the crystal transformation in iron.

An overview of hydrogen solubility in different steel grades is given in Figure 2.2. It can be seen that there are two different groups of steels in terms of hydrogen solubility. On the one hand there are the ferritic and martensitic steels and on the other hand there are the austenitic steels, whose hydrogen solubilities are higher by a factor of 3 to 20 compared to BCC steels and pure iron. The values for pure iron configurations are in the range of the ferritic/martensitic steels, with  $\alpha$ -iron having the lowest value [16]. Moreover, hydrogen solubility also highly depends on the type and amount of alloying elements. According to Caskey Jr. [16], chromium, manganese and nitrogen increase hydrogen solubility to a greater extent than nickel.

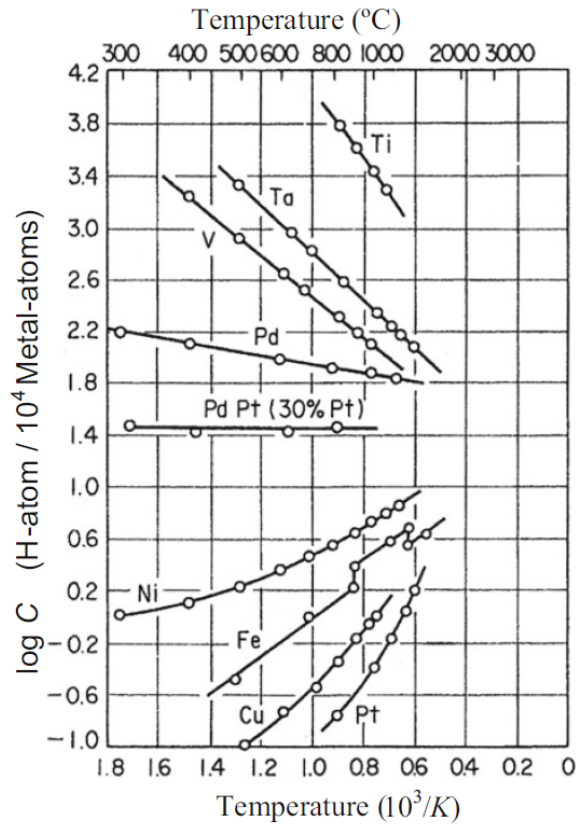


**Figure 2.1:** Hydrogen solubility as a function of temperature for various pure metals in equilibrium with 0.1 MPa hydrogen gas [4].

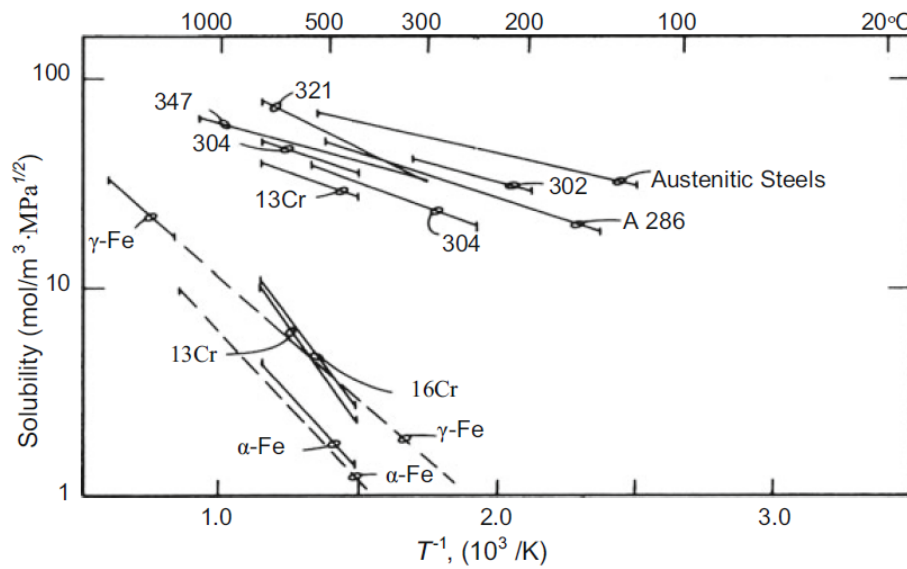


**Figure 2.2:** Hydrogen solubility as a function of temperature for different steels [4].

## 2.2 Hydrogen mobility in metals

Not only the amount of hydrogen that can be dissolved in the material is important for its HE behavior, but also the mobility of the hydrogen atoms. In general, the hydrogen charging technique (gaseous or electrochemical) as well as the charging parameters (hydrogen partial pressure/current density, temperature, time and surface condition) and the material properties (sample thickness, crystal structure of the material, etc.) [17] have an influence on the solubility as well as on the mobility of hydrogen in metals.

The most important atomic transport mechanism regarding hydrogen mobility in metals is diffusion [18], whereby the basic principles of diffusion are explained in the following section. A description of the effects of trapping on hydrogen mobility, is given in Section 2.2.2.

### 2.2.1 Basic diffusion principles of hydrogen in metals

The hydrogen flux based on a spatial concentration gradient in a metal, as well as the temporal concentration gradient, can be calculated using Fick's laws [19]. Whereas, the first law relates the diffusive flux  $J$  to the concentration gradient according to Equation (8) and the second law gives the change of concentration over time according to Equation (9):

$$J = -D * grad(C) \quad (8)$$

$$\frac{\partial C}{\partial t} = D * \nabla^2(C), \quad (9)$$

where  $J$  is the flux of diffusing atoms,  $D$  is the diffusion coefficient,  $c$  is the concentration of the diffusible species under consideration and  $t$  is the elapsed time during the diffusion process.

The diffusion process is based on the frequency of thermally activated jumps between nearby sites with a local energy minimum, represented by the jump frequency [20]. In general, diffusion depends on a number of different state variables. The most important ones are temperature, pressure and concentration. Each of them can be considered individually in the following Equations (10-12), respectively [19]:

$$D = D_0 * \exp\left(-\frac{\Delta H}{RT}\right) \quad (10)$$

$$D_p = D_p^0 * \exp\left(-\frac{p\Delta V^*}{RT}\right) \quad (11)$$

$$D^\Theta = D_{\Theta=0} * (1 - \Theta), \quad (12)$$

where  $D_0$  is the maximal diffusion coefficient at infinite temperature,  $\Delta H$  is the activation enthalpy and  $R$  is the universal gas constant.  $D_p$  represents the diffusion coefficient for a given pressure,  $D_p^0$  is the diffusion coefficient for a theoretical pressure of zero and  $\Delta V^*$  is the activation volume.  $D^\Theta$  and  $D_{\Theta=0}$  are the diffusion coefficients for a given concentration and  $\Theta$  is the fraction of occupiable lattice sites occupied by solute atoms [19].

Equation (12) is based on the fact, that as the concentration of hydrogen atoms increases, more and more lattice sites are blocked, i.e. the further diffusion process becomes slower at locally higher hydrogen concentrations. Furthermore, the concentration dependence of the diffusion coefficient is based on the change of the activity coefficients with changing concentration, i.e. the dissolved hydrogen atoms can locally change the interatomic distances or the electron density and thus influence the activity coefficient [19]. Diffusion processes in crystalline lattices are based on lattice site interactions and therefore depend on the particular geometric features of the lattice. A large difference in the diffusion coefficients can therefore be observed for different crystal lattices. This can be seen when comparing FCC and BCC structures, where the denser atomic packaging of FCC lattices leads to a higher activation energy for diffusion [4]. This results in slower diffusion processes in FCC lattices compared to BCC lattices. Furthermore, the type and amount of alloying elements are important parameters that directly influence the diffusion coefficient. This is due to the disorder of the pure metal lattice and the associated local geometric changes around the solute atoms, as well as the resulting hydrogen traps, e.g. precipitates [13]. An overview of the influence of the crystal lattice, alloying and temperature on the hydrogen diffusion coefficient is given in Figure 2.3, where the trends mentioned above show that pure iron has a higher diffusion coefficient compared to austenitic steels, as well as  $\alpha$ -iron compared to  $\gamma$ -iron [4].

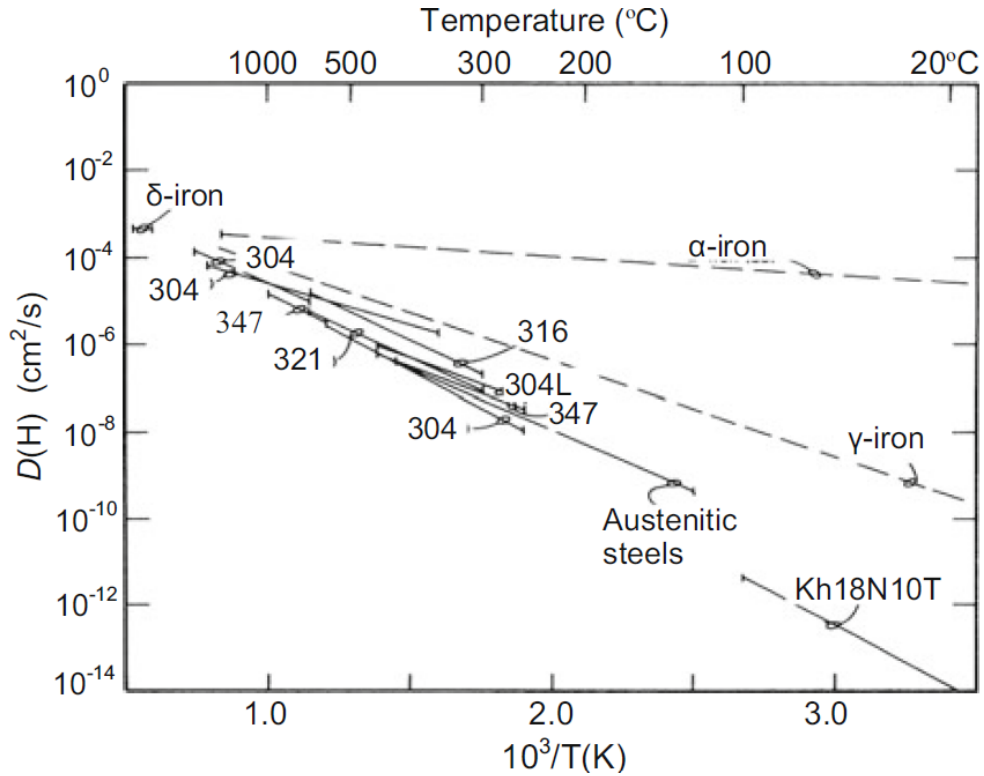


**Figure 2.3:** Hydrogen diffusion coefficients in iron and different austenitic steels [4].

### 2.2.2 Influence of trapping on the hydrogen mobility in metals

The hydrogen diffusion process in a metal is mainly influenced by the crystallographic lattice. However, the binding energy as well as the distribution and density of trap sites present in the material also have a significant influence on the hydrogen diffusion process. This leads to a wide range of diffusion coefficient values found in the literature for different steels in the low temperature range, where most trap sites are irreversible due to the low energy in the system leading to many trapped hydrogen atoms [4].

The trap sites mentioned in Section 2.1.2 are summarized in Figure 2.4. These trap sites are important not only in terms of the hydrogen amount trapped in the material, but also in terms of their influence on the hydrogen kinetics in the material. In other words, the ability of hydrogen to constantly diffuse into and redistribute within the material, due to its size even at room temperature, is the reason why the kinetics of hydrogen in metals is important [21]. Therefore, quantification of the binding energies of different trap types is of great interest, since when hydrogen atoms are strongly bound to certain lattice defects, their ability to diffuse is severely limited. The deterioration of mechanical properties with respect to HE is related to the ability of hydrogen to diffuse freely in the



material. Nagumo et al. [22] stated, that only weakly trapped and diffusible hydrogen contributes to the degradation of the material. This means that strongly trapped and therefore non-diffusible hydrogen is not involved in the deterioration of the mechanical properties at room temperature. This distinction between degradation contributing and non-contributing hydrogen trap sites was demonstrated by Takai et al. [23] for steels with 0.8% C content and an eutectoid microstructure.

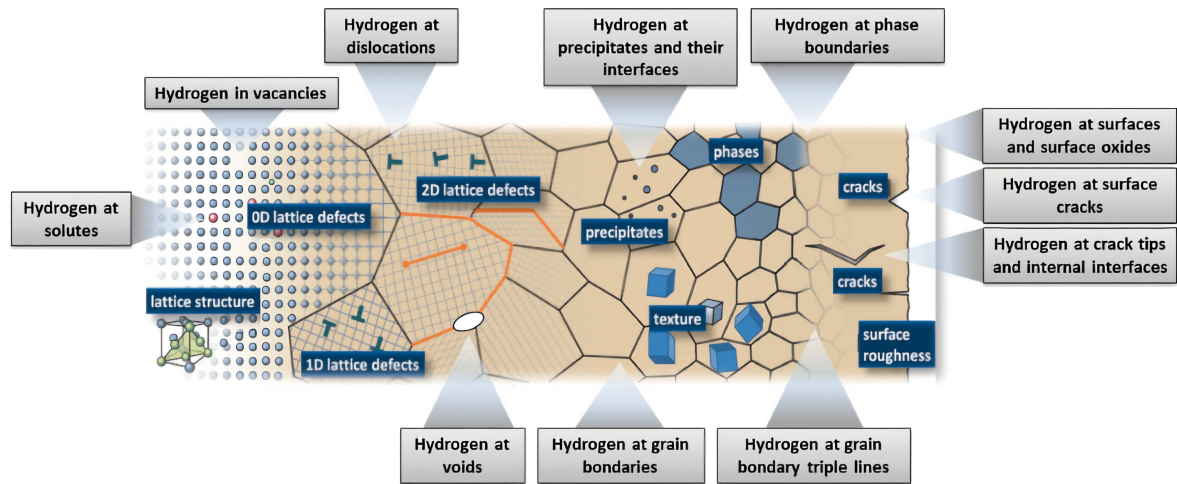


**Figure 2.4:** A variety of possible hydrogen trap sites in metals [21].

The left side of Figure 2.5 visualizes schematically the temperatures required to release hydrogen from different trap sites in pure iron, where the *Ion Intensity* is a measure of the amount of hydrogen released from the sample. From these temperatures, the binding energies of the different trap types in a certain material can be estimated, such that traps with higher release temperatures normally have higher binding energies than traps with lower release temperatures [4]. To sum up, hydrogen atoms bound to strong traps are not able to diffuse through the material at room temperature, while weakly bound hydrogen atoms are able to do so. In the literature, a distinction is often made between diffusible and non-diffusible hydrogen based on the desorption temperature of the respective hydrogen atoms, with the dividing line usually set at about 200 °C. Due to the characteristic peaks in hydrogen release rate versus temperature plots (depicted on the right side of Figure 2.5), diffusible hydrogen is referred to as peak 1 hydrogen and non-diffusible hydrogen as peak 2 hydrogen [23].

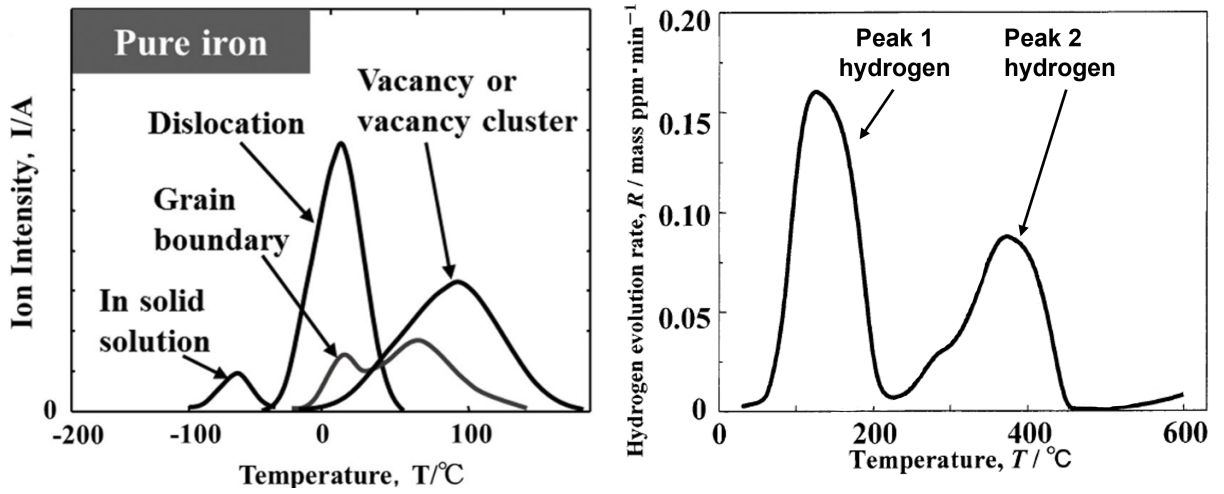


**Figure 2.5:** Left: Hydrogen release temperatures of different trap sites in pure iron [4]. Right: Characteristic hydrogen desorption peaks for diffusible hydrogen (*peak 1 hydrogen*) and non-diffusible hydrogen (*peak 2 hydrogen*) in a cold-drawn eutectoid steel [23].

### 2.3 Hydrogen embrittlement mechanisms

HE is one of the possible damage mechanisms caused by hydrogen in metals. Other ones, listed in the *ASM Materials Handbook*, are: hydrogen-induced blistering, cracking due to hydride formation, cracking as a result of precipitation of internal hydrogen or hydrogen attack [24]. There are different definitions and terminologies of HE in the literature based on the source of hydrogen and/or the type of damage induced. Internal hydrogen embrittlement (IHE) describes the cracking under permanent stresses below the yield strength with pre-existing hydrogen in areas of high applied or residual hydrostatic stresses. Hydrogen environment embrittlement (HEE) represents subcritical crack growth under permanent loads in hydrogen containing gases. The terms HEE, IHE and HE are sometimes replaced by the more general term hydrogen-assisted cracking (HAC). When cyclic loads are applied instead of static loads, the term hydrogen-assisted fatigue is often used [25]. HE is defined as a deterioration of mechanical properties, particularly ductility, and is the most commonly known hydrogen-induced damage mechanism in steels. For ultra-high strength steels, Lynch [25] states that they can be expected to be extremely susceptible to IHE at yield strengths of 1400 MPa or higher, even at very low hydrogen contents of approx 0.5 wt.ppm. In general, a steel with a higher strength will have a higher susceptibility to HE compared to a similar steel with a lower strength level, if there are no major differences regarding their microstructures [25]. This correlation can also be seen in Figure 2.6, which shows the tensile stress-strain curves of three different ferritic pipeline

steel specimens (X52, X65 and X100). These steels have a minimum yield strength of approx. 360 MPa, 450 MPa, and 670 MPa. The relative elongation at fracture (EAF) is a measure of HE susceptibility and is calculated by dividing the EAF in air by the EAF in hydrogen gas. A lower relative EAF value means a higher HE susceptibility of the material. For the tests of the X52, X65, and X100 specimens, the relative EAF values were approx. 0.78, 0.72 and 0.50, respectively [26]. These results support the previously mentioned theory, that a higher material strength increases the HE sensitivity [25].

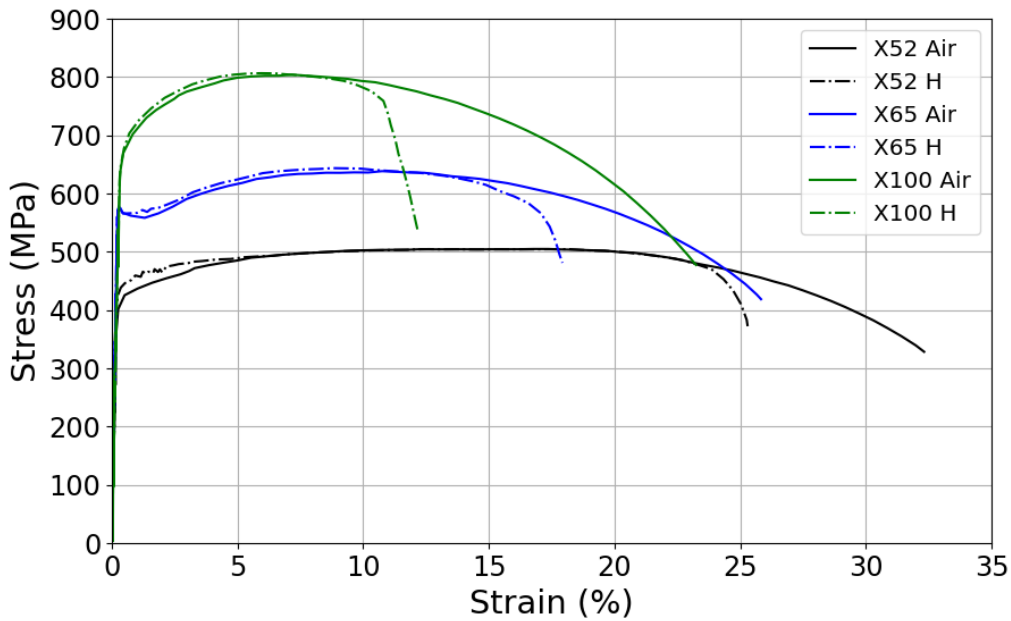


**Figure 2.6:** Tensile stress-strain curves of X52, X65, and X100 pipeline steels (data from Nanninga et al. [26]).

In general, HE is caused by local hydrogen accumulations at potential fracture sites. Multiphase steels with a significant volume fraction of martensite, such as dual-phase steels, are particularly susceptible to HE [27]. This can be explained by the martensite-ferrite interface, which is considered both a potential fracture site and a hydrogen trap. This favors the accumulation of hydrogen at these interfaces and the nucleation of hydrogen-induced cracks, which can propagate more easily through the brittle martensitic phase than through the more ductile ferritic phase. Therefore, an increase of the martensite content leads to an increase of the martensite-ferrite interface area and the HE susceptibility [27]. This correlation is shown in Figure 2.7 for a dual-phase steel by Wang et al. [27], which shows that an increase of the martensite

content leads to an increase of the hydrogen embrittlement index (HEI), a measure often used in the literature to quantify HE.

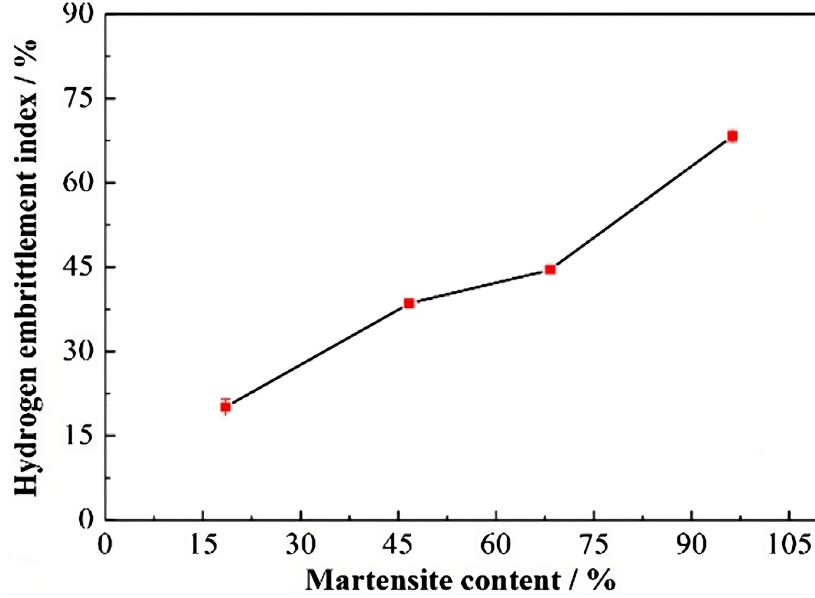


**Figure 2.7:** HEI as a function of the martensite content of a dual-phase steel [27].

In general,  $HEI$  is a measure for the loss of ductility, which can vary from 100 %, which refers to a total loss of ductility, to 0 %, which means that there is no reduction of ductility.  $HEI$  can be calculated using several equations. It is a comparison of mechanical properties, such as EAF or reduction of area (ROA), measured on uncharged and hydrogen-charged specimens. Therefore, it can be calculated using Equation (13) defined by Loidl et al. [28]:

$$HEI_{\delta} = \frac{(\delta_0 - \delta_H)}{\delta_0} * 100 \%, \quad (13)$$

where  $HEI_{\delta}$  is the HEI based on the EAF,  $\delta_0/\delta_H$  is the EAF of the uncharged/hydrogen-charged specimen, respectively. Alternatively, HEI can also be calculated using the following Equation (14) used in [29–31]:

$$HEI_{\phi} = \frac{(\phi_0 - \phi_H)}{\phi_0} * 100 \%, \quad (14)$$

where  $HEI_{\phi}$  is the HEI based on the ROA,  $\phi_0/\phi_H$  is the ROA of the uncharged/hydrogen-charged specimen, respectively.

Steels containing a significant amount of as-quenched martensite are the one, which are the most susceptible to HE, due to the high strength of the untempered martensite and the high residual stresses resulting from the transformation. Martensite tempering leads to an improvement of HE resistance, which is due to the relief of internal stresses and the reduction in strength. Furthermore, it is assumed that thermodynamically more stable phases are less prone to HE [32]. Other important factors regarding HE are microstructure, applied strain rate, surface condition, surrounding environment, temperature, pressure and hydrogen exposure time [17, 33].

For a noticeable deterioration of the mechanical properties, three conditions, visualized in Figure 2.8, have to be fulfilled [17]:

- **Material susceptibility:** The material must be susceptible to HE, which is usually indicated by a high material strength.
- **Hydrogen environment:** Hydrogen needs to be present in the atmosphere or the material itself needs to contain pre-existing hydrogen (e.g. due to the manufacturing process).
- **Mechanical stresses:** There must be sufficient high mechanical stresses.

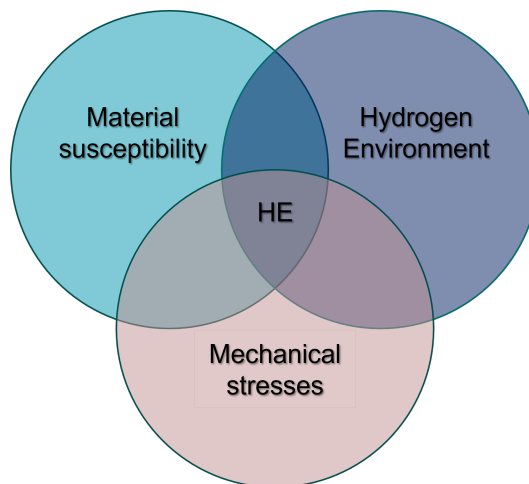


**Figure 2.8:** Necessary requirements for HE.

Despite intensive research on HE in metals over the last decades, there is still no theory that can unambiguously explain the underlying mechanisms of HE. Furthermore, hydrogen-metal interaction can occur in two different forms, which can be classified in hydride-forming (e.g. titanium alloys) and non-hydride-forming (e.g. iron and nickel

alloys) metals [34]. For the non hydride-forming metals four viable HE mechanisms [22, 33, 35] are considered in this thesis, namely:

- Hydrogen-enhanced decohesion (HEDE)
- Hydrogen-enhanced localized plasticity (HELP)
- Adsorption-induced dislocation emission (AIDE)
- Hydrogen-enhanced strain-induced vacancy generation (HESIV)

In most of the cases not just one mechanism is involved in the complex damage process, but there may be an interplay of different ones, with one of them in the foreground [36]. This behavior was reported in HE simulation studies performed by Solanki et al. [37] and Matsumoto et al. [38], where it was found, that for BCC iron different HE mechanisms can occur and be active simultaneously [36]. For a reliable identification of the prevailing mechanisms, each case must be considered individually.

### **2.3.1 Hydrogen-enhanced decohesion - HEDE**

The HEDE mechanism, which was introduced by Troiano in 1959 [39], proposes, that hydrogen in the vicinity of a crack tip can alter the occurring binding energies. Troiano proposed, that the electrons contributed by the hydrogen atoms enter the d-orbital of the metal nucleus. At higher electron densities, the atomic repulsive forces increase and so does the inter-atomic distance between the metal atoms, resulting in a loss of the cohesive strength between the metal cores. This effect is less pronounced when the d-orbital is less filled. For example, when nickel is alloyed with a transition metal that has fewer electrons in the d-orbital, the electron density in that band of the alloy is lower than in that of pure nickel. As a result, the reduction in cohesive strength due to hydrogen atoms is less pronounced in a nickel-iron-chromium alloy than in pure nickel [39].

The HEDE model suggests that hydrogen accumulates at various potential fracture sites such as: sharp crack tips, zones of high hydrostatic stress and regions in front of cracks, such as phase or grain boundaries. Then this hydrogen accumulation potentially leads to the displacement of a crack tip. Therefore, lattice decohesion and crack nucleation occur when the critical crack tip displacement is reached, which is typically half the interatomic distance. Propagation of the crack starts when the stress at the crack tip surpasses the hydrogen-weakened, local cohesive strength [17, 33].

The addition of alloying elements can alter the cohesive energy of the metal and the work required for interfacial separation. The changes in these quantities can then be analyzed to determine the effect of these alloying elements on the resistance to decohesion (due to hydrogen) of the alloy. Kholobina et al. [40] have analyzed the effect of different alloying elements on BCC iron with respect to hydrogen decohesion using DFT calculations for hydrogen co-segregation. It was found that among the materials studied, only tungsten and tantalum can suppress the influence of hydrogen on both grain boundary and bulk decohesion.

A limitation of this model is the high local hydrogen concentration around a crack tip, which is necessary for the hydrogen-enhanced decohesion process [25, 36]. To achieve such high hydrogen concentrations at interstitial lattice sites, it is assumed that very high mechanical stress is necessary [25]. According to the HEDE model, the atoms are separated in the tensile direction during fracture, rather than by lattice slip mechanisms. Therefore, when trying to prove the existence of this model, a featureless fracture surface could be used as evidence. Up to now, there is no technique available that can be used for atomic scale observations of hydrogen-influenced crack tips in bulk material, to investigate crack behavior in order to validate the HEDE model [25, 33].

### **2.3.2 Hydrogen-enhanced local plasticity - HELP**

The HELP model was first presented by Beachem in 1972 [41]. It states, that a sufficiently high local hydrogen accumulation in the vicinity of a crack tip promotes an arbitrary, but possible deformation process. This leads to a localization of the deformation process, thereby enhancing plasticity. According to Dong et al. [35], the HELP theory states that hydrogen weakens the dislocation-obstacle interactions and thus promotes dislocation movement, as such obstacles are generally known to pin dislocations. Furthermore, the increased mobility of dislocations in the presence of hydrogen can also be explained by the fact, that the dislocation-dislocation interactions are reduced by the presence of hydrogen, also known as *shielding*. However, this shielding effect is usually not achievable in non-hydride forming systems under conventional conditions, as a high hydrogen concentration in the range of 10 at% is required for test temperatures close to room temperature. In summary this means, that the HELP model is based on the effective shielding of the dislocation not only from interaction with other dislocations, but also from other physical obstacles in the lattice [17, 33, 42, 43].

The mechanism of crack growth in this model is assumed to be a micro void coalescence process, which is a more ductile fracture behavior. However, depending on the

microstructure, hydrogen concentration and crack tip stress intensity, brittle fracture is also possible due to a potentially ineffective shielding. However, contrary to the model name, the plastic deformation is localized to a very small volume, which means that the overall macroscopic ductility is low [33].

### **2.3.3 Adsorption-induced dislocation emission - AIDE**

The AIDE model was first proposed in 1976 and also further developed by Lynch [25,44] and is somehow a combination of HEDE and HELP. According to this mechanism, hydrogen is adsorbed at regions of high stress, such as crack tips. This model states, that the adsorbed hydrogen promotes local plasticity and consequently crack growth via dislocation emission in the vicinity of the crack tip, similar to the HELP model. The enhancement of dislocation emission includes not only the previously mentioned accelerated movement of dislocations away from the crack tip, but also the enhanced generation of dislocations, which is facilitated by the adsorption of hydrogen at the crack tip. The enhanced dislocation nucleation can be explained by a cooperative shearing process in the range of a few atomic distances around the crack tip, which is possible due to the reduced cohesive bond strength between the metal atoms due to the adsorbed hydrogen atoms, similar to the HEDE mechanism. The actual crack growth can also be explained by this enhanced dislocation emission, as well as by the coalescence of voids in the crack path. In order for this dislocation emission to take place, there must be a sufficiently high level of stress intensity at the tip of the crack [17,33].

### **2.3.4 Hydrogen-enhanced strain-induced vacancy mechanism - HESIV**

The HESIV model is based on the fact that the formation energy of vacancies can be lowered when the already existing vacancies in the metal form clusters with solute hydrogen atoms, which leads to an increase of the vacancy density in thermal equilibrium [45]. The effect of the HESIV mechanism is illustrated in Figure 2.9, which shows the hydrogen content in pure iron samples with different mechanical history. One group of samples ([strain]) was deformed and then exposed to hydrogen. Another group of samples ([H+strain]) was first pre-charged with hydrogen, then deformed and charged again. In this case, the hydrogen content measured by TDS acts as a measure of the density of vacancies due to their ability to trap hydrogen atoms. If hydrogen is present in the material prior to deformation, it will form complexes with the existing vacancies according to the HESIV model [22, 23], thus reducing the formation energy for new



vacancies. As a result, more vacancies are formed during straining than it would have been the case without hydrogen pre-charging. This comparatively higher vacancy density can then be seen by the amount of tracer hydrogen, which is absorbed into the material during the subsequent hydrogen charging, as the increased number of vacancies (hydrogen traps) can also accommodate a higher number of hydrogen atoms [4, 22, 23].

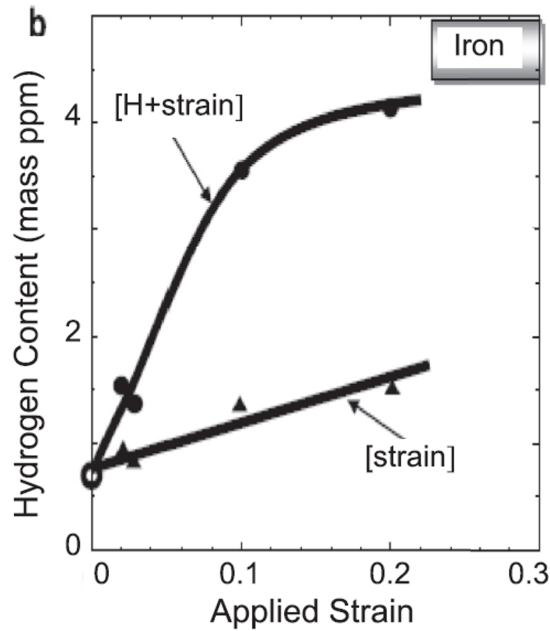


**Figure 2.9:** Hydrogen content of different iron samples that were strained before charging [strain] or that were pre-charged, strained, and then charged [H+strain] [22].

## 2.4 Materials testing methods for hydrogen embrittlement

In order to ensure, that a material can withstand a specific service condition when exposed to hydrogen, material tests dealing with the effects of HE must be carried out. In addition, materials testing is necessary to observe the effects of hydrogen on materials and thus gain fundamental knowledge of the mechanisms of HE. In general, these test methods can be divided into two different categories [46]:

- Materials testing carried out in hydrogen atmosphere (**in-situ** hydrogen charging)
- Materials testing carried out in inert atmosphere or in air, where the material to be tested is pre-charged with hydrogen (**ex-situ** hydrogen charging)

Depending on the test method and the required setup, both electrochemical and gaseous hydrogen charging can be considered for in-situ and ex-situ charging. However, the results obtained between ex-situ and in-situ experiments can differ significantly depending on the experimental design [46]. For example, Zafra et al. [47] claimed, that when comparing fatigue test results for in-situ and ex-situ charged  $42CrMo4$  steel specimens, the fatigue crack growth rate is higher for in-situ charged specimens. This can be explained by the progressive release of hydrogen at the crack faces for ex-situ charged specimens.

For in-situ hydrogen charging, HE can be promoted or suppressed by the addition of small amounts of gaseous substances to the hydrogen gas. Oxygen has often been investigated in the past, as it may mitigate HE effects, as the reactivity of  $O_2$  to most metals is higher than that of  $H_2$  [48, 49]. The protective effect of  $O_2$  additions can be explained by the thin oxide layer formed on the metal surfaces, which blocks  $H_2$  dissociation and adsorption at the surface. Many studies reported in the literature have consistently found that  $O_2$  additions between  $10^{-2}$  and  $10^{-3}$  vol.% can almost completely suppress HE [49]. In conclusion, the degree of HE suppression provided by  $O_2$  additives, and the amount required, is highly dependent on the test conditions (total gas pressure, strain rate, and temperature), as well as the chemical composition, microstructure, and strength of the steel being examined [49].

In this chapter the most relevant materials testing methods for HE are presented, namely tensile testing, fracture mechanics testing, and fatigue testing. These test methods are covered in various relevant standards for HE test methods (reviewed in Section 2.5) [46,50].

### 2.4.1 Tensile testing

Hydrogen degradation during tensile testing manifests itself as premature fracture of the specimen. This degradation can be expressed by comparing quantities such as yield strength, EAF, and ROA measured for charged and uncharged specimens. As explained in Section 2.2.2, not only the amount of hydrogen, but also the hydrogen trapping energies are crucial, when considering the degradation of mechanical properties due to HE. Therefore, specimens containing weakly trapped hydrogen will exhibit pronounced HE, while specimens containing only strongly bound hydrogen atoms will show less or no embrittlement [4, 23]. Takai et al. [23] investigated the influence of the trap activation energy of trapped hydrogen atoms on HE during tensile testing. Weakly bound hydrogen atoms, with desorption temperatures below  $200\text{ }^\circ\text{C}$ , are referred to as *peak 1 hydrogen* and strongly bound hydrogen atoms, with desorption temperatures above  $200\text{ }^\circ\text{C}$ , are referred to as *peak 2 hydrogen*, because of their characteristic peak positions

in TDS measurements as shown in Figure 2.5 on the right side. On the left side of Figure 2.10 stress-strain curves from multiple tensile test for high strength lower-bainitic steel specimens with a tensile strength of approx. 1500 MPa are depicted. The specimens were pre-charged with hydrogen at 50 °C in a 20 wt% aqueous  $\text{NH}_4\text{SCN}$  solution. The pre-charge duration was varied between the specimens and the sample labeled with  $0h$  was not pre-charged with hydrogen. These specimens were not cold-drawn prior to charging and therefore the only significant amount of hydrogen, that can be found in the specimens after charging is *peak 1 hydrogen*. It can be seen on the left graph of Figure 2.10 that *peak 1 hydrogen* leads to a pronounced loss of ductility. Takai et al. [23] were able to show from TDS measurements that the *peak 1 hydrogen* content in these samples reached its maximum at about 3.1 ppm after approx. 15 h, as shown in Figure 2.10 on the right side.

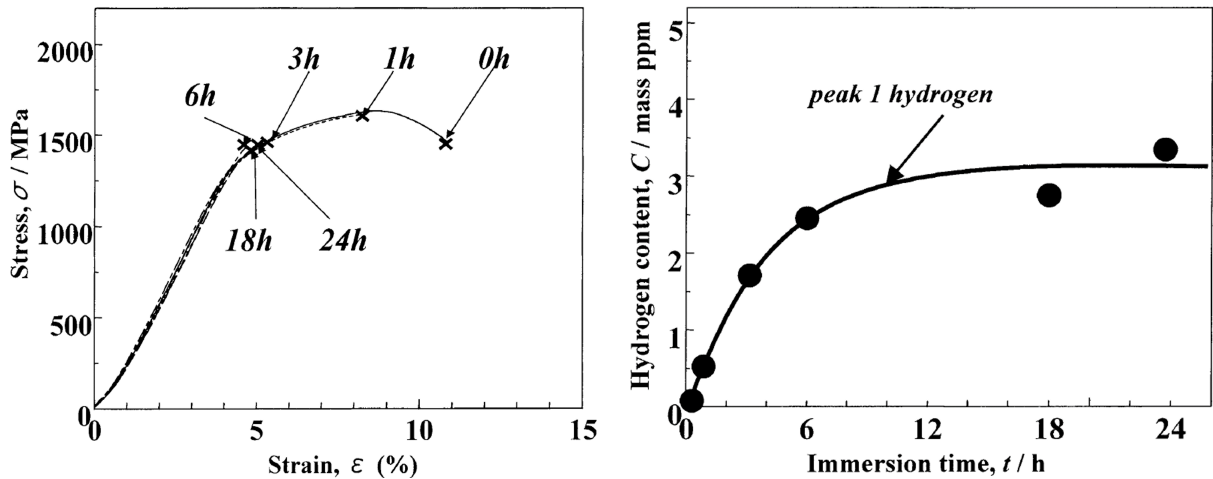


**Figure 2.10:** **Left:** Stress-strain curves from tensile tests of lower-bainitic steel specimens with different hydrogen pre-charging times. **Right:** Hydrogen content over charging time for these specimens [23].

In addition, Takai et al. [23] tested steel specimens with the same composition, which were cold-drawn to a ROA of 85 % before hydrogen charging to obtain *peak 2 hydrogen* trap sites. The charging and testing conditions were similar to those described above. The specimens used for tensile testing were heated up to 200 °C after hydrogen charging, but before tensile testing, in order to remove the *peak 1 hydrogen*. The stress-strain curves of these tensile specimens are shown in Figure 2.11 on the left, with the respective *peak 2 hydrogen* content in the specimen on the right. In this figure it can be seen, that there is almost no degradation of the specimen (except for the outlier  $1h$ ), which fits very well with

the theory that only *peak 1 hydrogen* contributes to the degradation of the mechanical properties, while *peak 2 hydrogen* does not [22, 23, 51].

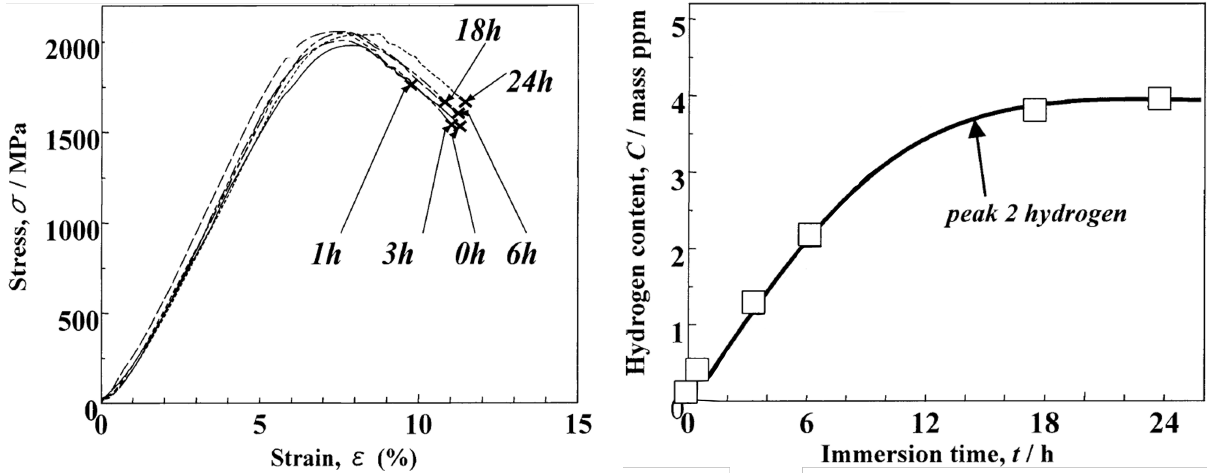


**Figure 2.11:** Left: Stress-strain curves from tensile tests of cold-drawn lower-bainitic steel specimens with different hydrogen pre-charging times after annealing at 200 °C. Right: Hydrogen content over charging time for these specimens after annealing at 200 °C [23].

Two test parameters that have a major influence on the measurement results of tensile tests, but also on fracture mechanics tests, fatigue tests, etc., are temperature and strain rate. These effects are shown in Figure 2.12 in terms of the relative ROA for a cold-drawn pearlitic steel with a tensile strength of approx. 1850 MPa. The relative ROA is calculated by dividing the ROA of an uncharged sample by the ROA of a similar, but charged sample. In short, a lower relative ROA value represents a higher HE susceptibility. This figure again shows that only *peak 1 hydrogen* and not *peak 2 hydrogen* has a detrimental effect on the mechanical properties [4, 23, 51].

On the left side of Figure 2.12 it is depicted, that hydrogen degradation for this steel is mainly prominent in the range between  $-20$  °C and 100 °C. As mentioned in Section 2.3.4 the amount of hydrogen-induced lattice defects increases, when *peak 1 hydrogen* is present in the sample prior to tensile testing (i.e. prior to straining). However, Doshida et al. [51] were able to show by TDS measurements, that the amount of hydrogen-induced lattice defects only increases, if the test temperature is high enough, so that the diffusion rate of *peak 1 hydrogen* is sufficiently high. The balance between the velocity of mobile dislocations (constant for a constant strain rate) and the hydrogen diffusion rate is crucial for hydrogen-dislocation interactions. This means that the amount of hydrogen-induced vacancies can only be increased, if the diffusion rate of diffusible hydrogen is high enough to interact with the mobile dislocations. The hydrogen can then diffuse to the newly formed

vacancies, created by plastic deformation, and can then be trapped there. This process stabilizes the vacancies by combining many vacancies into more stable vacancy clusters. In contrast, at very low test temperatures or for samples containing no *peak 1 hydrogen*, the amount of hydrogen-induced vacancies would not increase, because the newly formed unstable vacancies would be annihilated without the stabilizing *peak 1 hydrogen* due to the low diffusion rate of hydrogen at low temperatures [51].

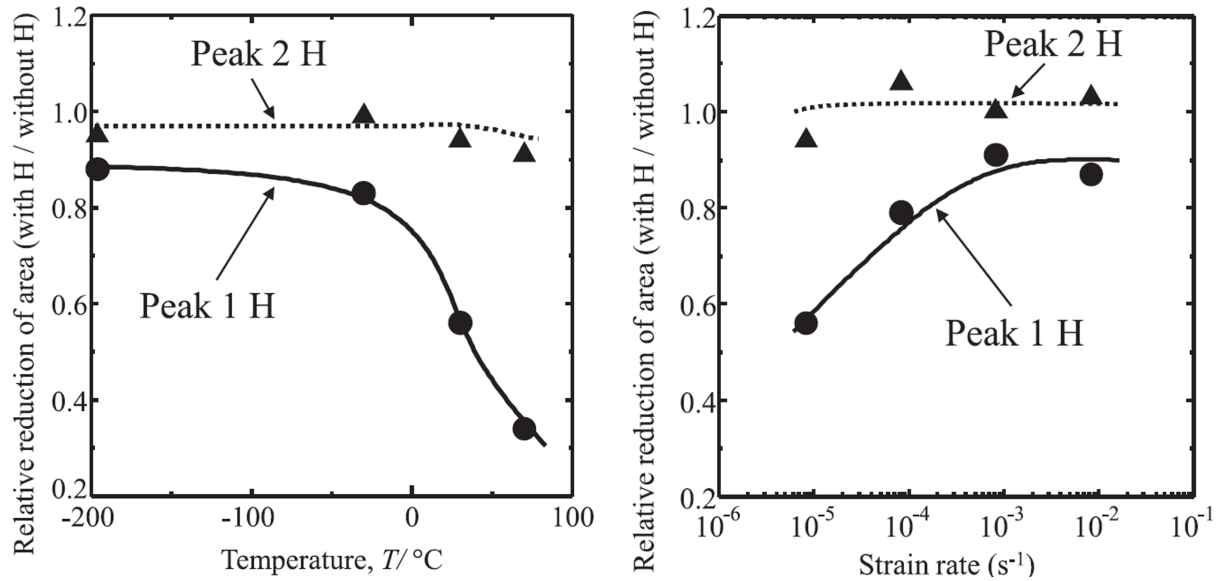


**Figure 2.12:** Influence of temperature (**left**) and strain rate (**right**) on the relative ROA measured in tensile tests [51].

The right graph in Figure 2.12 shows, that hydrogen degradation is mainly prominent for strain rates below  $10^{-3}$  1/s. For a constant testing temperature the hydrogen diffusion rates are constant. However, a lower strain rate results in a lower velocity of the mobile dislocations, as they are directly proportional to each other. The balance between the hydrogen diffusion rate and the velocity of mobile dislocations can again be used to explain this concept. Doshida et al. [51] showed that the amount of hydrogen-induced defects increases for lower strain rates, but only when *peak 1 hydrogen* is present in the specimen. Therefore, when the strain rate is too high, the hydrogen atoms are unable to catch up with the mobile dislocations and less hydrogen atoms are transported by dislocations to stabilize newly formed vacancies to vacancy clusters [51].

In summary, a lower strain rate and a test temperature close to room temperature will increase HE susceptibility in tensile tests. The exact temperature range that promotes HE susceptibility is strongly dependent on the binding energies and diffusion coefficients of the material used, as well as on the applied strain rate. This leads to the assumption,

that it is not hydrogen itself that leads to HE, but the hydrogen-induced generation of defects, especially vacancies and vacancy clusters, as it is described in the HESIV theory [4, 22, 23, 51].

### 2.4.2 Fracture mechanics testing

To evaluate HE effects in fracture mechanics tests, a slow strain rate is required, therefore, impact tests, such as Charpy, are not applicable. The most commonly used quantities to express the deterioration of fracture mechanics properties are the stress intensity factor, the J-integral, and the crack tip opening displacement. Bulky specimens are usually required for fracture mechanics testing, which may lead to inhomogeneous charging of the specimen. Initiation and growth of cracks is usually conducted under controlled charging and environmental conditions. Frequently used specimen geometries for such tests are: compact tension, double cantilever beam, and wedge opening loading specimens [4].

The stress intensity factor,  $K$ , is a quantity, which describes the stress state near a crack tip. The critical stress intensity factor,  $K_C$ , (also called fracture toughness) defines the value of  $K$  above which a crack will propagate rapidly through the material leading to catastrophic failure of the specimen. In other words,  $K_C$  describes the ability of a material to resist unstable crack propagation. The threshold stress intensity factor,  $K_{th}$ , is defined as the value  $K$  below which crack growth is negligibly small. This means that for a  $K$  value between  $K_{th}$  and  $K_C$  a crack can propagate stably through the specimen [4].

Figure 2.13 shows  $K_{th}$  values for various *AISI 4340* quenched and tempered steel specimens with the same chemical composition (36CrNiMo4), but different yield strengths. This figure illustrates the influence of yield strength and hydrogen pressure on  $K_{th}$ . It can be seen that  $K_{th}$  is lower for steels with a higher yield strength at a given hydrogen pressure or for a higher hydrogen pressure at a given yield strength [4]. Clark [52] was able to show for a *AISI 4340* steel specimen with a yield strength of 1240 MPa that an increase in temperature above room temperature results in a significant increase in  $K_{th}$ . However, its influence on  $K_{th}$  is negligible in the range between  $-40\text{ }^\circ\text{C}$  and  $30\text{ }^\circ\text{C}$ .

The J-integral is the change in deformation energy between two crack lengths differing by the crack extension  $\Delta a$ . It is applicable to specimens, where linear elastic fracture mechanics does not apply, i.e. where the plastic yielding around the crack tip is not negligibly small [53]. The J-integral is usually plotted as a function of  $\Delta a$  and is referred to as the crack resistance curve,  $J_R$ .

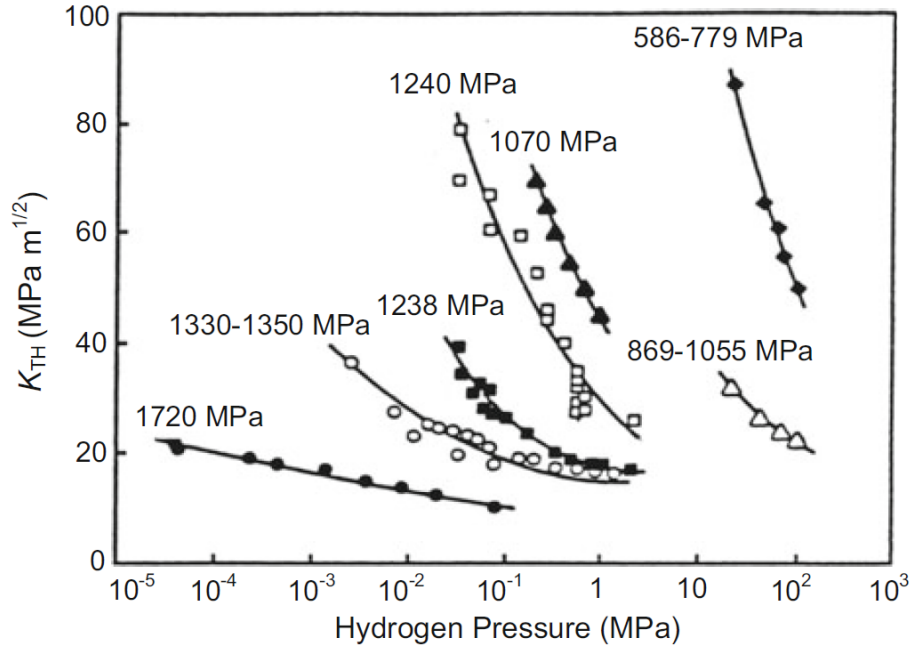


**Figure 2.13:**  $K_{th}$  as a function of hydrogen pressure for various *AISI 4340* steel samples with different yield strengths [4].

The influence of the test atmosphere on the J-integral is shown in Figure 2.14, which shows different  $J_R$  curves for a *15MnNi6-3* steel in argon, hydrogen and  $H_2-O_2$  mixtures at room temperature. The total gas pressure for all these tests was constant at 9 MPa. Deviations between the  $J_R$  curve in inert atmosphere and in hydrogen containing gases can be used as a measure of HE. Over the whole crack growth range  $\Delta a$ , the test conducted in the inert argon atmosphere gave the highest J-values, while the tests conducted in the pure hydrogen atmosphere gave the lowest J-values. The  $H_2-O_2$  gas mixtures were in between, with the mixture containing 0.015 vol.%  $O_2$  being closer to the argon curve [54]. These tests showed, that small additions of  $O_2$  to hydrogen gases can significantly affect the fracture behavior of a *15MnNi6-3* steel. The addition of 0.015 vol.%  $O_2$  to pure hydrogen gas results in a pronounced shift of the  $J_R$  curve toward the inert curve for this material. These findings support the previously mentioned theory that oxygen additives can mitigate HE on the material being tested in the hydrogen gas mixture [48, 49]. It is assumed that the HE suppressing effect of inhibitor gases is time-dependent and therefore, slow strain rate testing methods (i.e. fracture mechanics tests, such as J-Integral) are used to examine the loss of inhibitor strength over time [48].

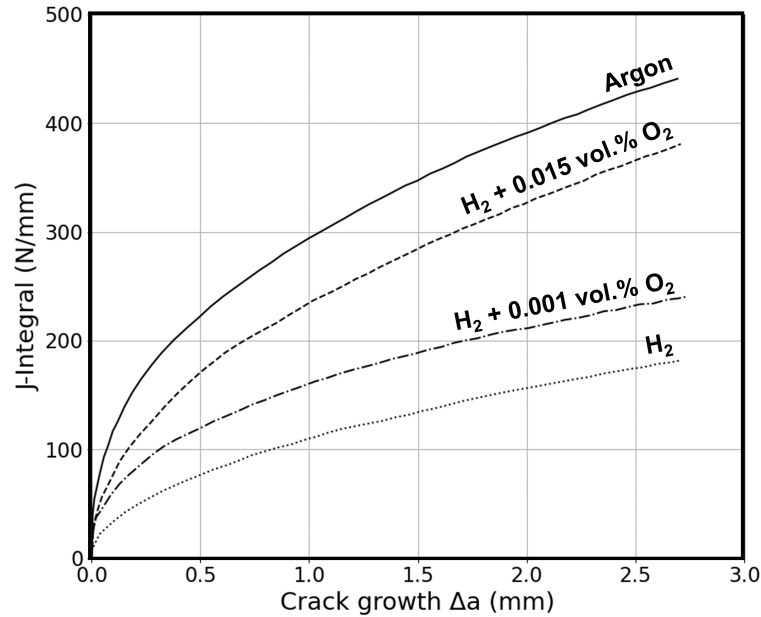


**Figure 2.14:** J-Integral as a function of crack growth for a *15MnNi6-3* steel in different atmospheres (data from Kussmaul et al. [54]).

### 2.4.3 Fatigue testing

Fatigue failure in hydrogen-containing atmospheres is possible not only in pure hydrogen under high pressure, but also in corrosive or humid environments, where hydrogen atoms are generated by electrochemical processes, such as cathodic protection. Fatigue properties are often visualized in S-N curves, from which fatigue life and fatigue limit can be determined. Notched specimens are commonly used to measure crack growth in laboratory tests. Due to the long duration of fatigue tests, the amount of hydrogen in the specimen is often not constant for ex-situ charged specimens [4].

Hydrogen generally lowers the fatigue limit, as well as the fatigue life [4]. Murakami et al. [55] investigated the effect of hydrogen on fatigue life and fatigue limit for various ex-situ charged stainless steels. For austenitic stainless steels, a critical factor in hydrogen-enhanced fatigue crack growth is the austenite fraction, that transforms to martensite near the crack tip due to cyclic loading. Therefore, austenitic stainless steels containing a high amount of austenite stabilizers (e.g. nickel) may be less susceptible to HE regarding fatigue failure. This behavior is shown in the study of Murakami et al. [55], where the hydrogen-charged *SUS304* (8.19 wt.% nickel) and the *SUS316* (10.2 wt.% nickel) specimens showed a noticeable increase in the crack growth rate in comparison to the uncharged specimens. However, the charged *SUS316L* (12.1 wt.% nickel) specimen showed no pronounced differences between the charged and uncharged



tests. For the tested martensitic specimens (0.7C-13Cr steel), the fatigue limit and fatigue life were significantly reduced for charged specimens. It was found by Murakami et al. [55], that non-metallic inclusions act as crack initiators and that non-diffusive hydrogen (*peak 2 hydrogen*) is trapped at non-metallic inclusions. There it is assumed to enhance the fatigue crack initiation process and the early stages of crack propagation. Diffusive hydrogen above a critical local concentration may contribute to a decrease of the threshold value for fatigue crack growth. However, Nagumo [4] stated in this context, that only diffusive hydrogen (*peak 1 hydrogen*) contributes to degradation and non-diffusive (*peak 2 hydrogen*) does not.

In Figure 2.15 S-N curves for high strength Si-Cr martensitic steel specimens with and without ex-situ hydrogen charging are depicted. It can be seen that the effect of hydrogen on the fatigue life is strongly pronounced. For example, at a stress amplitude of 600 MPa, the uncharged sample sustained  $10^6$  cycles, while the charged sample sustained only  $10^5$  cycles. At the same time, the influence of hydrogen on the fatigue limit is small. A measurement of the hydrogen content in the specimen showed a higher defect density in the ex-situ charged hydrogen specimens, than in the uncharged specimens for similar cycles. It is assumed, that hydrogen in combination with point defects, such as vacancies, can reduce the crack growth resistance. Furthermore, there is an assumption, that hydrogen is also involved in the crack initiation process [4, 56].

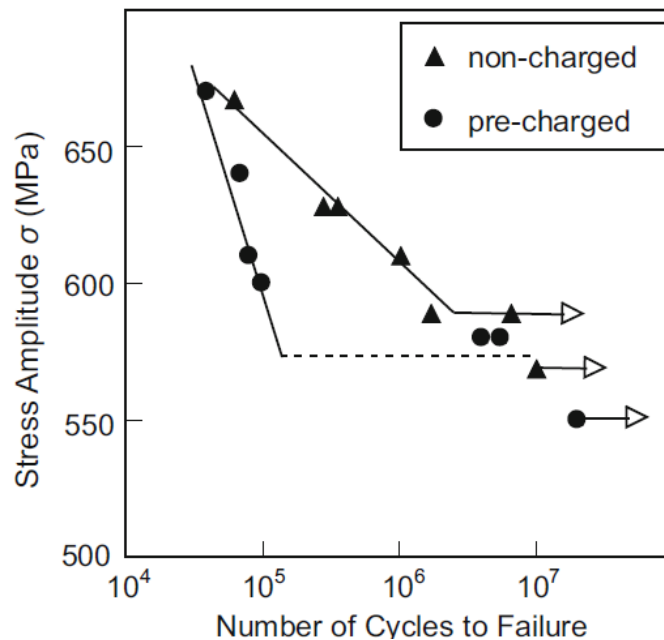


**Figure 2.15:** S-N curve for a Si-Cr martensitic steel measured for rotational bending fatigue with and without ex-situ hydrogen charging, the arrows indicate that there was no failure [4].

The sensitivity to HE regarding fatigue is strongly dependent on the hydrogen permeation rate of the microstructure. A pearlitic microstructure is known to have low hydrogen permeation rates [48] and therefore, steels with a fully pearlitic microstructure are found to be almost immune to HE in fatigue tests. In general, a higher pearlite phase fraction results in a lower sensitivity to HE in fatigue [48].

The fatigue crack growth rates shown in Figure 2.16 have been measured for a *X42* pipeline steel with a mixed ferritic-pearlitic microstructure in various gas mixtures. The test in  $N_2$  is intended as a reference measurement, to see the effect of HE on the crack growth rate in pure  $H_2$  gas by comparison. The other test atmospheres show the effect of different inhibitor gas additives in  $H_2$  gas.  $SO_2$ ,  $O_2$ , and  $CO$  are the most effective inhibitors for fatigue testing of a *X42* steel [48] in the concentrations given in Figure 2.16. In general, the effectiveness of an inhibitor gas depends mainly on three properties: its reactivity with the steel surface, the type of adsorption process (dissociative or in molecular form) and the dissociation products. The gases that dissociatively adsorb on the surface are the most effective inhibitors. The strongest inhibitors generate a sulfur, oxide, water, or carbide layer on the steel surface with their dissociation products [48].

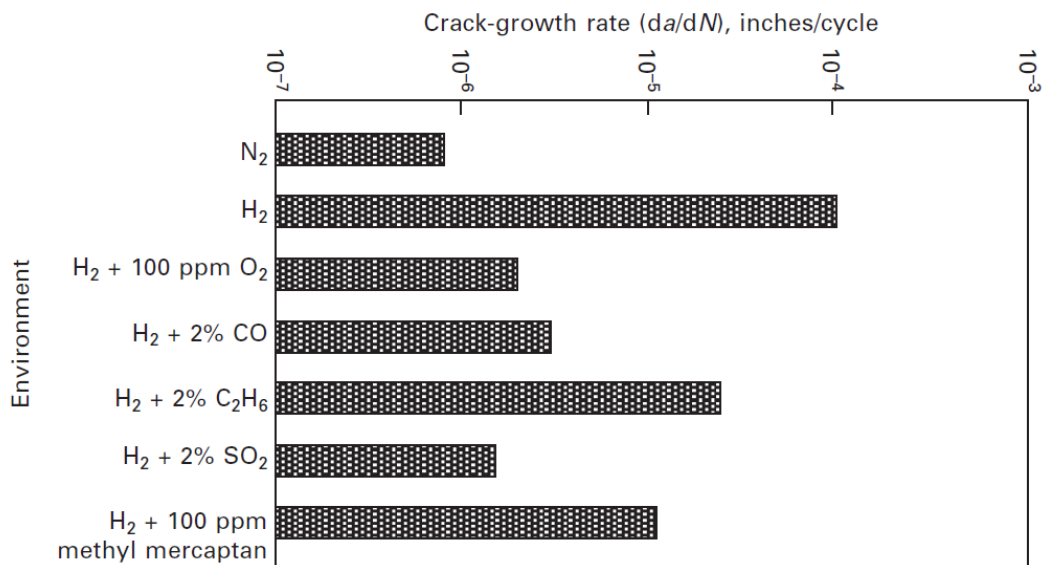


**Figure 2.16:** Crack growth rate for fatigue tests conducted on *X42* steel specimens in different environments [48].

## 2.5 Codes and standards for hydrogen components

According to recent research by Fischer et al. [50], only a few codes and standards are available for the design and dimensioning of components in contact with gaseous or liquid hydrogen. Such components are hereafter referred to as hydrogen components. Additionally, there are only a few standards dealing with the measurement of mechanical properties in hydrogen atmosphere [50]. Currently available benchmarks for the evaluation of the performance of hydrogen components are the *ASME* code for pressure piping, *B31.12-2019* [57] combined with the *ASME Boiler and Pressure Vessel Code - Section VIII - Division 3 (BPVC.VIII.3-2021)* [58].

The *ASME B31.12* code covers the construction, design, operation, and maintenance of industrial piping systems, pipelines, pressure vessels, and distribution systems in hydrogen atmospheres. The *BPVC.VIII.3* code covers alternative design rules for the construction of high pressure vessels, including hydrogen applications, with design pressures of at least 70 MPa. These two standards use a fracture mechanics approach for their benchmarks. However, fracture mechanics testing often requires bulky specimens, so applying these ASME codes to thin-walled components can be difficult. Furthermore, according to Fischer et al. [50], design codes for other hydrogen components like fittings, compressors, valves, etc. are currently not available or in the early stages of development. For the design of storage tanks and similar components, the *German AD 2000* code [59] may also be of interest in the near future, since in this code (in the bulletin S2) the assessment of hydrogen components is based on fatigue testing.

Standards for materials testing in hydrogen atmosphere are required for the application of hydrogen component design codes. The most relevant standards currently available are *ASTM G142 - Determination of Susceptibility of Metals to Embrittlement in Hydrogen Containing Environments at High Pressure, High Temperature, or Both* [60], *ISO 11114-4 - Transportable gas cylinders - Compatibility of cylinder and valve materials with gas contents - Part 4: Test methods for selecting steels resistant to hydrogen embrittlement* [61] and *ANSI/CSA CHMC 1 - Test methods for evaluating material compatibility in compressed hydrogen applications - Metals* [62]. These standards cover different material test methods like tensile tests, fracture toughness tests or fatigue tests. However, they are not harmonized in their detailed test parameters with each other [50]. In addition, the *European Industrial Gases Association (EIGA) IGC Doc 121/4* of 2014 is reviewed, which is considered more of a detailed guideline than a mandatory standard. In this chapter the above codes for the design of hydrogen components, as well as the standards dealing with

materials testing of hydrogen components are reviewed and a brief summary is given in Table 2.1.

**Table 2.1:** Overview of the materials, approaches, test methods and parameters covered by the codes and standards in this chapter [50, 57, 59–62].

	ASME B31.12	AD 2000 S2	EIGA IGC Doc 121/4
<b>Material</b>			
Carbon steels	✓	✓	✓
Low-alloy steels	✓	✓ <sup>2</sup>	✓
Austenitic steels	✓	✓ <sup>3</sup>	✓
Nickel alloys	✓	✓ <sup>3</sup>	✓
Aluminum alloys	✓	✓ <sup>3</sup>	-
Copper alloys	✓	✓ <sup>3</sup>	✓
<b>Approach</b>			
Fracture mechanic	✓	-	-
Fatigue based	-	✓	-
Multiple tests	-	-	✓ <sup>5</sup>
<b>Parameter</b>			
Temperature T	$T \geq -62\text{ °C}^1$	- <sup>4</sup>	$-40\text{ °C} \leq T \leq 175\text{ °C}$
Pressure p	$p \leq 21\text{ MPa}$	- <sup>4</sup>	$1\text{ MPa} \leq p \leq 21\text{ MPa}$

	ASTM G142	ISO 11114-4	ANSI/CSA CHMC 1
<b>Test method</b>			
Tensile	✓	-	✓
Fatigue life (S-N)	-	-	✓
Fatigue crack growth	-	-	✓
Fracture toughness	-	✓ <sup>6</sup>	✓ <sup>7</sup>

**1** ... Maximum specified temperature is material-dependent

**2** ... Only ferritic or quenched and tempered steels

**3** ... Not specified in the hydrogen section

**4** ... No specific temperature/pressure range given

**5** ... Tensile, fracture toughness, slow strain rate, and disk pressure tests

**6** ... Only step-load mode

**7** ... Only constant displacement mode

### 2.5.1 ASME B31.12

The *ASME B31.12* code (2011) [57] includes regulations for industrial piping systems, as well as for pipelines and general requirements for other systems in hydrogen service. It is a globally accepted code for the operation and design of pipes and pipelines containing gaseous hydrogen and hydrogen-containing mixtures with at least 10 vol.% of hydrogen. Pressures up to 21 MPa and temperatures down to  $-62^{\circ}\text{C}$  (upper temperature limit is material-dependent) are covered in this code. A wide range of metals and also a variety of fabrication products such as tubes, plates, forgings, fittings, etc. are covered. [57, 63].

With this code the maximum allowable gas pressure for a given wall thickness or a minimum wall thickness at a given gas pressure can be calculated for various applications and geometries. To accommodate HE for the design of hydrogen pipelines and piping systems, this code covers two main approaches, with maximum ultimate tensile strength (UTS) and maximum specified minimum yield strength (SMYS) prescribed for both approaches [57, 63].

**Approach A** introduces a hydrogen material performance factor (HMPF), which has the advantage that for simple piping applications and pipe geometries no material tests are required. It can take values between 0 and 1 and depends on the material used, as well as on its strength and the system design pressure, thus reducing the mechanical properties of the materials according to HE. This means, for example, that a HMPF value of 0.8 reduces the maximum allowable stress to 80% of its original value. HMPF only has to be determined for carbon steels, as well as for low- and intermediate-alloy steels. For all other applicable materials (i.e. stainless steels, copper, copper alloys, nickel, nickel alloys and aluminum alloys) included in this code, this factor can be set to 1. An exemplary table for the determination of HMPF, for a given system design pressure and yield/tensile strength of the material used, is shown in Figure 2.17. This code also specifies the maximum allowable stress over a wide range of temperatures for the above mentioned materials. However, even in the approach A, materials testing is required for pipes with an outer diameter greater than 114.3 mm or for welded constructions. In these cases, Charpy tests are required to ensure specimen size dependent impact energies. Furthermore, it is specified that these Charpy tests have to be performed in the same environment as in the actual application. However, Fischer et al. [50] claim that such a test capability does not yet exist [57, 63].

Specified Min. Strength, ksi		System Design Pressure, psig					
Tensile	Yield	≤1,000	2,000	3,000	4,000	5,000	6,000
70 and under	≤52	1.0	0.948	0.912	0.884	0.860	0.839
Over 70 through 75	≤56	0.930	0.881	0.848	0.824	0.800	0.778
Over 75 through 80	≤65	0.839	0.796	0.766	0.745	0.724	0.706
Over 80 through 90	≤80	0.715	0.678	0.645	0.633	0.618	0.600

**Figure 2.17:** Exemplary table for the determination of HMPF for carbon steel pipes [57].

**Approach B** is specified for welded steel pipes and pipeline structures. It is based on the assumption that the components contain cracks and that these cracks grow as a result of cyclic loading. Non-destructive testing shall be used to determine the size of initial cracks. These test methods are specified in the *ASME Section VIII Division 3* code. Approach B uses the same equations to calculate the minimum wall thickness for a given pressure or vice versa as approach A. However, in approach B, HMPF can be set directly to 1, if certain conditions, most of which must be determined by materials testing, are met. These conditions are specified in the *ASME B31.12* code. The lifetime assessment in this approach is based on fatigue crack growth curves and on fracture toughness, both of these must be measured in hydrogen atmosphere. Therefore, measurements of the threshold stress intensity factor,  $K_{th}$ , are necessary for the base material, the heat affected zone, and the weld material. These  $K_{th}$  values have to be measured in hydrogen gas. The lowest value is then compared to the applied stress intensity factor,  $K_{IA}$ , which can be calculated for a given geometry using the *ASME Section VIII Division 3* code. The *ASME B31.12* code also covers the influence of HE in welds or heat affected zones by prescribing Brinell hardness measurements after any post-weld heat treatment. The location and number of indentations required are also specified [50, 57, 58, 63].

In comparison, approach B is a more time-consuming, but less conservative approach, because the influence of HE can be captured more accurately, meaning that not as high design safety factors are required as it would be the case in approach A. However, approach B is more specific than approach A and is therefore not suitable for all applications described in this standard [57, 63].

Apart from mandatory requirements, the *ASME B31.12* code contains more general but non-mandatory guidelines, which are briefly reviewed below [57]. It is stated that the susceptibility to HE increases with the strength of the material used. In order terms,  $K_{th}$  regarding hydrogen assisted fracture decreases with increasing yield strength. Therefore, when designing hydrogen piping applications, not only a minimum yield strength limit, but also a maximum yield strength limit is required. Another important trend is the

increase in the susceptibility of metals to HE at higher hydrogen gas pressures, which can be seen by a decreasing  $K_{th}$  value with increasing gas pressure. This trend can be explained by the fact, that a higher hydrogen gas pressure favors a higher concentration of atomic hydrogen in the material, which promotes HE. The effect of HE on carbon steels and low-alloy steels is reduced with increased temperature, but at higher temperatures (approximately above 200 °C) other effects such as high temperature hydrogen attack (HTHA) can be triggered. This mechanism can be described by the formation of high pressure methane gas, when the dissolved hydrogen atoms react with the carbon atoms in the steel. This creates cracks in the material and locally decarburizes the steel, resulting in a change in properties. As a rule of thumb, it is stated that HE typically occurs below 95 °C because at or below this temperature the hydrogen remains dissolved in the material. Above 230 °C the hydrogen can diffuse out of the material and the HE effect is reversible. However, this is only valid if cracks have not yet formed and the atmosphere does not contain significant amounts of hydrogen gas. The *ASME B31.12* code claims that there are no structural materials that are immune to HE. However, the severity of HE varies greatly for different classes of structural materials, as depicted in Figure 2.18, which shows the compatibility of various materials with gaseous and liquid hydrogen. Therefore, it is not possible to select a metal or alloy from a list of materials that are immune to HE, which means that for each specific application, an appropriate selection and design of the components must be made according to the existing operating conditions [57].

Material	Form of Hydrogen		Notes
	Gas	Liquid	
Aluminum and aluminum alloys	Acceptable	Acceptable	...
Austenitic stainless steels with greater than 7% nickel (e.g., 304, 304L, 308, 316, 321, 347)	Acceptable	Acceptable	Beware of martensitic conversion at low temperature if stressed above yield point
Carbon steels	Acceptable	Not acceptable	Too brittle for cryogenic service
Copper and copper alloys (e.g., brass, bronze, and copper-nickel)	Acceptable	Acceptable	...
Gray, ductile, or cast iron	Not acceptable	Not acceptable	Not permitted for hydrogen service
Low-alloy steels	Acceptable	Not acceptable	Too brittle for cryogenic service
Nickel and nickel alloys (e.g., Inconel and Monel)	Not acceptable	Acceptable	Beware of susceptibility to hydrogen embrittlement
Nickel steels (e.g., 2.25%, 3.5%, 5%, and 9% Ni)	Not acceptable	Not acceptable	Beware of ductility loss
Titanium and titanium alloys	Acceptable	Acceptable	...

**Figure 2.18:** Gaseous and liquid hydrogen compatibility of various material classes [57].

Carbon steels are often used for hydrogen components in welded constructions. HTHA is a serious problem for carbon containing steels at operating temperatures above 200 °C. As a result, the American Petroleum Institute (API) has published empirical Nelson

curves (some are depicted in Figure 2.19) for various steels, which are used to identify the temperature and pressure ranges at which HTHA can occur. In such Nelson curves, each line represents a group of steels. The operating condition being tested is quantified by the highest temperature and pressure occurring in the process. The combination of temperature and pressure results in a unique point on the graph. Any Nelson curve above this point describes a steel or a group of steels, which should be suitable for that service condition. However, [64] summarizes reports claiming that catastrophic failures have occurred in the past at operating conditions in the safe zone (i.e. under the Nelson curve), leading to several revisions of these diagrams. For carbon steels in general, the API 5L (PSL 2) grades *X42* and *X52* are recommended in this code. For an increased resistance to HE, the microalloyed variants of *X42* and *X52* are suggested in [57].

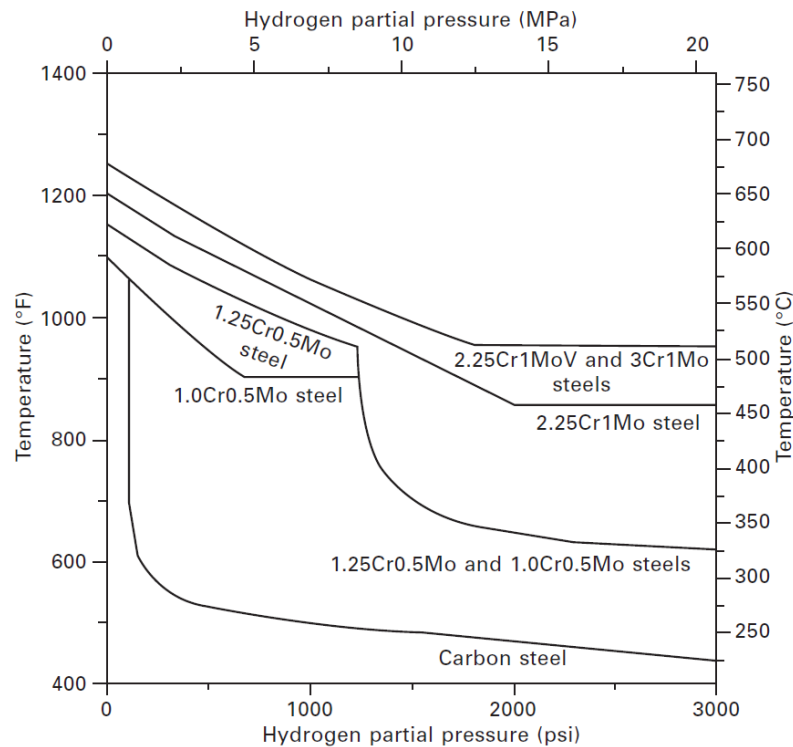


**Figure 2.19:** Nelson curves for Cr-Mo and carbon steels [65].

Low-alloy carbon steels are usually considered for piping applications, where higher temperatures or more aggressive corrosive media occur. However, the *ASME B31.12* code cautions designers against using such materials, because of the higher susceptibility to HE, since these materials normally have higher strengths than carbon steels. It is stated, that for low alloy steels, the alloying elements carbon, manganese, sulfur, phosphorus, and chromium increase the HE susceptibility. The lack of material test data



for such materials used as hydrogen components and the poor weldability are further reasons for not using this class of materials for the manufacturing of hydrogen components [57].

Austenitic stainless steels exhibit the best performance for the design of hydrogen components out of all structural metals according to *ASME B31.12*. Therefore, they have been used successfully for high pressure hydrogen components. The two most important factors affecting the HE resistance of austenitic steels are the presence of second phases and the alloy composition. Ferrite and martensite phases can significantly degrade the HE resistance. These phases can also accelerate hydrogen uptake because of the higher diffusion rates of BCC phases compared to those of FCC phases [4]. Second phases may be present in the microstructure due to processing flaws (ferrite) and/or mechanical stresses induced during processing or application (martensite). A higher nickel content increases the HE resistance, which is thought to be due to the austenite stabilizing effect of nickel. Therefore, this code suggests the use of *AISI 316* ( $> 12 \text{ wt\%}$  nickel) for hydrogen components with high requirements. With the exception of austenitic stainless steels, all other highly alloyed steels (defined in the *ASME B31.12* code as steels with  $< 90 \text{ wt\%}$  iron) are generally highly susceptible to HE. Their high strength and high concentration of alloying elements are the main reasons for this [57].

### 2.5.2 AD 2000 bulletin S2

The *AD 2000* code (2016) includes all necessary safety requirements to comply with the *European Pressure Equipment Directive (2014/68/EU)*. In addition, the *AD 2000* code is the basis for the *EN 13445* series of standards, in which unfired pressure vessels are covered. The main difference between this code and the *ASME B31.12* and *ASME BPVC-VIII-3* codes is that this code does not assume initial cracks in the material and that the lifetime assessment is based on crack initiation (S-N curve analysis) rather than on fracture mechanic testing. The *AD 2000 bulletin S2* specifies the design of components for special operating conditions (e.g. contact with hydrogen). This code covers different materials, including austenitic steels, ferritic steels, aluminum alloys, nickel alloys, copper alloys, etc., as well as different product types, such as rolled and forged steels [50]. However, only ferritic as well as quenched and tempered steels are specifically mentioned in the part of the code, that considers hydrogen components [59].

For the lifetime assessment according to *AD 2000 bulletin S2* [59] a structural stress analysis has to be performed in the first place, which can be done experimentally or by finite element method. Afterwards, the uni- or multiaxial equivalent stress range  $2\sigma_{va}$  and

the equivalent mean stress  $\bar{\sigma}_v$  of the specific load situation are calculated based on Tresca's maximum shear stress theory. For the fatigue-based lifetime assessment of pressure vessels two approaches are described in this code [50].

The first approach involves the calculation of the maximum bearable stress range  $2\sigma_{a,zul}$  to achieve a certain number of load cycles. In general, the actual stress range  $2\sigma_a$  is determined and then corrected by various semi-empirical correction factors, that account for the effects of component thickness, surface roughness, temperature, and mean stress to obtain  $2\sigma_{a,zul}$ . This code distinguishes between welded and non-welded components. To calculate  $2\sigma_a$  for a targeted lifetime for non-welded components, general design S-N curves for unnotched specimens are provided. These design curves were generated by using experimental data and conservative correction factors based on statistical calculations of failure probability and lifetime scatter. Alternatively,  $2\sigma_a$  can also be calculated with an empirical formula or taken from tabulated values for lifetimes exceeding the fatigue limit, which is defined here as  $N \geq 2 * 10^6$ . For welded components, a similar approach is used to obtain  $2\sigma_a$ . The difference is the analysis of the weld joint, which can be classified into four grades (K0 - K3). This classification is based on the notch effect of the weld seam.  $2\sigma_a$  can be obtained from design curves given for different weld classes for austenitic and ferritic forged and rolled steels. These design curves were generated from experimental data, obtained from strain and stress controlled fatigue tests carried out on welded specimens. Within this approach for welded components, the effects of residual stresses and surface roughness are already accounted and thus do not need to be considered in separate correction factors. Only the effects of wall thickness and temperature are considered with correction factors. Heat treatments that have a positive effect on the lifetime, such as stress relieving, are considered with a correction factor  $f \geq 1$  [50, 59].

The second approach in this code is the calculation of the maximum achievable number of load cycles for a given stress range. Here, the lifetime is obtained from design S-N curves and with similar correction factors as described above. However, the correction factors, that take into account fatigue effects, such as wall thickness and surface roughness are calculated iteratively [50, 59].

When operating the components in gaseous hydrogen, it must be taken into account that the previously calculated lifetime  $N_{zul}$  may be significantly lower and that fatigue failure may occur even at extremely high cycles ( $N > 10^7$ ). In general, the above mentioned methods for the calculation of  $N_{zul}$  are the basis for the lifetime assessment of hydrogen components. To consider the effects of HE on the components lifetime, the approach used for welded and non-welded components is depicted in the flowchart in Figure 2.20.

The above explained component lifetime  $N_{zul}$  is corrected by the hydrogen reduction factor,  $f_N$ , according to the following Equation:

$$N_{zul}^* = N_{zul} * f_N, \quad (15)$$

to obtain the fatigue lifetime in hydrogen atmosphere,  $N_{zul}^*$ , where  $f_N$  depends on the presence of welds, their quality and material strength. For steel bottles and seamless, non-welded pressure vessels made out of quenched and tempered steels the permissible number of load cycles  $N_{zul}$  for the calculation has to be in the range of  $10^3 \leq N \leq 5 * 10^4$ . To calculate  $N_{zul}^*$  for this case, a  $f_N$  value of 0.1 is prescribed, which is not further explained in the code. However, according to Fischer et al. [50], after applying this correction value, the remaining failure probability is approximately 0.1%.

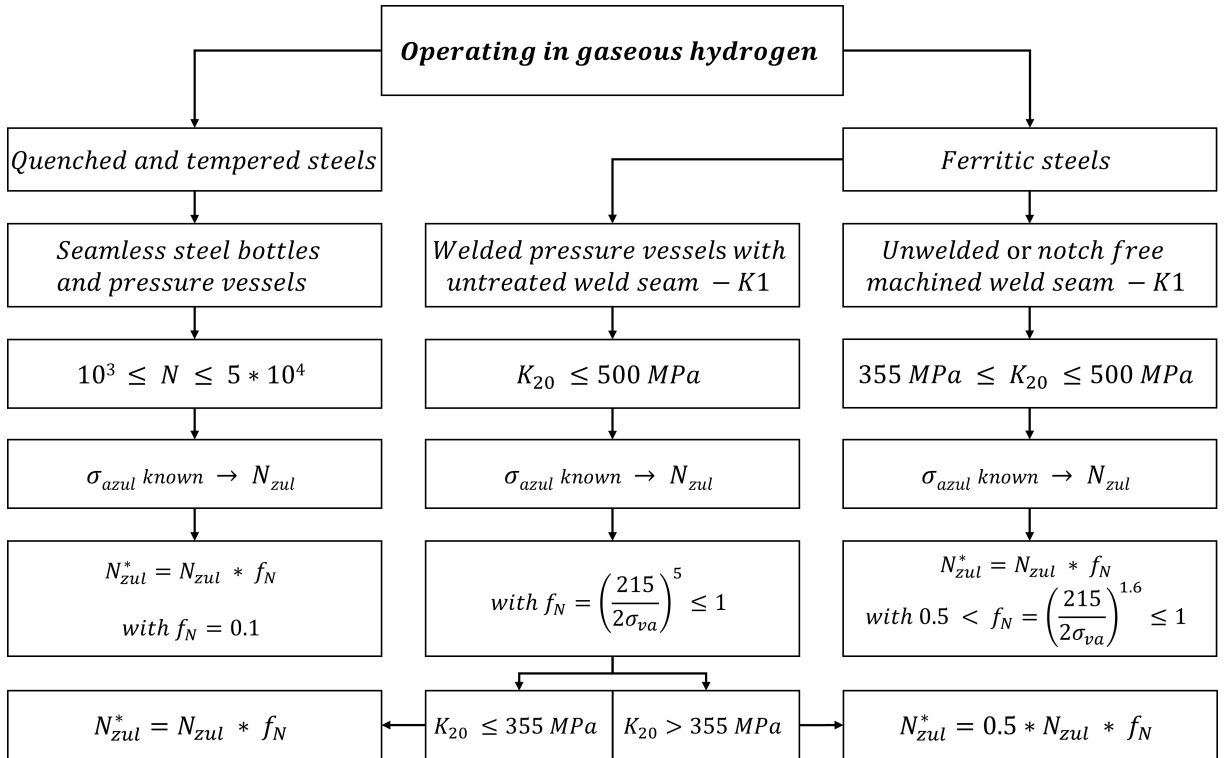


**Figure 2.20:** Lifetime assessment flowchart for welded and non-welded steel bottles and pressure vessels according to AD 2000 bulletin S2 [59].

The *AD 2000* code uses specific strength values,  $K_T$ , where  $T$  is the testing temperature. These specific strength values have to be determined for each material according to the *AD 2000 bulletin W* series. For non-welded pressure vessels made out of ferritic steel with

a strength value measured at room temperature,  $K_{20}$ , of less than 500 MPa the formula to calculate  $f_N$  is given with:

$$0.5 < f_N = \left( \frac{215}{2\sigma_{va}} \right)^{1.6} \leq 1 \quad (16)$$

For welded pressure vessels made of ferritic steel with notch free machined weld joints, Equation (16) is also valid, when  $K_{20} < 500$  MPa is true and the weld joint class is at least K1 or better [59]. For  $K_{20} < 355$  MPa,  $f_N$  can be set to 1 for non-welded pressure vessels as well as for welded pressure vessels with notch-free machined weld seams, because no detrimental gaseous hydrogen effects are assumed [50].

Welded pressure vessels made of ferritic steel with an untreated weld must have at least a K1 weld class or better and a  $K_{20}$  value below 500 MPa to be considered in this code. If  $K_{20}$  is in the range between 355 MPa and 500 MPa,  $N_{zul}^*$  is additionally multiplied by 0.5, besides the regular calculation of  $N_{zul}^*$  (visualized in Figure 2.20). This procedure is done because experimental fatigue tests have detected hydrogen cracks in welded storage tanks made of P355 and P460 steels, leading to the assumption that the strength of these steels is high enough to already show a significant susceptibility to HE [50]. The following equation describes the calculation of  $f_N$  for this case [59]:

$$f_N = \left( \frac{215}{2\sigma_{va}} \right)^5 \leq 1 \quad (17)$$

### 2.5.3 European Industrial Gases Association guideline document

The *EIGA IGC Doc 121/14* (2014) covers hydrogen pipeline systems and is a guideline for the design, maintenance, and operation of metallic piping systems, which are in contact with hydrogen or hydrogen mixtures. This document is intended as a summary of up-to-date industrial practice and is therefore not mandatory. It covers a temperature range from  $-40$  °C to  $175$  °C and hydrogen pressures between 1 MPa and 21 MPa. The focus lies on the risk prevention and management of metallic components in piping systems, which are damaged by hydrogen, through e.g. HE or stress corrosion cracking. Various materials are covered, including carbon steels, stainless steels, copper alloys, nickel alloys, etc. In addition, this document describes recommended maximum values for various material properties such as carbon equivalent, concentrations of various tramp and trace elements, hardness, and UTS. Several relevant standards are referenced for the qualification of

material properties under the influence of gaseous hydrogen, such as *ISO 11114-4* or *ASTM G142* [50].

#### **2.5.4 ASTM G142**

*ASTM G142-98* (2016) [60] standardizes quasi-static tensile testing for materials in gaseous hydrogen. This standard covers not only test equipment recommendations, but also appropriate test conditions and dimensions for smooth and notched tensile specimens. It is applicable over a wide range of temperatures and hydrogen gas pressures, although these ranges are not specified any further. However, pressures of 7 MPa, 35 MPa, and 69 MPa are suggested for the purpose of standardization. The concentration of oxygen impurities is limited to 1 ppm, and an extension rate of 0.002 mm/s  $\pm$  10 % and 0.02 mm/s  $\pm$  10 % is suggested for smooth and notched specimens, respectively. For the specified smooth specimen geometry, this extension rate of the gauge length can be translated to a nominal strain rate of  $7 * 10^{-5}$  1/s. The extension rate of the notched specimen is considered to be the extension rate of the cross-head of the testing machine and therefore no nominal strain rate is given in this standard. Additionally, it is specified that the extension rate has to be constant during testing. However, this standard only covers relevant material test conditions and does not provide instructions on how the obtained values can be used for the design of components in contact with hydrogen [50].

#### **2.5.5 ISO 11114-4**

*ISO 11114-4:2017* [61] specifies test methods and evaluation of test results for steels used in the manufacturing of seamless gas bottles with a maximum capacity of 3000 l, approved for the transport of pure hydrogen gas or hydrogen gas mixtures. This standard covers the test procedure, test apparatus, as well as specimen dimensions for three test methods (disk rupture test, fracture toughness test and hydrogen-induced crack corrosion test) in gaseous hydrogen. However, only the first two test methods are covered within the scope of this thesis. The maximum concentrations of oxygen and gaseous water impurities for all of these test methods shall not exceed 1 ppm and 3 ppm, respectively. In addition, only hydrogen partial pressures greater than 5 MPa are covered. Otherwise, it is stated that a regular design for the gas bottle is valid. The standard recommends the limitation of the UTS and the avoidance of manufacturing defects. For the use of e.g. a *34CrMo4* quenched and tempered steel, a UTS limit of 950 MPa is set. For other low-alloy steels

covered by this standard, a UTS of more or less than 950 MPa is also possible, depending on the steel used.

The first test method describes a disk test that determines the maximum gas pressure, that can be applied to a disk-shaped steel specimen before it ruptures. During testing, the applied gas pressure is continuously increased until the specimen bursts. This procedure must be performed in hydrogen gas and in a reference gas such as helium. The ratio between the burst pressure of the sample in reference gas,  $p_{He}$ , and in hydrogen gas,  $p_{H_2}$ , is then calculated. This ratio is a measure of the HE susceptibility of the material, where a higher ratio means a higher HE susceptibility. The rate of pressure increase (RPI) has an influence on this ratio, therefore the RPI with the highest ratio must be found to cover the worst-case scenario. In addition, the RPI has to be constant within each test [61].

The second test method covers the measurement of the critical stress intensity factor in a gaseous hydrogen atmosphere,  $K_{IH}$ , which is determined in a step-load test. In this standard the testing of compact tension specimens, according to *ISO 7539-6:2011* is covered. However, the specimen dimensions are included in the *ISO 11114-4:2017* standard as well. In addition to the impurity restrictions above, the hydrogen gas purity must be at least 99.9995%. Prior to testing, a predefined crack is introduced into the specimen. At the start of the test, an initial load is applied, which is equivalent to a  $K$  value of  $1 \text{ MPa}\sqrt{m}$  and this load is held for at least 20 min. Crack initiation and propagation shall be observed, using the direct current potential drop method. If no crack propagation is observed in the test time, the load is increased as specified in the standard and maintained again for at least 20 min. This procedure is repeated until the specimen fractures [50, 61].

### 2.5.6 ANSI/CSA CHMC 1

*ANSI/CSA CHMC 1* (2014) [62] covers tensile testing, fatigue testing (crack growth and lifetime assessment), as well as fracture toughness testing. For all these test methods an oxygen impurity concentration of 1 ppm or less is prescribed, which is consistent with *ASTM G142* and *ISO 11114-4*. However, for tensile testing the nominal strain rate for smooth and notched specimen is specified as  $10^{-5} \text{ 1/s}$  and  $10^{-6} \text{ 1/s}$ , which deviates from the specification in *ASTM G142*, where the strain rate for smooth specimen was seven times higher. Additionally, the strain rate for notched specimens is specified to be an order of magnitude smaller than the strain rate for smooth specimens, which is in contradiction to *ASTM G142*, where the strain rate of smooth specimens must be one order of magnitude lower than for notched specimens [50].

For fracture toughness testing, compact tension or single edge bend specimens are specified in this standard. The specimen dimensions are covered in the *ASTM E1820* standard. *ANSI/CSA CHMC 1* only covers the determination of  $K_{IH}$  in constant displacement mode tests, but not in constant load mode tests. The displacement rate is prescribed between 0.1 and 1 MPa $\sqrt{m}$ /min [50].

For the testing of crack growth due to fatigue, this standard includes compact tension, middle tension, and eccentrically-loaded single edge crack tension specimens, which are specified in *ASTM E647*. During testing,  $\Delta K_{th}$  and the crack propagation per load cycle,  $da/dN$ , are determined. The prescribed testing parameters are a frequency of 1 Hz, a sinusoidal or triangular load, and a stress ratio,  $R_\sigma$ , of 0.1. For the load-controlled fatigue lifetime assessment this standard covers specimens specified in *ASTM E466* [50]. For the strain-controlled fatigue lifetime assessment the specimens have to be in compliance with *ASTM E606*. A  $R_\sigma$  value of 0.1 or -1 is prescribed for notched or smooth specimen, respectively. For low cycle fatigue (LCF) tests the maximum allowed frequency is 1 Hz, for high cycle fatigue (HCF) tests it is 20 Hz. The threshold value between LCF and HCF is specified as  $10^5$  cycles in this standard. The waveform of the applied load is again specified as sinusoidal or triangular [50].

This standard also includes guidelines for selecting appropriate test temperatures and gas pressures. The hydrogen gas pressure applied during the test, must be at least as high as in the intended application. The test temperature must be the temperature of maximum hydrogen embrittlement (TMHE), which depends on the material used. However, for testing austenitic stainless steels, a TMHE of 220 K is recommended. For carbon and low alloy steels, *ANSI/CSA CHMC 1* recommends testing at room temperature, however, the TMHE for carbon and low alloy steels must be verified with tests at various temperatures. For the qualification of materials in contact with gaseous hydrogen, the use of relative material properties is suggested, comparing the material properties of hydrogen-charged specimens with those of uncharged specimens. *ANSI/CSA CHMC 1* suggests the use of the relative notched tensile strength (RNTS) to evaluate the hydrogen compatibility of a material. However, Fischer et al. [50] caution designers against validating hydrogen compatibility using only one specific test method, because the HE effect on the material can vary in intensity for different test methods. In addition, *ANSI/CSA CHMC 1* provides a method for calculating a hydrogen safety factor,  $SF$ , for load-controlled fatigue tests in the LCF regime.  $SF$  is calculated at four different numbers of cycles ( $1, 10^3, 10^4, 10^5$ ) by dividing the fatigue strength measured in a reference gas, such as air,  $S_R$ , by the fatigue strength measured in gaseous hydrogen,  $S_H$ . When calculating  $SF$  for 1 cycle, the notched tensile strength in reference gas,  $NTS_R$ , and in hydrogen,  $NTS_H$ , are used [50].

# 3 Methodological approach

## 3.1 Material selection

A martensitic steel as well as an austenitic steel were investigated in this thesis, as these steels show significant differences in terms of hydrogen diffusion rate and hydrogen solubility, due to their different crystallographic lattices. Therefore, the susceptibility to HE should also differ between these alloys. The chemical composition of the experimentally investigated steels can be found in Table 3.1. The first material used was a *PH13-8Mo* stainless steel, which is also known as *X3CrNiMoAl13-8-2* [68] or *1.4534* [66]. *PH13-8Mo* is a precipitation hardened steel with an excellent combination of strength and toughness. The *PH13-8Mo* material used in this thesis (the used heat treatment is covered in Section 3.1.2) has a UTS of approx. 1400 MPa and an EAF of approx. 14.3%. Its microstructure consists of a martensitic matrix with nano-sized NiAl precipitates, resulting in a precipitation-strengthening effect [69]. Depending on the heat treatment applied, significant amounts of reverted austenite can be present in the microstructure [29, 70]. Reverted austenite improves the toughness and ductility of *PH 13-8 Mo* and can lead to a significant reduction of the HE susceptibility [29, 71]. The second material used in this thesis was an *AISI 303* stainless steel, which is also designated as *X8CrNiS18-9* [68] or *1.4305* [67]. This alloy is a modified form of the

**Table 3.1:** Chemical compositions of the investigated alloys in mass percentages [66, 67].

DIN WL	PH 13-8 Mo	AISI 303
C	$\leq 0.05$	0.10
Si	$\leq 0.1$	1.00
Mn	$\leq 0.1$	2.00
P	$\leq 0.01$	0.045
S	$\leq 0.008$	0.150 - 0.350
Cr	12.25 - 13.25	17.00 - 19.00
Mo	2.00 - 2.50	-
Ni	7.50 - 8.50	8.00 - 10.00
N	$\leq 0.01$	0.10
Al	0.90 - 1.20	-
Cu	-	1.00
Fe	Bal.	Bal.



*AISI 304* alloy containing up to 0.3% sulfur, which improves machinability but reduces corrosion resistance [72]. Both *AISI 303* and *AISI 304* have a fully austenitic microstructure and are widely used in various industries mainly because of their good combination of strength and ductility as well as corrosion resistance (only *AISI 304*) [73]. The *AISI 303* material used in this thesis (the used heat treatment is covered in Section 3.1.2) has a UTS of approx. 820 MPa and an EAF of approx. 50.3%.

### 3.1.1 Diffusion calculations

The hydrogen charging process is diffusion dependent and therefore significant charging times are required to achieve a uniformly distributed hydrogen concentration near the solubility limit for bulky specimens. For laboratory testing, charging times typically range from a few hours to several days. For such charging times, the hydrogen concentration usually varies significantly from the surface to the core for bulky specimens. For austenitic steels, this effect is even more pronounced due to their extremely slow diffusion rate. Therefore, based on the mean diffusion distance of hydrogen atoms in steel, an approximate diffusion depth for hydrogen in the considered alloys has been estimated, in order to obtain useful starting parameters for hydrogen charging. The hydrogen diffusion depth is hereafter understood as the distance from the surface to the innermost layer where significant amounts of diffusible hydrogen can still be found. These calculations assume a constant hydrogen surface concentration and an initial hydrogen concentration of zero in the material. Furthermore, the diffusion of the hydrogen atoms was considered only in one dimension (normal to the surface). The assumed boundary conditions lead to the following equation [74]:

$$c(x, t) = c_R * \operatorname{erfc} \left( \frac{x}{2\sqrt{Dt}} \right), \quad (18)$$

where  $c(x, t)$  is the hydrogen concentration at location  $x$  at time  $t$ ,  $c_R$  is the constant hydrogen concentration on the surface,  $D$  is the diffusivity of hydrogen in the respective material and  $\operatorname{erfc}$  is the complementary error function. The hydrogen solubility at room temperature of *AISI 303* and *PH 13-8 Mo* was extrapolated from the data given in [75] and [76], respectively and was used as constant surface hydrogen concentration,  $c_R$ , during electrochemical charging at 50 °C. For the correct estimation of the hydrogen concentration according to Equation (18), the choice of  $D$  is crucial. The correct value for a specific alloy, in a particular condition, at a specific temperature is usually not

documented in the literature. Therefore, experimental measurements are necessary to get exact values for the specific case considered. However, for the selection of initial parameters for hydrogen charging, an approximation of the diffusion behavior is sufficient. The hydrogen diffusivity for the different materials was estimated as follows.

For *AISI 303*, the hydrogen solubility was extrapolated from the data published by Li et al. [75]. For the calculation of  $D$ , the following equation from Perng et al. [77] was used, which is valid for the very similar *AISI 304* alloy:

$$D = 7.69 * 10^{-3} * \exp\left(\frac{-53.3[kJ/mol]}{RT}\right) \quad (19)$$

For *PH 13-8 Mo*, the diffusivity at room temperature, as well as the hydrogen solubility, were linearly interpolated from the data published by Tsay et al. [76]. The diffusivity at 50 °C was estimated according to Equation (10) by using the activation energy of a *X2CrNiMoV13-5-2* steel [78], which has a similar alloy composition. This procedure yields the following formula to approximate the hydrogen diffusivity as a function of the temperature:

$$D = 0.819 * \exp\left(\frac{-43.4[kJ/mol]}{RT}\right) \quad (20)$$

### 3.1.2 Sample preparation

The *AISI 303* tensile specimen were manufactured according to DIN 50125 [79]. They were made with a smaller diameter compared to the *PH 13-8 Mo* tensile specimen, due to the slower diffusion rate of austenitic steels compared to the martensitic ones [4]. The tensile specimens were milled out of a cylindrical rod with a diameter of 8 mm. The cylindrical rod was in an annealed, as-delivered state. The exact geometry of the tensile specimen can be seen in Figure 3.1.

According to Figure 3.2, cylindrical samples were machined out of a *PH 13-8 Mo* rolled round bar with a diameter of 90 mm. These cylindrical samples were then solution-annealed for 30 min at 850 °C, air cooled and then further cooled down in cold water, in order to cool the specimen below 16 °C. This procedure is necessary to fully transform the retained austenite into martensite [80]. Subsequently, an aging treatment was applied to the samples at 552 °C (1025 °F) for 4 h. The amount of reverted austenite in the samples after aging was  $4.4 \pm 0.2$  vol.% according to the XRD measurements, as described by

Rosenauer et al. [80]. After the heat treatment, the cylindrical specimen were milled to round tensile specimen according to ASTM A370-20 [81]. The exact geometry of these specimen can be seen in Figure 3.3.

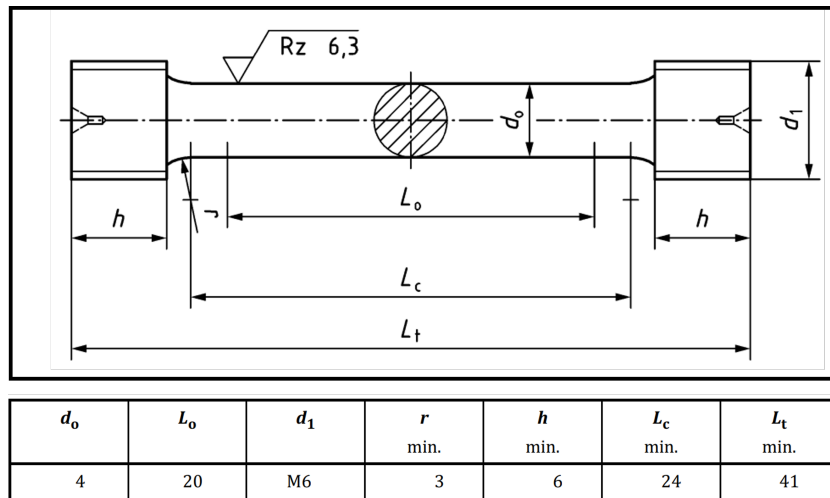


**Figure 3.1:** The geometry used for the *AISI 303* tensile specimens (measures are in mm) [79].

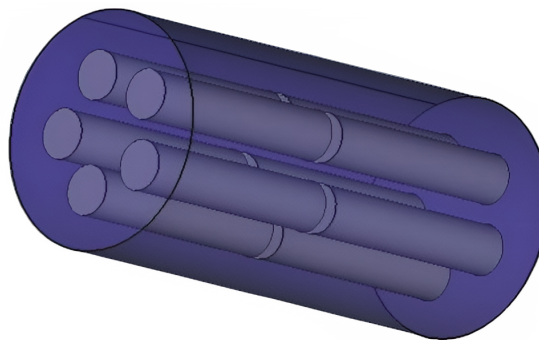


**Figure 3.2:** Schematic drawing of the location where the *PH 13-8 Mo* cylindrical specimen were taken from a rolled round bar with a diameter of 90 mm.

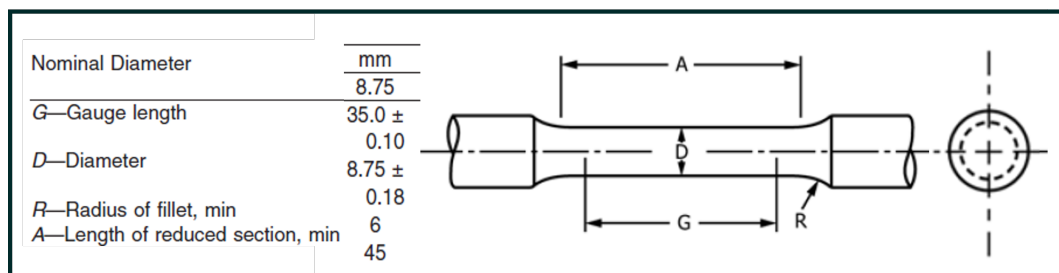


**Figure 3.3:** The geometry used for the *PH 13-8 Mo* tensile specimens [81].

### 3.1.3 Microstructural analysis

For the microstructural analysis, the threads of already tested uncharged tensile specimens were separated from the gauge section using the *Secotom-60* cutting machine from *Struers*. The specimens were embedded with the embedding material *Polyfast* in the embedding press *CitoPress-20*, both from *Struers*. Each of these specimens was ground and polished using a *Tegramin-30* grinding machine from *Struers*. The samples were ground with SiC abrasive paper up to grit size *P4000* according to *FEPA* and then polished with diamond suspensions (3  $\mu\text{m}$  and 1  $\mu\text{m}$ ) from *Struers*. To make the microstructure visible, the *PH 13-8 Mo* specimens were etched with the etchant *V2A-Beize*, whereby the etchant was heated up to 70 °C. The *AISI 303* specimens were etched at room temperature with an etchant according to *Beraha II*. The microstructure was then analyzed in a *Zeiss Axio Imager Vario* from *Carl Zeiss AG*.

## 3.2 Experimental details

### 3.2.1 Specimen assignment

Specimens of each alloy in three different conditions were subjected to tensile tests: uncharged specimens (U), charged specimens (C), as well as charged and annealed specimens (CA). Furthermore, uncharged (TU) and charged specimens (TC) of each alloy were subjected to TDS measurements. This assignment can be seen in detail in Table 3.2.

**Table 3.2:** Specimen assignment to the applied condition/measurement.

	Uncharged	Charged	Charged & annealed	TDS
<b>PH 13-8 Mo</b>	MU1 - MU3	MC1 - MC4	MCA	MTU, MTC
<b>AISI 303</b>	AU1 - AU3	AC1 - AC4	ACA1, ACA2	ATU, ATC

M ... Martensite, A ... Austenite, U ... Uncharged, C ... Charged CA ... Charged and annealed, TU ... Uncharged TDS, TC ... Charged TDS
--

### 3.2.2 Hydrogen charging and annealing

Electrochemical hydrogen charging, also known as cathodic hydrogen charging, is based on the principle of an electrochemical cell. The specimen to be charged with hydrogen acts as cathode and an inert material (usually platinum or glassy carbon) acts as anode. The cathode and anode are both submerged in an electrolyte, which is usually water-based. For high temperature cathodic charging, undiluted electrolytes (e.g. molten salts) are used. By applying an electrical potential between the cathode and anode, the electrolyte decomposes to form positively charged ions (hydrogen ions) and negatively charged ions. The hydrogen ions are attracted to the cathode by the external electric field, resulting in a local excess of hydrogen ions at the surface of the specimen. The applied potential also acts as a driving force for hydrogen diffusion into the specimen [82].

The samples were electrochemically charged with hydrogen using the setup shown in Figure 3.4. A description of the charging parameters and electrolyte compositions used

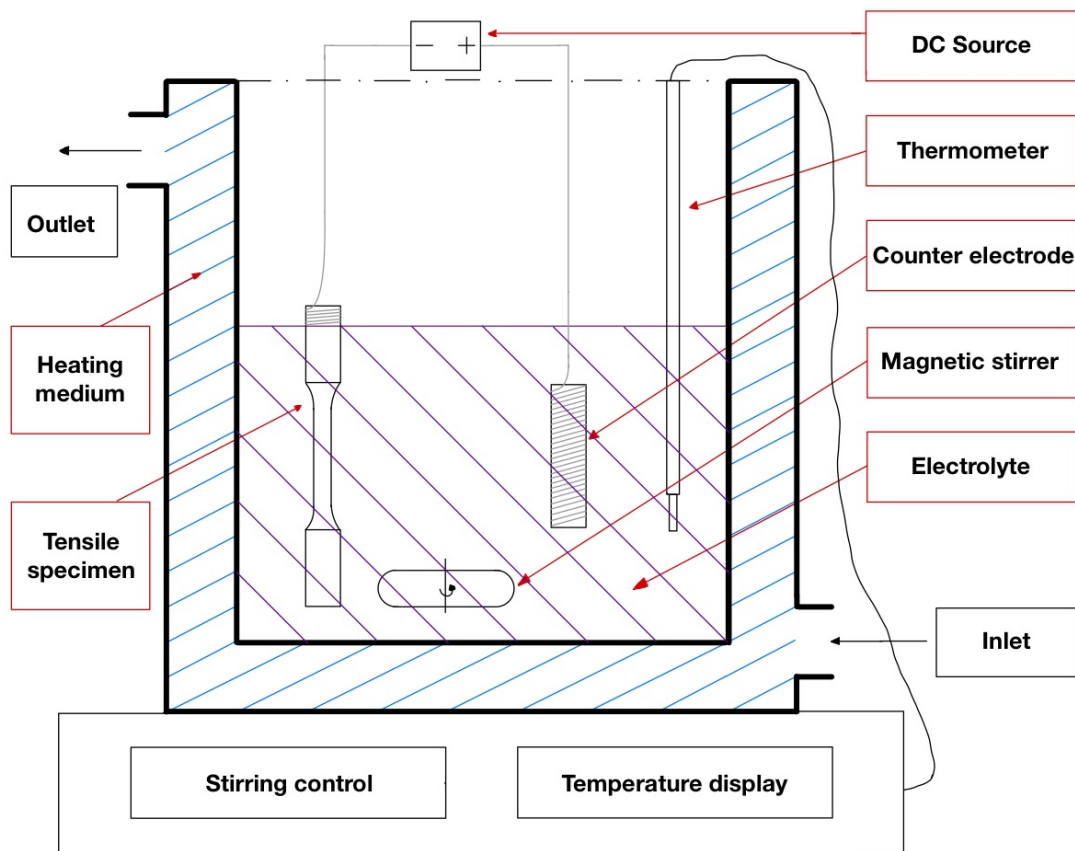


**Figure 3.4:** Schematic drawing of the hydrogen charging process.

is given in Table 3.3. However, it has to be mentioned, that the charging process of *AC2* was temporarily interrupted for about 10 h due to a power outage. The *PeakTech 6225 A* from *PeakTech Prüf- und Messtechnik GmbH* was used as DC source. A *P-3 Glassy Carbon plate* (25x25x3 mm) from *C3 Prozess- und Analysetechnik GmbH* acted as counter electrode and was connected to the DC source via a platinum wire with a diameter of 0.3 mm. The tensile specimens were connected to the DC source with standard alligator clips according to Figure 3.4. The *Heating and cooling medium, Rothitherm<sup>®</sup> M 150* from *Carl Roth GmbH + Co. KG* was used as heating medium in the thermostat *Eco E4 S* from *Lauda Dr. R. Wobser GmbH & Co. KG*.

**Table 3.3:** Hydrogen charging parameters and electrolyte compositions.

	Time [h]	Electrolyte	Current density [ $\frac{\text{mA}}{\text{cm}^2}$ ]
<b>PH 13-8 Mo</b>	20	0.5M H <sub>2</sub> SO <sub>4</sub> + 1 $\frac{\text{g}}{\text{L}}$ CH <sub>4</sub> N <sub>2</sub> S	0.15
<b>AISI 303</b>	90	1M NaOH + 1 $\frac{\text{g}}{\text{L}}$ CH <sub>4</sub> N <sub>2</sub> S	1

The hydrogen charging was done at 50 °C, to improve the hydrogen diffusivity. The longer charging times for the *AISI 303* specimen compared to the *PH 13-8 Mo* specimen were chosen due to the slow diffusion behavior of austenitic steels in comparison to martensitic steels [4]. In addition, two different electrolytes were used for hydrogen charging, as the electrolyte used for the charging of the *PH 13-8 Mo* samples could not be used for the charging of the *AISI 303* samples. This was due to the increased corrosion susceptibility of *AISI 303*. A magnified view of the corrosive attack on an *AISI 303* specimen after being charged in the sulfuric acid electrolyte for 90 h is shown in Figure A.1 in the appendix. The electrolyte used in the charging process has been replaced with unused electrolyte at regular intervals. This was done to create comparable charging conditions between the different samples. To prevent the threads of the tensile specimens from being charged with hydrogen, they were covered with Teflon<sup>™</sup> tape prior to charging. Thiourea (CH<sub>4</sub>N<sub>2</sub>S) was added to the electrolyte to decelerate the recombination of hydrogen atoms and also to accelerate the surface adsorption of hydrogen [30].

Annealing of the tensile specimen was performed to investigate whether notches were formed on the surface due to corrosive attack during hydrogen charging. In addition, this annealing after hydrogen charging was performed to investigate the influence of diffusible and non-diffusible hydrogen on the mechanical behavior of the specimen during tensile testing. The tensile specimen annealing parameters were:

- The *PH 13-8 Mo* specimen was heated up from room temperature to 200 °C at a heating rate of 1 K/min, held at 200 °C for 17 h and then cooled down to room temperature at a cooling rate of 1 K/min.
- The *AISI 303* specimens were heated up from room temperature to 200 °C at a heating rate of 0.5 K/min, held at 200 °C for 90 h and then cooled down to room temperature at a cooling rate of 0.5 K/min.

All hydrogen-charged tensile specimens were immediately mounted into the tensile testing machine and the tensile tests were started within 15 minutes after charging. For the charged and annealed specimens, there was no time limit between charging and annealing as well as between annealing and tensile testing, since the diffusible hydrogen should diffuse out of the specimens, or had already done so. The specimen undergoing a TDS measurement, were cooled in liquid nitrogen immediately after charging to slow down the hydrogen desorption in the specimen until the specimen were set up for the TDS measurement.

#### 3.2.3 Tensile testing

Tensile testing was carried out on a 250 kN universal testing machine by *ZwickRoell Testing Systems GmbH* with a software upgrade by *Messphysik Materials Testing GmbH* using a mechanical extensometer and a hydro-mechanical clamping system. All tensile tests were performed at room temperature and in accordance with ISO 6892-1:2009 [83]. Two different tensile test methods are standardized therein, whereby in this thesis the rate of stress increase was used as control parameter (referred to as method B in this standard). The tensile tests were performed on a predefined constant strain rate of 0.24 mm/min or  $1.14 * 10^{-4}$ /s for the *PH 13-8 Mo* specimen and 0.12 mm/min or  $1.00 * 10^{-4}$ /s for the *AISI 303* specimen. The choice of strain rate was made following the research of Li et al. [29], where different strain rates for tensile tests on hydrogen-charged *PH 13-8 Mo* specimens were compared regarding their influence on HEI and test time until fracture.

#### 3.2.4 Thermal desorption spectroscopy - TDS

For TDS measurements, the threads of the hydrogen-charged tensile specimen were separated from the gauge section, with each cut taking no more than 30 s. The samples were then ground on all surfaces with SiC abrasive paper (grit size P500 according to

*FEPA*) for a few seconds to remove contaminants. The specimens were cooled in liquid nitrogen after each cut and grinding step. The samples were then weighed and placed in the TDS apparatus. This procedure was also carried out on uncharged tensile specimens, which were then used as reference measurements to determine the amount of hydrogen in the uncharged specimens. The samples were heated in an *IR07* infrared furnace from *Bruker Corporation*. In combination with a *G8 Galileo* carrier gas melt extraction furnace, also from *Bruker Corporation*. During the measurement, each sample was heated with 50 K/s until it reached 950 °C, this temperature was then kept until the end of the measurement. During the measurement the hydrogen desorption rate (in ppm/s) was determined according to the schematic operating principle shown in Figure 3.5. The total amount of hydrogen in the samples was then calculated by integrating the area under the hydrogen desorption peak over time.

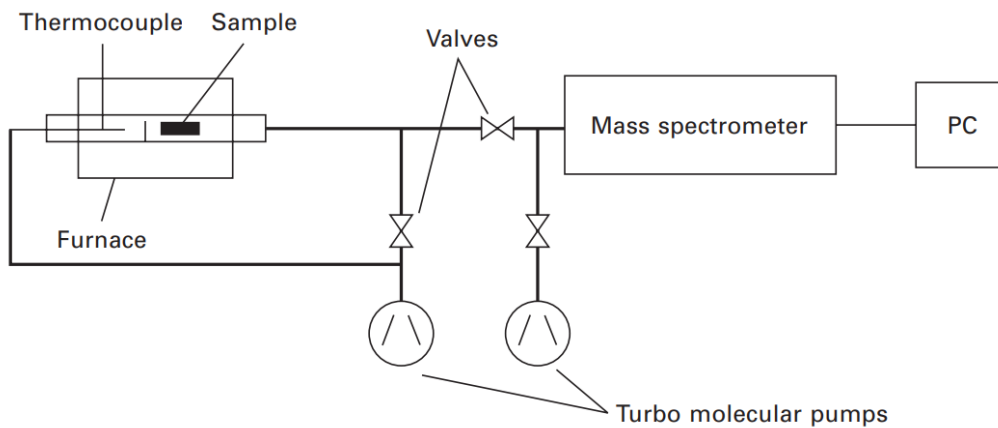


**Figure 3.5:** Schematic representation of the functional principle of a TDS measurement [84].

### 3.2.5 Fractographic analysis

For the fractographic analysis the stereo microscope *Zeiss Stereo Discovery.V20* from *Carl Zeiss AG* as well as the SEM *Tescan Clara* from *Tescan orsay holdings, a.s.* were used. Prior to the analysis in the SEM the specimen were placed in isopropyl alcohol and cleaned in an ultrasonic cleaner for 5 min. For the calculation of the ROA, the cross-sectional area of the specimens was measured using the free software *ImageJ* from *Wayne Rasband* on stereo microscope images.



## 4 Results and discussion

### 4.1 Diffusion calculations

Equation (18) has been used to plot hydrogen concentration profiles for *PH13-8Mo* (specimen radius: 4.375 mm) and *AISI 303* (specimen radius: 2 mm) tensile specimens. These profiles are plotted for 20 °C and 50 °C, in order to estimate the achievable hydrogen diffusion depth (as discussed in Section 3.1.1) in the charged specimens. For both, diffusion times from 20 h up to 120 h have been calculated. Even after 120 h of hydrogen charging at 50 °C the hydrogen diffusion depth in *AISI 303* is restricted to about 0.1 mm as shown in Figure 4.1. The hydrogen diffusion depth for the charging of *PH13-8Mo* at 50 °C for 20 h is restricted to approx. 2 mm as depicted in Figure 4.2, which is significantly larger than for *AISI 303*. At the same time, the hydrogen solubility for *AISI 303* is orders of magnitude higher than for *PH13-8Mo*.

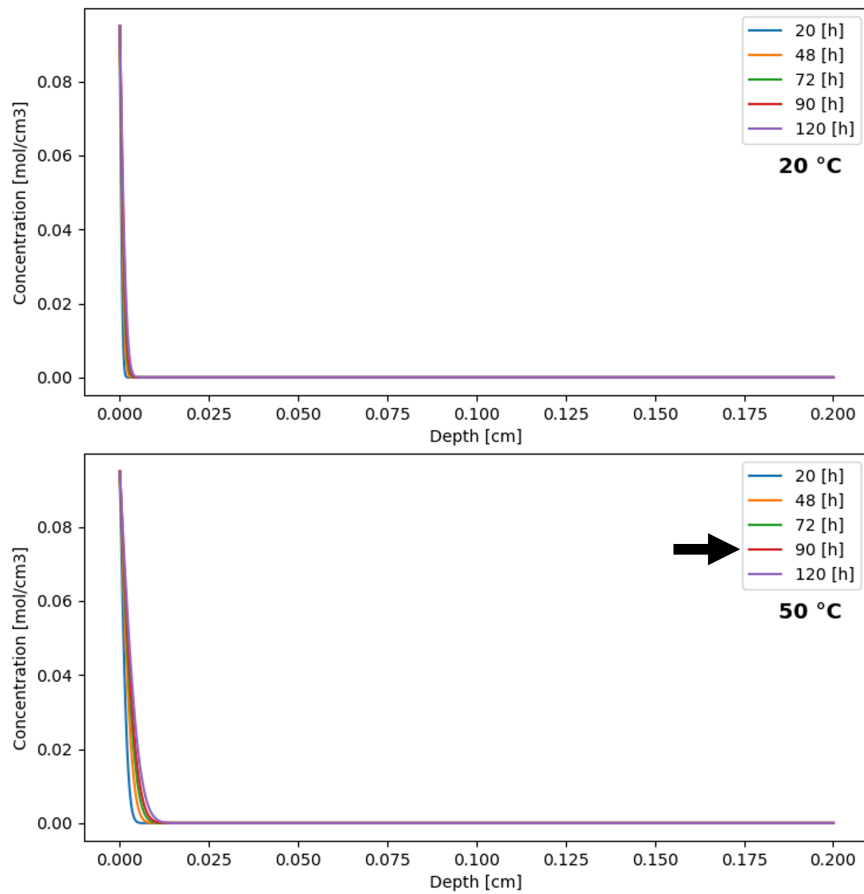


**Figure 4.1:** Estimated hydrogen diffusion depth of *AISI 303* specimens for various charging times at 20 °C (**top**) and 50 °C (**bottom**), the arrow indicates the charging duration used in this thesis.

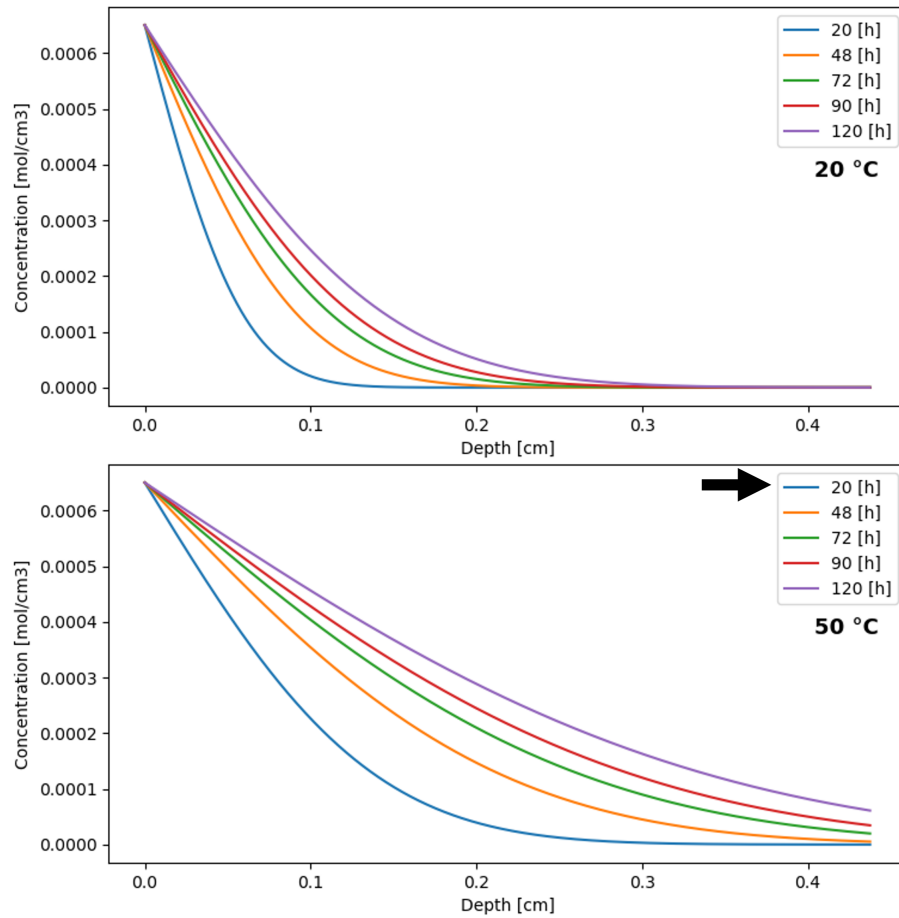


**Figure 4.2:** Estimated hydrogen diffusion depth of *PH 13-8 Mo* specimens for various charging times at 20 °C (**top**) and 50 °C (**bottom**), the arrow indicates the charging duration used in this thesis.

The estimated hydrogen solubility as well as the hydrogen diffusivity for each steel (calculated as described in Section 3.1.1) at 20 °C and 50 °C are shown in Table 4.1.

**Table 4.1:** Estimated hydrogen solubility ( $S$ ) at room temperature, as well as hydrogen diffusivity at 20 °C ( $D_{20}$ ) and 50 °C ( $D_{50}$ ), with a color code to visualize the influence of each property on the HE resistance of the materials [75–78].

	<b>PH 13-8 Mo</b>	<b>AISI 303</b>	
$D_{20}$	$1.5 * 10^{-8}$	$2.4 * 10^{-12}$	$[\frac{cm^2}{s}]$
$D_{50}$	$7.9 * 10^{-8}$	$1.9 * 10^{-11}$	$[\frac{cm^2}{s}]$
$S$	$6.5 * 10^{-4}$	$9.5 * 10^{-2}$	$[\frac{mol}{cm^3}]$
	--	-	+ +

Table 4.1 is a simplified approach to illustrate how the hydrogen diffusivity and solubility influence the HE resistance of the materials. However, it should be noted, that a higher hydrogen solubility can also lead to a higher number of strong hydrogen trap sites, which would increase the HE resistivity of the material [76]. The high hydrogen diffusivity of *PH13-8Mo* would result in a significant hydrogen concentration in the core of the specimens, when charged at 50 °C for about 300 h or more, according to Equation (18) using the data from Table 4.1. In contrast, the diffusivity of *AISI303* is about four orders of magnitude slower than that of *PH13-8Mo*. This results in a hypothetical hydrogen charging time of about 30,000 h at 50 °C to achieve a similar hydrogen concentration in the core of the *AISI303* specimens (radius: 2 mm) as in the core of the *PH13-8Mo* specimens (radius: 4.375 mm) if they were charged at 50 °C for 300 h.

Tsay et al. [76] compared differently aged *PH13-8Mo* specimens regarding their hydrogen diffusivity and solubility. Temperatures ranging from 427 °C to 593 °C were used for the various aging treatments, each with a duration of 4 h [76]. It was found that specimens aged at a higher temperature had a higher volume fraction of reverted austenite. Reverted austenite is considered to be a strong hydrogen trap [29, 30, 76], capable of absorbing hydrogen at its interfaces and within itself. Therefore, an increase in the volume fraction of reverted austenite leads to an increase in hydrogen solubility and a decrease in hydrogen diffusivity, and thus the HE susceptibility of *PH13-8Mo* can be reduced [76].

In [31, 85–88], the effect of pre-straining, i.e. straining prior to hydrogen exposure, on the HE susceptibility of different austenitic stainless steels was investigated. It has been found, that in less stable austenitic steels, austenite is partially transformed into martensite during straining. The martensitic domains act as fast hydrogen diffusion paths in the austenitic matrix, thus promoting hydrogen diffusivity in austenitic stainless steels. A nickel content of 12 wt.% or more is suggested for an improved austenite stabilizing effect [85], in order to impede the austenite to martensite transformation.

## 4.2 Microstructural analysis

Exemplary optical microscopy images of the microstructure of *PH13-8Mo* and *AISI303* are shown in Figure 4.3 (A) and (B), respectively. The microstructure depicted in Figure 4.3 (A) shows a martensitic matrix with delta ferrite grains elongated along the rolling direction. In the microstructure shown in Figure 4.3 (B), austenite grains, some containing twins, and MnS inclusions elongated along the rolling direction can be seen. These MnS inclusions are characteristic for an *AISI303* steel.

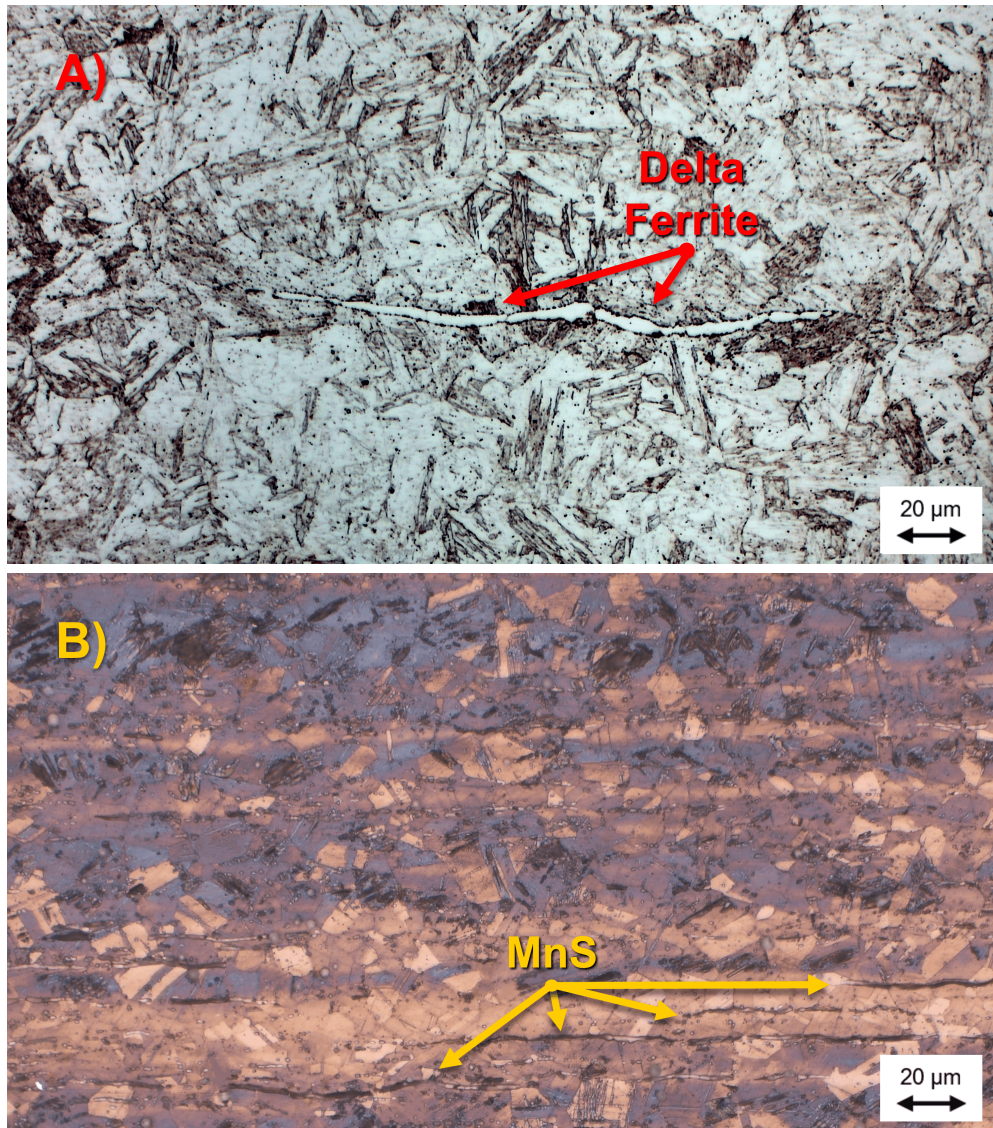


**Figure 4.3:** Exemplary microstructure of (A) *PH13-8Mo* and (B) *AISI 303* after etching (A) with *V2A-Beize* and (B) according to *Beraha II*. The arrows indicate elongated (A) delta ferrite grains and (B) MnS inclusions.

### 4.3 Tensile testing

The stress-strain curves of the *PH 13-8 Mo* and the *AISI 303* tensile tests are plotted in the Figures 4.4 and 4.5, respectively. These figures only include valid test results, i.e. all tensile specimens where the fracture surface was in the middle third of the gauge length. The tested *PH13-8Mo* specimens exhibited a high yield strength of about 1400 MPa with no significant deviations between uncharged (*MU*), charged (*MC*), and charged & annealed (*MCA*) specimens. An EAF of over 14% was measured for the *MU* specimens.

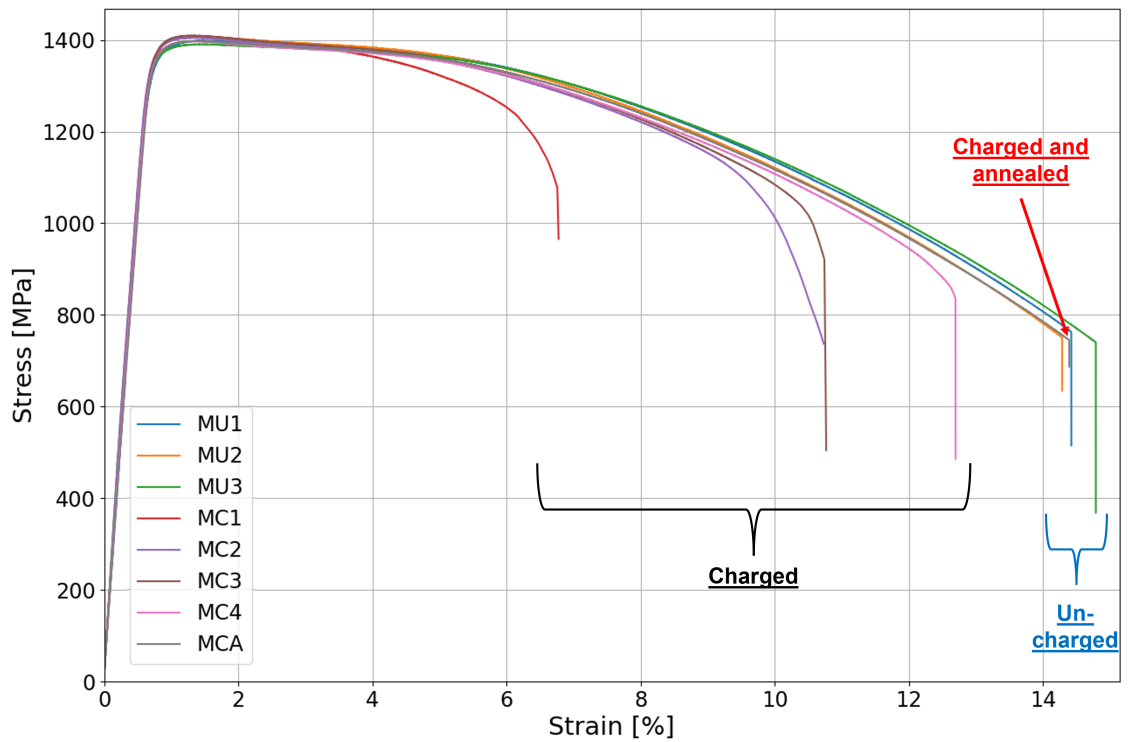


**Figure 4.4:** Stress-strain curves from tensile tests of uncharged (MU), charged (MC) as well as charged & annealed (MCA) PH 13-8 Mo tensile specimens.

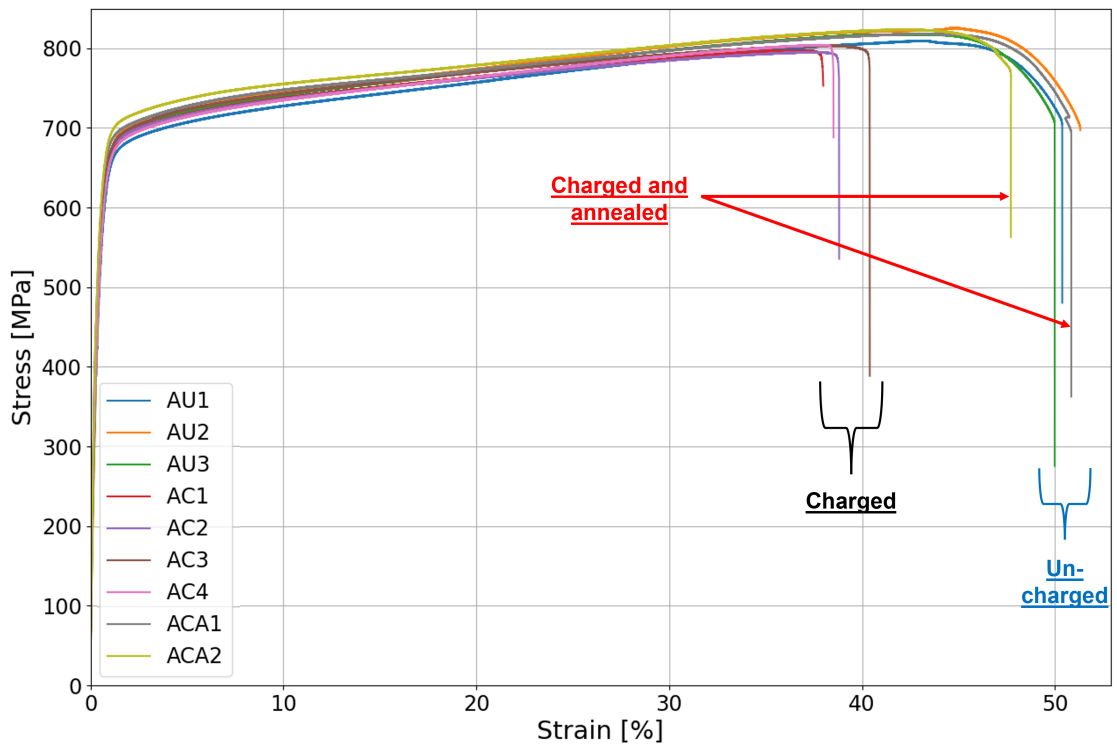


**Figure 4.5:** Stress-strain curves from tensile tests of uncharged (AU), charged (AC) as well as charged & annealed (ACA) AISI 303 tensile specimens.

The deviations between the *MU* as well as between the *MCA* and the *MU* specimens were minor. A significant reduction of EAF was measured for the *MC* specimens compared to the *MU* specimens. For the *MC* specimens a very high variance of EAF was observed.

The tested *AISI 303* specimens exhibited a yield strength of about 500 MPa with no noticeable scatter between the uncharged (*AU*) and charged (*AC*) specimens. A minor decrease of the UTS was observed for the *AC* specimens with regard to the *AU* specimens. A very high EAF of about 50 % for the *AU* specimens, as well as a significant deterioration of the EAF was measured for the *AC* specimens compared to the *AU* specimens. The scatter between the different *AC* specimens, as well as the scatter between the different *AU* was small, which indicates good data reproducibility. The charged & annealed (*ACA*) specimens exhibited only minor or virtually no difference to the *AU* specimens.

Table A.1 in the appendix contains the EAF, ROA, UTS, and 0.2 % proof stress,  $Rp_{0.2}$ , of all tested tensile specimen. Table 4.3 lists all HEI values based on the EAF ( $HEI_{\delta}$ ) and based on the ROA ( $HEI_{\phi}$ ) of all charged specimens, which were calculated in relation to the mean EAF and ROA of the respective uncharged specimens, according to the Equations (13) and (14). The mean,  $\mu$ , and the standard deviation,  $\sigma$ , of all these values in (%) for all specimens are expressed as  $\mu \pm \sigma$  in the Tables 4.2 and 4.3.

The scatter of the EAF and the ROA values of the different *MU* specimens was not significant, resulting in small standard deviations for these values. On the other hand, there were large deviations between the EAF and the ROA values of the different *MC* specimens. In particular, *MC1* differed greatly from the corresponding properties of *MC2* and *MC3*. It is assumed that *MC1* had pre-existing surface defects, that led to premature failure. Therefore, the *MC1* specimen is considered an outlier.

The charging and annealing procedure used for the *CA* samples was similar to that used in [23], where the samples were heated to 200 °C to remove the diffusible hydrogen from the sample. However, the strongly bound and therefore non-diffusible hydrogen was not removed from the samples at 200 °C in [23]. This means, that a significant amount of non-diffusible hydrogen remains in the *CA* specimens after annealing. It is a strong indication that the electrochemical hydrogen charging did not significantly alter the surface quality of the specimens and that no harmful notches were introduced. Furthermore, the almost identical EAF and ROA values between the *MCA* and the *MU* specimens support the theory stated in various publications [4, 22, 23, 51] that only diffusible hydrogen in the material leads to HE.



**Table 4.2:** Mean,  $\mu$ , and standard deviation,  $\sigma$ , of EAF, ROA, UTS, and  $R_{p0.2}$  of the charged (C) and uncharged (U) samples and the individual values of the charged & annealed (CA) samples.

	Sample	EAF [%]	ROA [%]	UTS [MPa]	$R_{p0.2}$ [MPa]
$\mu$	<b>MU1-3</b>	14.28	67.44	1399	1362
$\pm \sigma$		$\pm 0.27$	$\pm 0.61$	$\pm 7$	$\pm 12$
$\mu$	<b>MC1-4</b>	9.95	40.01	1405	1375
$\pm \sigma$		$\pm 2.23$	$\pm 18.3$	$\pm 5$	$\pm 6$
	<b>MCA</b>	14.07	67.61	1398	1372
$\mu$	<b>AU1-3</b>	50.29	57.75	818	514
$\pm \sigma$		$\pm 0.46$	$\pm 1.04$	$\pm 7$	$\pm 11$
$\mu$	<b>AC1-4</b>	38.67	31.35	800	514
$\pm \sigma$		$\pm 0.96$	$\pm 1.48$	$\pm 4$	$\pm 25$
	<b>ACA1</b>	50.68	60.13	818.5	558.8
	<b>ACA2</b>	47.45	50.04	823.6	571.5

**Table 4.3:**  $HEI_{\delta}$  and  $HEI_{\phi}$  of all charged (C) specimens, including mean,  $\mu$ , and standard deviation,  $\sigma$ , values.

	<b>PH 13-8 Mo</b>	$HEI_{\delta}$ [%]	$HEI_{\phi}$ [%]	<b>AISI 303</b>	$HEI_{\delta}$ [%]	$HEI_{\phi}$ [%]
	MC1	53.25	85.88	AC1	24.86	48.90
	MC2	26.00	31.90	AC2	23.23	44.45
	MC3	25.73	31.12	AC3	20.09	42.23
	MC4	12.43	13.79	AC4	23.81	47.28
$\mu$	-	29.35	40.67	-	23.00	45.72
$\pm \sigma$	-	$\pm 14.9$	$\pm 27.1$	-	$\pm 1.78$	$\pm 2.57$

For further research, more charged *PH 13-8 Mo* specimens should be tested to determine reproducible values with a low standard deviation. In addition, more *MCA* specimens should be tested to improve the reproducibility of the results. However, the results obtained for the *MCA* specimen show virtually no difference from those obtained for the *MU* specimens, suggesting that the before mentioned theory of diffusible hydrogen and traps [4, 22, 23, 51] is valid and that plausible values have been measured.

The obtained EAF and ROA of the tested *AISI 303* specimens did not vary significantly for each specimen condition. Therefore, low standard deviations were obtained for *AC*,

*AU* and *ACA* specimens. Furthermore, the results measured on the *ACA1* specimen were almost identical to those obtained for the *AU* specimens, while the results of the *ACA2* specimen differed slightly from those of the *AU* specimens. However, this deviation is not significant enough to say that the remaining non-diffusible hydrogen in the sample resulted in substantial HE. For further research, more *ACA* specimens should be tested for a better reproducibility of the obtained values.

The scatter of the UTS and the  $R_{p0.2}$  values of the *MU*, *MC* and *MCA* specimens was small. This is in agreement with the results of Li et al. [29], which tested similarly aged and charged specimens at a strain rate of  $3.33 * 10^{-4} s^{-1}$ . However, it was found that for *PH13-8Mo* specimens aged at about 540 °C, the deviation between the uncharged and charged UTS is strongly dependent on the strain rate applied. At a strain rate of  $2 * 10^{-5} s^{-1}$  the charged UTS dropped to about 55 % of its uncharged value. A possible explanation for the significant loss of UTS in the charged state at very slow strain rates is the HEDE mechanism [29, 30], as discussed in detail in Section 2.3.1. In contrast to the UTS, the  $R_{p0.2}$  is suspected to increase for hydrogen-charged specimens, due to the solution strengthening effect of hydrogen or hydrogen clusters. The necessity of very slow strain rates to significantly degrade UTS may be explained by the need to allow sufficient time during deformation for hydrogen to diffuse to critical crack initiation sites. A similar dependence for slow strain rates applies to the increase of  $R_{p0.2}$ , where the hydrogen atoms need sufficient time to diffuse to and interact with dislocations [29]. This solution strengthening effect was not observed in the stress-strain curves of *PH13-8Mo* (see Figure 4.4) as the differences between the charged and uncharged  $R_{p0.2}$  were not significant. The influence of hydrogen on the yield strength is strongly dependent on the chemical composition and microstructure of the steel. For low-carbon steels, silicon steels, and low-alloy steels it was reported [30], that hydrogen had no influence on the yield strength at all. In contrast, for the austenitic stainless steel *AISI 310s*, Abraham et al. [89] stated that hydrogen increased the yield strength significantly for high hydrogen concentration and very slow strain rates. However, the solution strengthening effect of hydrogen was found to be weaker than that of nitrogen and carbon. This is in contradiction to the results of this thesis, where the  $R_{p0.2}$  of the *AU* and the *AC* specimen was almost identical. A slight reduction of the UTS between *AU* and *AC* was observed, which may be explained by the loss of cohesive strength due to the HEDE mechanism [29, 30]. Zhou et al. [87] reported a significant loss of UTS for electrochemically charged specimen in comparison to uncharged *AISI 304* specimen at very low strain rates. Wang et al. [31] were able to show for a *AISI 304L*, for a similar strain rate and charging conditions as used in this thesis, that the  $R_{p0.2}$  was almost identical for uncharged and charged specimens.



However, the UTS of the charged specimen was slightly lower than that of the uncharged specimen in [31]. These results are consistent with the results of this thesis.

When comparing the HEI values from Table 4.3, it can be seen, that there are generally significant differences between the  $HEI_{\delta}$  and the  $HEI_{\phi}$  values for the same sample. This is consistent with the results obtained by Wang et al. [31], where different *AISI 304L* specimens were compared regarding their  $HEI_{\delta}$  and  $HEI_{\phi}$  values. For the *AC* specimens it can be seen, that a very low standard deviation was determined for the  $HEI_{\delta}$  as well as for the  $HEI_{\phi}$ . In contrast, for the *MC* specimens a large standard deviation for both HEI values was obtained. This is primarily due to the outlier *MC1*. When the results of *MC1* are excluded, the calculation of the mean and standard deviation of the  $HEI_{\delta}$  and the  $HEI_{\phi}$  yields  $21.39\% \pm 6.33\%$  and  $25.60\% \pm 8.36\%$ , respectively. Comparing these values with the corresponding values of the *AC* specimens, it can be seen that the *AISI 303* and *PH 13-8 Mo* specimens have very similar  $HEI_{\delta}$  values. This can be explained by the fact that both materials have a similar relative decrease in their EAF due to HE. However, the  $HEI_{\phi}$  values of the *AISI 303* specimens are significantly higher than those of the *PH 13-8 Mo* specimens. This can be explained by the fact, that the *AISI 303* specimens have a higher relative decrease in ROA due to HE than the *PH 13-8 Mo* specimens.

According to Li et al. [29] the HEI for differently aged *PH 13-8 Mo* specimens has a local minimum in the tested range (540 °C - 750 °C) at 650 °C, which is attributed to the high amount of reverted austenite in the specimen. The specimens aged at higher temperatures (e.g. 750 °C) exhibit a high susceptibility to HE, which is assumed to be due to the high amount of unstable reverted austenite transforming back to martensite. The observations of Li et al. [29] and Tsay et al. [76] are consistent because a high amount of reverted austenite is assumed to reduce the amount of diffusible hydrogen (*peak 1 hydrogen*) in the specimen, since reverted austenite is known to be a strong hydrogen trap. The HEI is known to be decreasing for decreasing amount of (*peak 1 hydrogen*) [23, 29, 51]. Tan et al. [90] investigated the influence of three different heat treatment routes on the HEI for electrochemically charged *PH 13-8 Mo* specimens. The austenite contents in the three different states were 0 vol.%, 9.3 vol.%, and 13.2 vol.%. The corresponding  $HEI_{\delta}$  values were 52 %, 22 %, and 14 %, again showing the beneficial effect of a higher austenite fraction on the HE resistivity of *PH 13-8 Mo* steels. The austenite content of the *PH 13-8 Mo* specimens tested in this thesis was 4.4 vol.%. The corresponding mean  $HEI_{\delta}$  was 23 %, which is only slightly higher than the corresponding value of the specimen containing 9.3 vol.% austenite. This deviation may be explained by the one order of magnitude slower applied strain rate and the therefore more pronounced HE of the specimens tested

in [90]. This means, that for a *PH 13-8 Mo* specimen with an austenite content of 4.4 vol.% tested at a similar strain as in [90], a  $HEI_{\delta}$  closer to 52% is expected.

There is very little tensile test data on HE of *AISI 303* steels available in the literature. In addition, the available data cannot be used for meaningful comparisons, because the test parameters for electrochemical charging were either completely different or even gaseous hydrogen charging has been used. Therefore, other but similar austenitic stainless steels of the *AISI 300* series, that have been electrochemically charged with hydrogen under comparable charging and testing conditions, are used for benchmarking. When comparing the here obtained HEI values with corresponding values of a *AISI 304L* steel from Wang et al. [31], the influence of the slightly different chemical composition between the *AISI 303* and *AISI 304L* steels on the HEIs can be examined. The values obtained by Wang et al. were 6.9% and 15.5% for  $HEI_{\delta}$  and  $HEI_{\phi}$ , respectively. However, this comparison must be treated with caution because different charging conditions were used. The most significant differences between the conditions used in this thesis and those used in [31] are the 50 times higher current density and the applied strain rate, which was about 3 times faster than in this thesis. The influence of the strain rate on the relative ROA can be seen in Figure 2.12 in the right graph. It has been shown by Li et al. [75] that the applied current density during cathodic hydrogen charging has an influence on the hydrogen permeation rate, because of the faster hydrogen evolution at the sample surface. It was shown, that the  $HEI_{\delta}$  value decreases with increasing strain rate for a *AISI 316L* steel by Astafurova et al. [91] and for a *AISI 304* steel by Kim et al. [92]. It can be seen that the *AISI 303* steel investigated in this thesis has a higher HE susceptibility than the *AISI 304L* steel, when comparing the HEI values. This can be explained by the theory, that for austenitic stainless steel, the HE susceptibility mainly depends on the ability of the material to stabilize austenite [31, 85]. Therefore, metastable austenitic grades such as *AISI 303*, *AISI 304*, or *AISI 316* are prone to form strain-induced martensite during deformation [31, 93, 94]. This is due to the inherent HE susceptibility of the martensitic phase, which can be explained by the comparatively high hydrogen diffusivity. It is suggested in the literature [85, 86], that strain-induced martensite acts as a fast diffusion path for hydrogen in the lattice, resulting in high local hydrogen concentrations. Stable austenitic stainless steels, such as *AISI 309* or *AISI 310* are generally less susceptible to HE [31, 94, 95]. It was found, that *AISI 309* and *AISI 310* did not show significant HE in hydrogen-containing atmospheres, however, they are still susceptible to HE after cathodic hydrogen charging [94, 95]. Therefore, it was found, that the HEI of austenitic stainless steels decreases with an increasing nickel content, due to the austenite stabilizing effect of nickel. A nickel content of 12 wt.% or more is suggested for an improved HE resistance

also at low temperatures [85]. The nickel content of the *AISI 303* samples tested in this thesis was between 8% and 10%. Furthermore, this steel contains significant amounts of MnS, which can act as irreversible hydrogen traps [96–98] and favorably influence the HE resistance. However, there are contradictory considerations for MnS in the literature [99], as it has been reported that MnS inclusions can also act as reversible hydrogen traps [99,100], whereas the trapping efficiency depends on the sulfur content [100]. As a result, they can act as nucleation sites for hydrogen-induced cracks [99,101] or hydrogen blisters [98]. Large and elongated MnS inclusions are described as especially detrimental, as they increase the susceptibility to hydrogen-induced cracking [99]. MnS inclusions located on the surface are described as particularly harmful in [98], as they promote hydrogen entry into the bulk due to the release of H<sub>2</sub>S. In summary, the low nickel content and high fraction of elongated MnS inclusions result in increased HE susceptibility. These circumstances may explain the high HE susceptibility of *AISI 303*, which is atypical for an austenitic stainless steel.

## 4.4 Thermal desorption spectroscopy - TDS

The total amount of hydrogen of the *PH 13-8 Mo* and the *AISI 303* charged and uncharged specimens are listed in Table 4.4 (see Table 3.2 for specimen assignment). The hydrogen desorption rate in (ppm/s) as a function of the specimen temperature for the *MTU*, *MTC*, *ATU*, and *ATC* specimens can be seen in the Figures A.2 and A.3 in the appendix.

**Table 4.4:** Total amount of hydrogen measured in the TDS samples.

Sample	MTU	MTC	ATU	ATC
Hydrogen content [wt.ppm]	0.0980	1.4285	3.1747	6.1331

In Table 4.4 it can be seen that the hydrogen concentration in the uncharged *ATU* sample was higher than in the charged *MTC* sample. This emphasizes the large difference in hydrogen solubility between martensitic and austenitic steels. Nevertheless, the relative increase in hydrogen content between the *MTU* and *MTC* samples is significantly higher than between the *ATU* and *ATC* samples, despite the fact that longer charging times were used for the *ATC* sample than for the *MTC* sample. This can be explained by the difference in hydrogen diffusivity of several orders of magnitude between martensitic and austenitic steels [4].

Tan et al. [90] found, that for a *PH 13-8 Mo* specimen, which was electrochemically charged for 24 h in 0.1 M NaOH at a current density of 0.05 mA/cm<sup>2</sup>, the hydrogen content was between 2.28 wt.ppm and 2.95 wt.ppm, depending on the heat treatment used. The higher amount of hydrogen in the samples by Tan et al. [90], than in the *MTC* sample can be explained by the longer hydrogen charging time compared to the charging time used in this thesis. In addition, the specimen with the highest amount of hydrogen (2.95 wt.ppm) in [90] contains 13.2 vol.% austenite, which is known to be a strong hydrogen trap [76] and therefore, samples containing a high amount of austenite have a higher hydrogen solubility [76, 90]. For comparison, the austenite content of the *PH 13-8 Mo* specimens tested in this thesis was 4.4 vol.%.

Shubina-Helbert et al. [102] found, that for an *AISI 304L* specimen, which was electrochemically charged for 16.67 h in 0.1 M NaOH at a current density of 2 mA/cm<sup>2</sup>, the hydrogen content was about 2.3 wt.ppm. The hydrogen concentration in an uncharged reference sample was approx. 0.9 wt.ppm. Explanations for the deviation between the charged specimens in [102] and this thesis are the significantly longer charging time and the presence of MnS inclusions on the surface in the herein tested specimen, both of which are known to increase hydrogen uptake [98]. As described above, MnS inclusions act as hydrogen traps, which may explain the differences in hydrogen concentration between the uncharged specimen in this thesis and in [102].

## 4.5 Fractographic analysis

The stereo-microscopic images of the fracture surfaces of uncharged, charged, as well as charged & annealed tensile specimens are shown in the Figure 4.6 for *PH 13-8 Mo* specimens and in the Figure 4.7 for *AISI 303* specimens.

The fracture surfaces of *MU2* and *MCA* are relatively similar. Both specimens fractured in a cup and cone manner along approx. 90° of the direction of the applied tensile load, undergoing severe necking prior to fracture. Neither specimen shows any visible cracks on its lateral surface. In contrast, the fracture surface of the *MC3* specimen has a jagged appearance with a large height difference between the edge and the center of the fracture surface. In addition, multiple lateral cracks can be seen in the necked area on the surface, and the specimen showed relatively little necking. Both are indicative of hydrogen-induced loss of ductility. When comparing the *AU1*, *AC1* and *ACA1* specimens, the same descriptions apply, with the only difference that all specimens show less necking than the corresponding martensitic specimens.

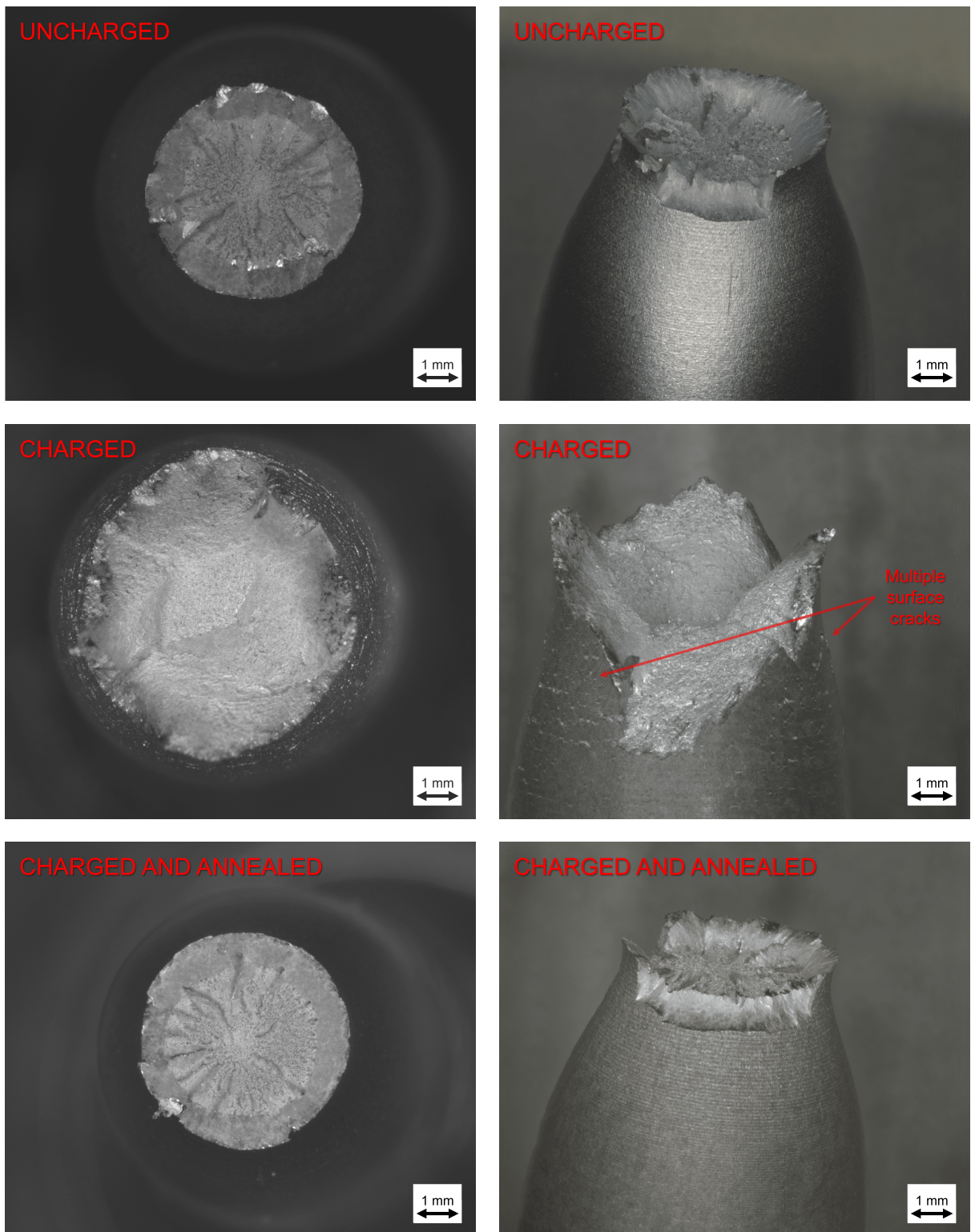


**Figure 4.6:** Top and side view of the fracture surfaces of the MU2 (**top**), MC3 (**middle**) and MCA (**bottom**) specimens.



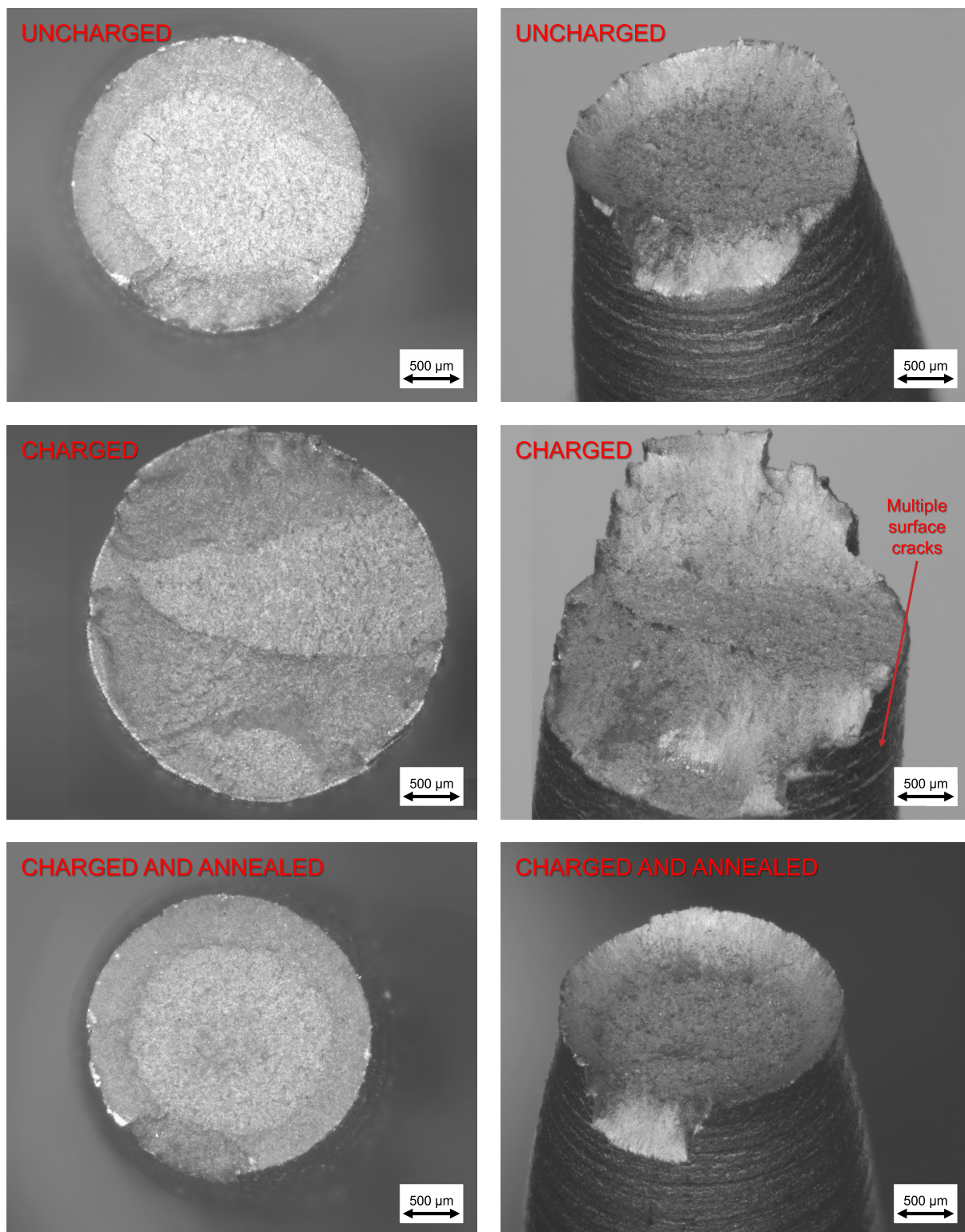


**Figure 4.7:** Top and side view of the fracture surfaces of the AU1 (**top**), AC3 (**middle**) and ACA1 (**bottom**) specimens.

The fracture surfaces of uncharged, charged, as well as charged & annealed specimen were analyzed through SEM. The results for uncharged and charged *PH13-8Mo* and *AISI303* specimens can be seen in the Figures 4.8 and 4.9. The results for charged and charged & annealed *PH13-8Mo* and *AISI303* specimens can be seen in the Figures A.4 and A.5 in the appendix. Additionally, a SEM image of the lateral cracks of the *MC2* specimen is depicted in Figure A.6 in the appendix.

The fracture surface of *MC1* contains ductile regions in the core, brittle regions on the edge of the specimen and a mixed region in between, visible in Figure 4.8 (D). The type of fracture in the brittle regions can be described as intergranular quasi-cleavage fracture, which can be seen in Figure 4.8 (E) and (F). An exact measurement of the brittle zone depth, i.e. the distance from the edge of the fracture surface to the brittle-ductile junction is not possible, because of the irregular shape of the ductile to brittle transition region. This brittle zone depth is of interest, because it can be used as a measure of the achievable hydrogen diffusion depth within the material during charging. The maximum of the brittle zone depth of the *MC1* specimen is approx. 750  $\mu\text{m}$  as depicted in Figure 4.8 (D).

The fracture surface of the *MU2* and the *MCA* specimens are very similar and consist of shear lips within the regions near the edge and a ductile region in the center, containing many cracks, which are oriented in radial direction, visible in Figure 4.8 (A) and in Figure A.4 (D) in the appendix. In the center, the fracture morphology can be described as dimple fracture, as shown in Figure 4.8 (B). The shear lips at the edge of the fracture surface can be seen at higher magnification in Figure 4.8 (C). Similar SEM micrographs of the fracture surfaces of charged and uncharged *PH13-8Mo* specimens can be seen in [30]. The fracture morphology there is also described as dimple fracture in the ductile region near the center and as intergranular quasi-cleavage fracture near the edges. In [30], differently aged but equally charged specimens are compared regarding their brittle zone depth. The aging temperature was fixed at 650  $^{\circ}\text{C}$  but the aging time was varied leading to brittle zone depths in the range between 480  $\mu\text{m}$  and 942  $\mu\text{m}$ . These values correspond well to the brittle zone depth of 750  $\mu\text{m}$  of the *PH13-8Mo* specimens tested in this thesis (see Figure 4.8 (D)). The fracture morphology demonstrated in Figure 4.8 was similar also in other *PH13-8Mo* specimens tested in this thesis, as depicted in the appendix, in Figure A.4.



## 4 RESULTS AND DISCUSSION

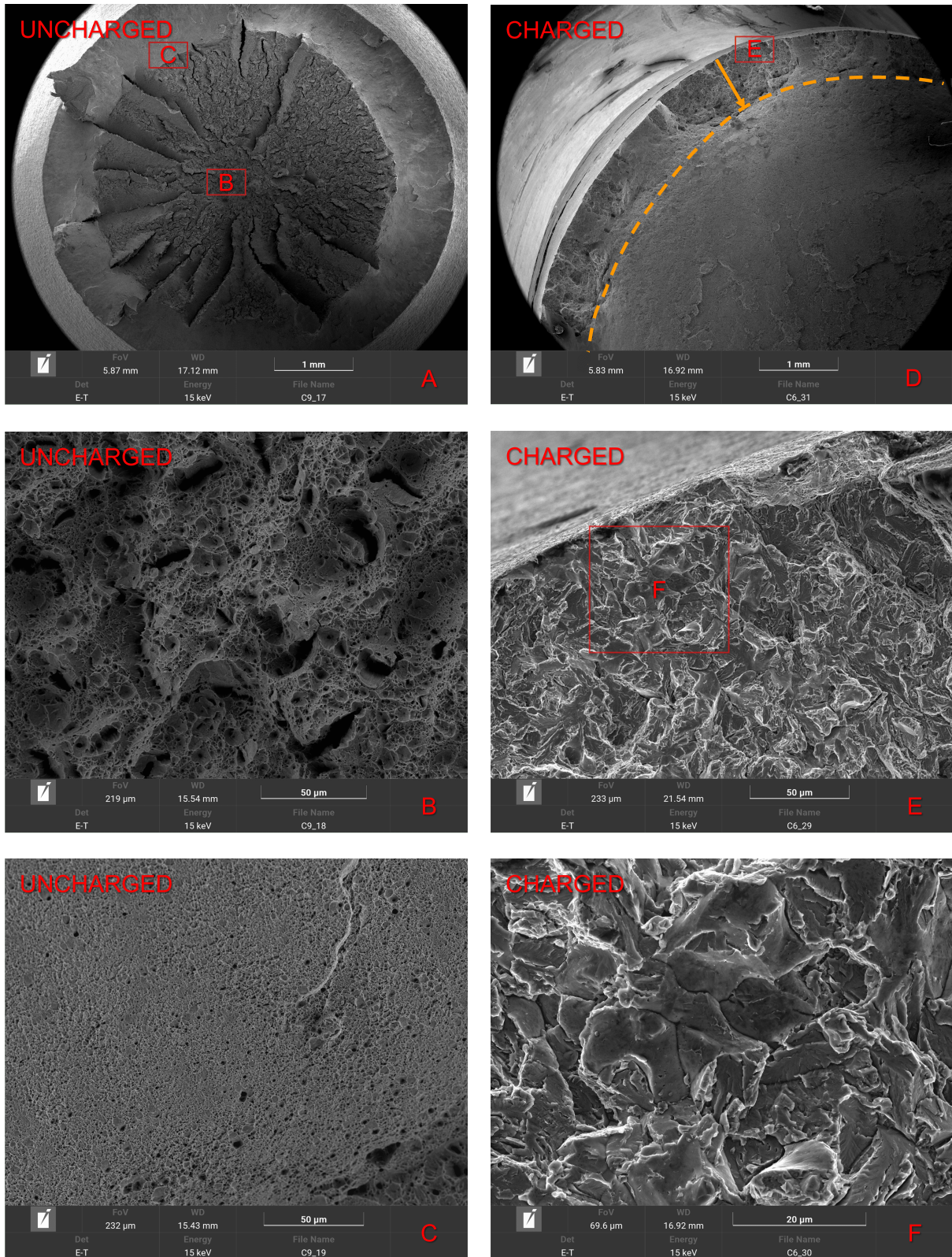


**Figure 4.8:** Fracture surfaces of the *PH 13-8 Mo* specimens MU2 (A-C) and MC1 (D-F), the red squares indicate where the respective magnified area below is located.



## 4 RESULTS AND DISCUSSION

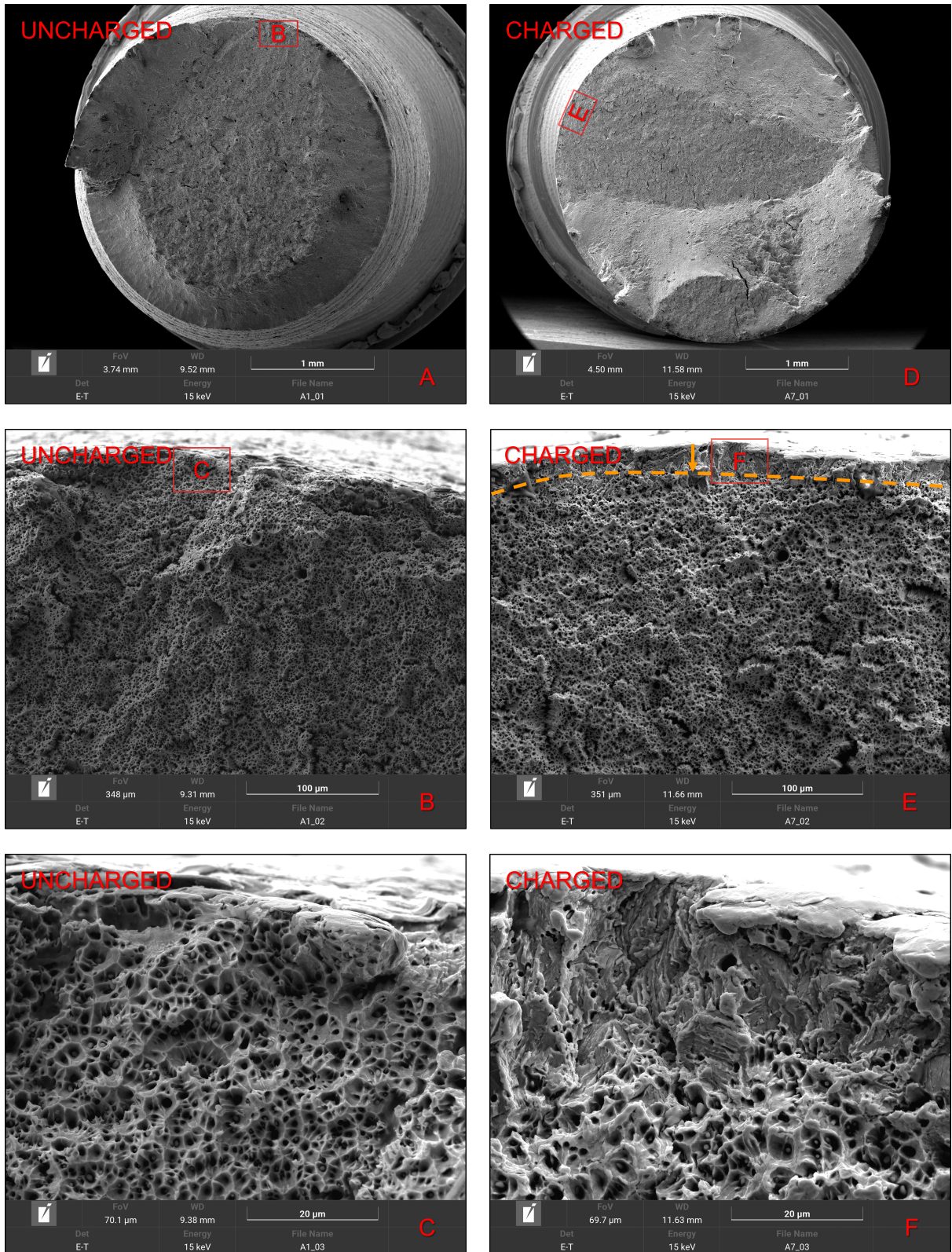


**Figure 4.9:** Fracture surfaces of the *AISI 303* specimens AU1 (A-C) and AC3 (D-F), the red squares indicate where the respective magnified area below is located.

The fracture surfaces of *AU1*, *AC3* and *ACA2* consist of almost completely ductile fracture zones, with a dimple fracture morphology (depicted in Figure 4.9 (B), (C), (E) and (F) and in Figure A.5 in the appendix). *AU1* fractured in a cup and cone manner, as shown in Figure 4.9 (A). The fracture surface of the charged specimen has a jagged appearance with a large height difference between the edge and the center of the fracture surface (visualized in Figure 4.9 (D)). The charged specimen shows small brittle regions with quasi-cleavage fracture features at the very edge of the fracture surface, with a brittle zone depth between approx. 20  $\mu\text{m}$  and 30  $\mu\text{m}$  (depicted in Figure 4.9 (E) and (F)). Wang et al. [31] reported a brittle zone depth of about 55  $\mu\text{m}$  for an electrochemically charged *AISI 304L* steel, for which higher charging times and current densities were used. There, the fracture morphology of the brittle region of the charged specimen is also described as quasi-cleavage. Besides the different charging conditions, it is assumed that MnS inclusions in *AISI 303* reduce the hydrogen diffusivity [98] in the bulk, and therefore also reduce the brittle zone depth of *AISI 303* compared to *AISI 304L*. This assumption is based on the behavior of bulk MnS inclusions, which can act as irreversible hydrogen trap sites [96, 97], as well as nucleation sites for hydrogen-induced cracks [99, 101].

The dimples in the ductile region, but near the brittle region of *AC3*, appear to be larger than the dimples on the fracture surface of *AU1* (comparison of Figure 4.9 (C) and (F)). This is in contradiction to the results of [103–106], where the average dimple size for other austenitic stainless steels decreased or remained the same after hydrogen charging.

Comparing the brittle zone depth values with the approximated hydrogen diffusion depth profiles from Figures 4.1 and 4.2, it can be seen that each brittle zone depth is approximately the same size as the distance from the corresponding sample surface to the position containing approximately 50% of the surface hydrogen concentration. It should be noted, however, that diffusion coefficients and solubility values used for the diffusion calculation were taken from literature, and were not measured for the exact used material. Also, the diffusion model used for the calculations does not take into account the effects of hydrogen trapping. However, these effects have to be taken into account, because the depth of the brittle zone refers to the local concentration of only diffusible hydrogen atoms (*peak 1 hydrogen*), since only these actively contribute to HE [22, 23, 51]. This means that for a more precise prediction of the brittle zone depth, only the local (*peak 1 hydrogen*) content must be considered.

## 5 Summary and outlook

The aim of this thesis was to review codes and standards covering the design and dimensioning of metallic components in contact with hydrogen and to investigate and summarize the fundamentals of HE to gain knowledge of the underlying theories. In addition, several codes and standards specifying materials testing methods in hydrogen-containing atmospheres were reviewed and various steels were evaluated regarding their susceptibility to HE. In the experimental part, tensile tests, TDS measurements and fractographic analyses were performed on hydrogen charged and uncharged specimens to evaluate the HE susceptibility of *PH 13-8 Mo* and *AISI 303*.

It was found that *PH 13-8 Mo* exhibits a significant susceptibility to HE, due to the small fraction of austenite and the high strength. According to *ASME B31.12* [57], high-alloyed steels with a martensitic matrix (e.g. *PH 13-8 Mo*) are generally not recommended for components in applications involving exposure to hydrogen in any form. Austenitic stainless steels may be the most suitable steels for components in contact with hydrogen [57]. For a pronounced HE resistance, a nickel content of 12 *wt.%* or more is recommended [85]. However, due to its strength, which is lower than that of *PH 13-8 Mo*, but still exceeds the UTS limit specified in [57], detrimental non-metallic inclusions, and a nickel content below 10 %, the tested *AISI 303* specimens exhibited a significant susceptibility to HE. Diffusion calculations and fractographic analysis showed, that the hydrogen diffusion rate of *AISI 303* is orders of magnitude lower than that of *PH 13-8 Mo*. Furthermore, using TDS, it was found that *AISI 303* has a higher hydrogen solubility than *PH 13-8 Mo*.

It has been shown, that the embrittlement effect of hydrogen can be reversed by an annealing treatment of the specimens at 200 °C for several hours between hydrogen charging and tensile testing. The tensile test results of these charged & annealed specimens were similar to those of uncharged specimens. However, according to [23] annealing at this temperature is not sufficient to remove all hydrogen atoms from the specimens. This indicates that the remaining amount of hydrogen (i.e. non-diffusible hydrogen) does not contribute to the deterioration of the mechanical properties.

Owing to extensive research on HE over the last few decades, there is a solid understanding of the performance of various steels in hydrogen-containing atmospheres at temperatures in the approximate range between  $-200$  °C and  $200$  °C, as it is assumed that HE in steels is most severe within this temperature range [107]. However, there is a lack of information on the performance of steels in hydrogen-containing atmospheres at higher temperatures, which may be of interest in the future for high-temperatures processes where structural metals are in contact with hydrogen.

## 6 Bibliography

- [1] T. Lei, D. Wang, X. Yu, S. Ma, W. Zhao, C. Cui, J. Meng, S. Tao, D. Guan, *Global iron and steel plant CO<sub>2</sub> emissions and carbon-neutrality pathways*, Nature 622 (2023) 514–520.
- [2] E. Koren, C.M.H. Hagen, D. Wang, X. Lu, R. Johnsen, J. Yamabe, *Experimental comparison of gaseous and electrochemical hydrogen charging in X65 pipeline steel using the permeation technique*, Corros. Sci. 215 (2023) 111025.
- [3] Mitsubishi Heavy Industries, *How hydrogen can decarbonize the steel industry - and what it will take*, [https://en.euractiv.eu/wp-content/uploads/sites/2/infographic/Decarbonising\\_steel\\_with\\_hydrogen-infographic\\_vertical-min-1.pdf](https://en.euractiv.eu/wp-content/uploads/sites/2/infographic/Decarbonising_steel_with_hydrogen-infographic_vertical-min-1.pdf), accessed on 03.11.2023.
- [4] M. Nagumo, *Fundamentals of Hydrogen Embrittlement*, Springer Science+Business Media, Singapore, 2016.
- [5] A.A. Pisarev, in R.P. Gangloff, B.P. Somerday (eds.): *Gaseous hydrogen embrittlement of materials in energy technologies. Vol. 2: Mechanisms, modelling and future developments*, Woodhead Publishing Limited, Cambridge, 2012, pp. 1–22.
- [6] A. Staykov, J. Yamabe, B.P. Somerday, *Effect of hydrogen gas impurities on the hydrogen dissociation on iron surface*, Int. J. Quantum Chem. 114 (2014) 626–635.
- [7] E.D. Williams, *Surface steps and surface morphology: understanding macroscopic phenomena from atomic observations*, Surf. Sci. 299/300 (1994) 502–524.
- [8] J. Capelle, J. Gilgert, I. Dmytrakh, G. Pluvinage, *Sensitivity of pipelines with steel API X52 to hydrogen embrittlement*, Int. J. Hydrog. Energy 33 (2008) 7630–7641.
- [9] Y.F. Cheng, L. Niu, *Mechanism for hydrogen evolution reaction on pipeline steel in near-neutral pH solution*, Electrochem. Commun. 9 (2007) 558–562.
- [10] H.P. van Leeuwen, in R.A. Oriani, J.P. Hirth, M. Smialowski (eds.): *Hydrogen Degradation of Ferrous Alloys*, Noyes Publications, Park Ridge, 1985, pp. 16–35.
- [11] J.R.G. Da Silva, S.W. Stafford, R.B. McLellan, *The thermodynamics of the hydrogen-iron system*, J. Less Common Met. 49 (1976) 407–420.

- [12] K. Lee, M. Yuan, J. Wilcox, *Understanding Deviations in Hydrogen Solubility Predictions in Transition Metals through First-Principles Calculations*, J. Phys. Chem. C. 119 (2015) 19642–19653.
- [13] J. Xu, C. Yu, H. Lu, Y. Wang, C. Luo, G. Xu, J. Suo, *Effects of alloying elements and heat treatment on hydrogen diffusion in SCRAM steels*, J. Nucl. Mater. 516 (2019) 135–143.
- [14] A.K. Drexler, F. Konert, J. Nietzke, E. Hodžić, S. Pastore, J. Domitner, M. Rhode, C. Sommitsch, T. Böllinghaus, *Effect of Tensile Loading and Temperature on the Hydrogen Solubility of Steels at High Gas Pressure*, Steel Res. Int. (2023) 2300493.
- [15] H. Ogawa, *A Statistical–Mechanical Method to Evaluate Hydrogen Solubility in Metal*, J. Phys. Chem. C. 114 (2010) 2134–2143.
- [16] G.R. Caskey Jr., in R.A. Oriani, J.P. Hirth, M. Smailowski (eds.): *Hydrogen Degradation of Ferrous Alloys*, Noyes Publications, Park Ridge, 1985, pp. 822–862.
- [17] S.K. Dwivedi, M. Vishwakarma, *Hydrogen embrittlement in different materials: A review*, Int. J. Hydrog. Energy 43 (2018) 21603–21616.
- [18] A. Turnbull, in R.P. Gangloff, B.P. Somerday (eds.): *Gaseous hydrogen embrittlement of materials in energy technologies. Vol. 2: Mechanisms, modelling and future developments*, Woodhead Publishing Limited, Cambridge, 2012, pp. 89–124.
- [19] P. Kedzierzawski, in R.A. Oriani, J.P. Hirth, M. Smailowski (eds.): *Hydrogen Degradation of Ferrous Alloys*, Noyes Publications, Park Ridge, 1985, pp. 251–268.
- [20] T.T. Fang, M.I. Chen, W.D. Hsu, *Insight into understanding the jump frequency of diffusion in solids*, AIP Adv. 10 (2020) 065132.
- [21] M. Koyama, M. Rohwerder, C.C. Tasan, A. Bashir, E. Akiyama, K. Takai, D. Raabe, K. Tsuzaki, *Recent progress in microstructural hydrogen mapping in steels: quantification, kinetic analysis, and multi-scale characterisation*, Mater. Sci. Technol. 33 (2017) 1481–1496.
- [22] M. Nagumo, K. Takai, *The predominant role of strain-induced vacancies in hydrogen embrittlement of steels: Overview*, Acta Mater. 165 (2019) 722–733.
- [23] K. Takai, R. Watanuki, *Hydrogen in Trapping States Innocuous to Environmental Degradation of High-strength Steels*, ISIJ Int. 43 (2003) 520–526.

- [24] M.R. Louthan Jr., *Hydrogen Embrittlement of Metals: A Primer for the Failure Analyst*, J. Fail. Anal. Prev. 8 (2008) 289–307.
- [25] S. Lynch, *Hydrogen embrittlement phenomena and mechanisms*, Corros. Rev. 30 (2012) 105–123.
- [26] N.E. Nanninga, Y.S. Levy, E.S. Drexler, R.T. Condon, A.E. Stevenson, A.J. Slifka, *Comparison of hydrogen embrittlement in three pipeline steels in high pressure gaseous hydrogen environments*, Corros. Sci. 59 (2012) 1–9.
- [27] Z. Wang, J. Liu, F. Huang, Y.J. Bi, S.Q. Zhang, *Hydrogen Diffusion and Its Effect on Hydrogen Embrittlement in DP Steels With Different Martensite Content*, Front. Mater. Sci. 7 (2020) 620000.
- [28] M. Loidl, O. Kolk, S. Veith, T. Göbel, *Characterization of hydrogen embrittlement in automotive advanced high strength steels*, Mater. Werkst. 42 (2011) 1105–1110.
- [29] X. Li, J. Zhang, J. Chen, S. Shen, G. Yang, T. Wang, X. Song, *Effect of aging treatment on hydrogen embrittlement of PH 13-8 Mo martensite stainless steel*, Mater. Sci. Eng. A 651 (2016) 474–485.
- [30] X. Li, J. Zhang, Y. Wang, S. Shen, X. Song, *Effect of hydrogen on tensile properties and fracture behavior of PH 13-8 Mo steel*, Mater. Des. 108 (2016) 608–617.
- [31] Y. Wang, X. Wang, J. Gong, L. Shen, W. Dong, *Hydrogen embrittlement of cathodically hydrogen-precharged 304L austenitic stainless steel: Effect of plastic pre-strain*, Int. J. Hydrog. Energy 39 (2014) 13909–13918.
- [32] E. Quadrini, *Study of the effect of heat treatment on hydrogen embrittlement of AISI 4340 steel*, J. Mater. Sci. 24 (1989) 915–920.
- [33] J. Venezuela, Q. Liu, M. Zhang, Q. Zhou, A. Atrens, *A review of hydrogen embrittlement of martensitic advanced high-strength steels*, Corros. Rev. 34 (2016) 153–186.
- [34] M.M.H. Bhuiya, A. Kumar, K.J. Kim, *Metal hydrides in engineering systems, processes, and devices: A review of non-storage applications*, Int. J. Hydrog. Energy 40 (2015) 2231–2247.
- [35] F. Dong, J. Venezuela, H. Li, Z. Shi, Q. Zhou, L. Chen, J. Chen, L. Du, A. Atrens, *Enhancement of hydrogen embrittlement resistance in a Fe-18Mn-0.6C twinning induced plasticity steel by copper alloying*, Acta Mater. 254 (2023) 118888.



- [36] M.B. Djukic, G.M. Bakic, V. Sijacki-Zeravcic, A. Sedmak, B. Rajcic, *The synergistic action and interplay of hydrogen embrittlement mechanisms in steels and iron: Localized plasticity and decohesion*, Eng. Fract. Mech. 216 (2019) 106528.
- [37] K.N. Solanki, D.K. Ward, D.J. Bammann, *A Nanoscale Study of Dislocation Nucleation at the Crack Tip in the Nickel-Hydrogen System*, Metall. Mater. Trans. A 42 (2011) 340–347.
- [38] R. Matsumoto, S. Seki, S. Taketomi, N. Miyazaki, *Hydrogen-related phenomena due to decreases in lattice defect energies—Molecular dynamics simulations using the embedded atom method potential with pseudo-hydrogen effects*, Comput. Mater. Sci. 92 (2014) 362–371.
- [39] A.R. Troiano, *The Role of Hydrogen and Other Interstitials in the Mechanical Behavior of Metals*, Metallogr. Microstruct. Anal. 5 (2016) 557–569.
- [40] A.S. Kholobina, W. Ecker, R. Pippan, V.I. Razumovskiy, *Effect of alloying elements on hydrogen enhanced decohesion in bcc iron*, Comput. Mater. Sci. 188 (2021) 110215.
- [41] C.D. Beachem, *A new model for hydrogen-assisted cracking (hydrogen embrittlement)*, Metall. Mater. Trans. B 3 (1972) 441–455.
- [42] P. Yu, Y. Cui, G.Z. Zhu, Y. Shen, M. Wen, *The key role played by dislocation core radius and energy in hydrogen interaction with dislocations*, Acta Mater. 185 (2020) 518–527.
- [43] M. Itakura, H. Kaburaki, M. Yamaguchi, T. Okita, *The effect of hydrogen atoms on the screw dislocation mobility in bcc iron: A first-principles study*, Acta Mater. 61 (2013) 6857–6867.
- [44] S. Lynch, *Environmentally assisted cracking: Overview of evidence for an adsorption-induced localised-slip process*, Acta Metall. 36 (1988) 2639–2661.
- [45] R. Kirchheim, *Reducing grain boundary, dislocation line and vacancy formation energies by solute segregation. I. Theoretical background*, Acta Mater. 55 (2007) 5129–5138.
- [46] A. Ilyushechkin, L. Schoeman, L. Carter, S.S. Hla, *Material Challenges and Hydrogen Embrittlement Assessment for Hydrogen Utilisation in Industrial Scale*, Hydrogen 4 (2023) 599–619.

- [47] A. Zafra, G. Álvarez, G. Benoit, G. Henaff, E. Martinez-Pañeda, C. Rodríguez, J. Belzunce, *Hydrogen-assisted fatigue crack growth: Pre-charging vs in-situ testing in gaseous environments*, Mater. Sci. Eng. A 871 (2023) 144885.
- [48] J.H. Holbrook, H.J. Cialone, E.W. Collings, E.J. Drauglis, P.M. Scott, M.E. Mayfield, in R.P. Gangloff, B.P. Somerday (eds.): *Gaseous hydrogen embrittlement of materials in energy technologies. Vol. 2: Mechanisms, modelling and future developments*, Woodhead Publishing Limited, Cambridge, 2012, pp. 129–153.
- [49] T. Michler, I.E. Boitsov, I.L. Malkov, A.A. Yukhimchuk, J. Naumann, *Assessing the effect of low oxygen concentrations in gaseous hydrogen embrittlement of DIN 1.4301 and 1.1200 steels at high gas pressures*, Corros. Sci. 65 (2012) 169–177.
- [50] C. Fischer, S. Fliegner, H. Oesterlin, T. Michler, S. Höhler, A. Mondry, P. La Ertault de Bretonniere, *Codes and standards for the fatigue-based design of hydrogen infrastructure components*, Int. J. Fatigue 171 (2023) 107564.
- [51] T. Doshida, K. Takai, *Dependence of hydrogen-induced lattice defects and hydrogen embrittlement of cold-drawn pearlitic steels on hydrogen trap state, temperature, strain rate and hydrogen content*, Acta Mater. 79 (2014) 93–107.
- [52] W.G. Clark Jr., *Effect of temperature and pressure on hydrogen cracking in high strength type 4340 steel*, J. Mater. Energy Sys. 1 (1979) 33–40.
- [53] S.J. Park, M.K. Seo, *Interface Science and Composites*, Academic Press, Amsterdam, 2011.
- [54] K. Kussmaul, *Fracture mechanical behaviour of the steel 15 MnNi 6 3 in argon and in high pressure hydrogen gas with admixtures of oxygen*, Int. J. Hydrog. Energy 23 (1998) 577–582.
- [55] Y. Murakami, H. Matsunaga, *The effect of hydrogen on fatigue properties of steels used for fuel cell system*, Int. J. Fatigue 28 (2006) 1509–1520.
- [56] M. Nagumo, H. Shimura, T. Chaya, H. Hayashi, I. Ochiai, *Fatigue damage and its interaction with hydrogen in martensitic steels*, Mater. Sci. Eng. A 348 (2003) 192–200.
- [57] American Society of Mechanical Engineers, B31.12, *Hydrogen Piping and Pipelines*, 2011.



- [58] American Society of Mechanical Engineers, BPVC Section VIII, *Rules for Construction of Pressure Vessels Division 3 - Alternative Rules for Construction of High Pressure Vessels*, 2021.
- [59] Deutsches Institut für Normung e.V., DIN AD 2000 - Bulletin S2, *Richtlinie über Druckgeräte - Berechnung auf Wechselbeanspruchung*, 2016.
- [60] ASTM International, ASTM G142-98, *Test Method for Determination of Susceptibility of Metals to Embrittlement in Hydrogen Containing Environments at High Pressure, High Temperature, or Both*, 2016.
- [61] International Organization for Standardization, ISO 11114-4:2017, *Transportable gas cylinders - Compatibility of cylinder and valve materials with gas contents - Part 4: Test methods for selecting steels resistant to hydrogen embrittlement*, 2017.
- [62] CSA Group, ANSI/CSA CHMC 1-2014:2014-02-01, *Test methods for evaluating material compatibility in compressed hydrogen applications - Metals*, 2014.
- [63] G.B. Rawls, T. Adams, N.L. Newhouse, in R.P. Gangloff, B.P. Somerday (eds.): *Gaseous hydrogen embrittlement of materials in energy technologies. Vol. 1: The problem, its characterisation and effect on particular alloy classes*, Woodhead Publishing Limited, Cambridge, 2012, pp. 1–48.
- [64] K. Poorhaydari, *A Comprehensive Examination of High-Temperature Hydrogen Attack—A Review of over a Century of Investigations*, J. Mater. Eng. Perform. 30 (2021) 7875–7908.
- [65] S. Pillot, L. Coudreuse, in R.P. Gangloff, B.P. Somerday (eds.): *Gaseous hydrogen embrittlement of materials in energy technologies. Vol. 1: The problem, its characterisation and effect on particular alloy classes*, Woodhead Publishing Limited, Cambridge, 2012, pp. 51–93.
- [66] Deutsches Institut für Normung e.V., WL 1.4534-1:2012-10, *Aerospace series - High-strength precipitation-hardening stainless chromium-nickel-molybdenum-aluminium steel with approx. 0,04 C - 13 Cr - 8 Ni - 2,2 Mo - 1 Al - Part 1: Bars and forgings*, 2012.
- [67] Deutsches Institut für Normung e.V., DIN EN 10088-3:2014-12, *Stainless steels - Part 3: Technical delivery conditions for semi-finished products, bars, rods, wire, sections and bright products of corrosion resisting steels for general purposes*, 2014.

- [68] Deutsches Institut für Normung e.V., DIN EN 10027-1:2017-01, *Designation systems for steels - Part 1: Steel names*, 2017.
- [69] S. Zeisl, A. Landefeld, N. van Steenberge, Y. Chang, R. Schnitzer, *The role of alloying elements in NiAl and Ni<sub>3</sub>Ti strengthened Co-free maraging steels*, Mater. Sci. Eng. A 861 (2022) 144313.
- [70] R. Schnitzer, R. Radis, M. Nöhner, M. Schober, R. Hochfellner, S. Zinner, E. Povoden-Karadeniz, E. Kozeschnik, H. Leitner, *Reverted austenite in PH 13-8 Mo maraging steels*, Mater. Chem. Phys. 122 (2010) 138–145.
- [71] W. Sha, Z. Guo, *Maraging steels*, Woodhead Publishing Limited, Cambridge, 2009.
- [72] J.P. Yuan, D.D. Chen, H.R. Bo, *Nickel Release Rate of Type 303 Free Cutting Austenitic Stainless Steel*, Adv. Mater. Res. 1096 (2015) 114–119.
- [73] H. Wang, Z. Shi, X. Yaer, Z. Tong, Z. Du, *High mechanical performance of AISI304 stainless steel plate by surface nanocrystallization and microstructural evolution during the explosive impact treatment*, J. Mater. Res. Technol. 8 (2019) 609–614.
- [74] P. Shewmon, *Diffusion in Solids*, Second Edition, Wiley-TMS, New Jersey, 1991.
- [75] Y.F. Li, L.M. Zhao, H.L. Pan, *Hydrogen permeation behaviour and associated phase transformations in annealed AISI304 stainless steels*, Mater. Struct. 46 (2013) 621–627.
- [76] L.W. Tsay, M.Y. Chi, H.R. Chen, C. Chen, *Investigation of hydrogen sulfide stress corrosion cracking of PH 13-8 Mo stainless steel*, Mater. Sci. Eng. A 416 (2006) 155–160.
- [77] T.P. Perng, C.J. Altstetter, *Effects of deformation on hydrogen permeation in austenitic stainless steels*, Acta Metall. 34 (1986) 1771–1781.
- [78] G. Hinds, J. Zhao, A.J. Griffiths, A. Turnbull, *Hydrogen Diffusion in Super 13% Chromium Martensitic Stainless Steel*, Corrosion 61 (2005) 348–354.
- [79] Deutsches Institut für Normung e.V., DIN 50125:2022-08, *Testing of metallic materials - Tensile test pieces*, 2022.
- [80] A. Rosenauer, D. Brandl, G. Ressel, S. Lukas, S. Monschein, M. Stockinger, R. Schnitzer, *Influence of delta ferrite on the impact toughness of a PH 13-8 Mo maraging steel*, Mater. Sci. Eng. A 856 (2022) 144024.

- [81] ASTM International, ASTM A370-20, *Test Methods and Definitions for Mechanical Testing of Steel Products*, 2020.
- [82] N. Ehrlin, C. Bjerkén, M. Fisk, *Cathodic hydrogen charging of Inconel 718*, AIMS Mater. Sci. 3 (2016) 1350–1364.
- [83] International Organization for Standardization, ISO 6892-1:2009, *Metallic materials - Tensile testing - Part 1: Method of test at room temperature*, 2009.
- [84] K. Verbeken, in R.P. Gangloff, B.P. Somerday (eds.): *Gaseous hydrogen embrittlement of materials in energy technologies. Vol. 2: Mechanisms, modelling and future developments*, Woodhead Publishing Limited, Cambridge, 2012, pp. 27–50.
- [85] M. Martin, S. Weber, W. Theisen, T. Michler, J. Naumann, *Effect of alloying elements on hydrogen environment embrittlement of AISI type 304 austenitic stainless steel*, Int. J. Hydrog. Energy 36 (2011) 15888–15898.
- [86] Y. Wang, X. Wu, X. Li, W. Wu, J. Gong, *Combined effects of prior plastic deformation and sensitization on hydrogen embrittlement of 304 austenitic stainless steel*, Int. J. Hydrog. Energy 44 (2019) 7014–7031.
- [87] C. Zhou, Y. Song, Q. Shi, S. Hu, J. Zheng, P. Xu, L. Zhang, *Effect of pre-strain on hydrogen embrittlement of metastable austenitic stainless steel under different hydrogen conditions*, Int. J. Hydrog. Energy 44 (2019) 26036–26048.
- [88] H.Y. Zhang, L.W. Zheng, T. Wang, W.J. Lv, Q.X. Shi, J.Y. Ma, Y. Luo, W. Liang, J. Hu, R. Misra, *Interrelationship between hydrogen and alpha-prime-martensite of SUS 304 austenitic stainless steel revealed by tensile tests*, Mater. Sci. Eng. A 831 (2022) 142169.
- [89] D.P. Abraham, C.J. Altstetter, *The effect of hydrogen on the yield and flow stress of an austenitic stainless steel*, Metall. Mater. Trans. A 26 (1995) 2849–2858.
- [90] L. Tan, D. Li, L. Yan, X. Pang, K. Gao, *A novel heat treatment for improving the hydrogen embrittlement resistance of a precipitation-hardened martensitic stainless steel*, Corros. Sci. 206 (2022) 110530.
- [91] E. Astafurova, A. Fortuna, E. Melnikov, S. Astafurov, *The Effect of Strain Rate on Hydrogen-Assisted Deformation Behavior and Microstructure in AISI 316L Austenitic Stainless Steel*, Materials 16 (2023) 2983.

- [92] Y.S. Kim, S.H. Bak, S.S. Kim, *Effect of Strain-Induced Martensite on Tensile Properties and Hydrogen Embrittlement of 304 Stainless Steel*, Metall. Mater. Trans. A 47 (2016) 222–230.
- [93] M. De Freitas, L. Reis, B. Li, *Comparative study on biaxial low-cycle fatigue behaviour of three structural steels*, Fatigue Fract. Eng. Mat. Struct. 29 (2006) 992–999.
- [94] L. Zhang, M. Imade, B. An, M. Wen, T. Iijima, S. Fukuyama, K. Yokogawa, *Internal Reversible Hydrogen Embrittlement of Austenitic Stainless Steels Based on Type 316 at Low Temperatures*, ISIJ Int. 52 (2012) 240–246.
- [95] G. Han, J. He, S. Fukuyama, K. Yokogawa, *Effect of strain-induced martensite on hydrogen environment embrittlement of sensitized austenitic stainless steels at low temperatures*, Acta Mater. 46 (1998) 4559–4570.
- [96] M.A. Mohtadi-Bonab, M. Eskandari, *A focus on different factors affecting hydrogen induced cracking in oil and natural gas pipeline steel*, Eng. Fail. Anal. 79 (2017) 351–360.
- [97] M. Garet, A. Brass, C. Haut, F. Gutierrez-Solana, *Hydrogen trapping on non metallic inclusions in cr-mo low alloy steels*, Corros. Sci. 40 (1998) 1073–1086.
- [98] Z. Szklarska-Smialowska, E. Lunarska, *The effect of sulfide inclusions on the susceptibility of steels to pitting, stress corrosion cracking and hydrogen embrittlement*, Werkst. Korros. 32 (1981) 478–485.
- [99] G. Ghosh, P. Rostron, R. Garg, A. Panday, *Hydrogen induced cracking of pipeline and pressure vessel steels: A review*, Eng. Fract. Mech. 199 (2018) 609–618.
- [100] A.J. Haq, K. Muzaka, D.P. Dunne, A. Calka, E.V. Pereloma, *Effect of microstructure and composition on hydrogen permeation in X70 pipeline steels*, Int. J. Hydrog. Energy 38 (2013) 2544–2556.
- [101] E. Miyoshi, T. Tanaka, F. Terasaki, A. Ikeda, *Hydrogen-Induced Cracking of Steels Under Wet Hydrogen Sulfide Environment*, J. Eng. Ind. 98 (1976) 1221–1230.
- [102] V. Shubina Helbert, A. Nazarov, F. Vucko, S. Rioual, D. Thierry, *Hydrogen effect on the passivation and crevice corrosion initiation of AISI 304L using Scanning Kelvin Probe*, Corros. Sci. 182 (2021) 109225.

- [103] A.W. Thompson, *The behavior of sensitized 309S stainless steel in hydrogen*, Mater. Sci. Eng. 14 (1974) 253–264.
- [104] T. Matsuo, J. Yamabe, S. Matsuoka, *Effects of hydrogen on tensile properties and fracture surface morphologies of Type 316L stainless steel*, Int. J. Hydrog. Energy 39 (2014) 3542–3551.
- [105] G.P. Tiwari, A. Bose, J.K. Chakravartty, S.L. Wadekar, M.K. Totlani, R.N. Arya, R.K. Fotedar, *A study of internal hydrogen embrittlement of steels*, Mater. Sci. Eng. A 286 (2000) 269–281.
- [106] C. San Marchi, B.P. Somerday, X. Tang, G.H. Schiroky, *Effects of alloy composition and strain hardening on tensile fracture of hydrogen-precharged type 316 stainless steels*, Int. J. Hydrog. Energy 33 (2008) 889–904.
- [107] T. Michler, F. Schweizer, K. Wackermann, *Review on the Influence of Temperature upon Hydrogen Effects in Structural Alloys*, Metals 11 (2021) 423.

# List of Figures

1.1	Principle of the hydrogen usage in a carbon-dioxide-free steel production [3].	1
2.1	Hydrogen solubility as a function of temperature for various pure metals in equilibrium with 0.1 MPa hydrogen gas [4]. . . . .	7
2.2	Hydrogen solubility as a function of temperature for different steels [4]. . .	7
2.3	Hydrogen diffusion coefficients in iron and different austenitic steels [4]. . .	10
2.4	A variety of possible hydrogen trap sites in metals [21]. . . . .	11
2.5	<b>Left:</b> Hydrogen release temperatures of different trap sites in pure iron [4]. <b>Right:</b> Characteristic hydrogen desorption peaks for diffusible hydrogen ( <i>peak 1 hydrogen</i> ) and non-diffusible hydrogen ( <i>peak 2 hydrogen</i> ) in a cold-drawn eutectoid steel [23]. . . . .	12
2.6	Tensile stress-strain curves of X52, X65, and X100 pipeline steels (data from Nanninga et al. [26]). . . . .	13
2.7	HEI as a function of the martensite content of a dual-phase steel [27]. . . .	14
2.8	Necessary requirements for HE. . . . .	15
2.9	Hydrogen content of different iron samples that were strained before charging [strain] or that were pre-charged, strained, and then charged [H+strain] [22]. . . . .	19
2.10	<b>Left:</b> Stress-strain curves from tensile tests of lower-bainitic steel specimens with different hydrogen pre-charging times. <b>Right:</b> Hydrogen content over charging time for these specimens [23]. . . . .	21
2.11	<b>Left:</b> Stress-strain curves from tensile tests of cold-drawn lower-bainitic steel specimens with different hydrogen pre-charging times after annealing at 200 °C. <b>Right:</b> Hydrogen content over charging time for these specimens after annealing at 200 °C [23]. . . . .	22
2.12	Influence of temperature ( <b>left</b> ) and strain rate ( <b>right</b> ) on the relative ROA measured in tensile tests [51]. . . . .	23
2.13	$K_{th}$ as a function of hydrogen pressure for various <i>AISI 4340</i> steel samples with different yield strengths [4]. . . . .	25
2.14	J-Integral as a function of crack growth for a <i>15MnNi6-3</i> steel in different atmospheres (data from Kussmaul et al. [54]). . . . .	26
2.15	S-N curve for a Si-Cr martensitic steel measured for rotational bending fatigue with and without ex-situ hydrogen charging, the arrows indicate that there was no failure [4]. . . . .	27

2.16	Crack growth rate for fatigue tests conducted on <i>X42</i> steel specimens in different environments [48]. . . . .	28
2.17	Exemplary table for the determination of HMPF for carbon steel pipes [57].	32
2.18	Gaseous and liquid hydrogen compatibility of various material classes [57].	33
2.19	Nelson curves for Cr-Mo and carbon steels [65]. . . . .	34
2.20	Lifetime assessment flowchart for welded and non-welded steel bottles and pressure vessels according to AD 2000 bulletin S2 [59]. . . . .	37
3.1	The geometry used for the <i>AISI 303</i> tensile specimens (measures are in mm) [79]. . . . .	45
3.2	Schematic drawing of the location where the <i>PH 13-8 Mo</i> cylindrical specimen were taken from a rolled round bar with a diameter of 90 mm. . .	45
3.3	The geometry used for the <i>PH 13-8 Mo</i> tensile specimens [81]. . . . .	45
3.4	Schematic drawing of the hydrogen charging process. . . . .	47
3.5	Schematic representation of the functional principle of a TDS measurement [84]. . . . .	50
4.1	Estimated hydrogen diffusion depth of <i>AISI 303</i> specimens for various charging times at 20 °C ( <b>top</b> ) and 50 °C ( <b>bottom</b> ), the arrow indicates the charging duration used in this thesis. . . . .	51
4.2	Estimated hydrogen diffusion depth of <i>PH 13-8 Mo</i> specimens for various charging times at 20 °C ( <b>top</b> ) and 50 °C ( <b>bottom</b> ), the arrow indicates the charging duration used in this thesis. . . . .	52
4.3	Exemplary microstructure of (A) <i>PH 13-8 Mo</i> and (B) <i>AISI 303</i> after etching (A) with <i>V2A-Beize</i> and (B) according to <i>Beraha II</i> . The arrows indicate elongated (A) delta ferrite grains and (B) MnS inclusions. . . . .	54
4.4	Stress-strain curves from tensile tests of uncharged (MU), charged (MC) as well as charged & annealed (MCA) PH 13-8 Mo tensile specimens. . . .	55
4.5	Stress-strain curves from tensile tests of uncharged (AU), charged (AC) as well as charged & annealed (ACA) AISI 303 tensile specimens. . . . .	55
4.6	Top and side view of the fracture surfaces of the MU2 ( <b>top</b> ), MC3 ( <b>middle</b> ) and MCA ( <b>bottom</b> ) specimens. . . . .	63
4.7	Top and side view of the fracture surfaces of the AU1 ( <b>top</b> ), AC3 ( <b>middle</b> ) and ACA1 ( <b>bottom</b> ) specimens. . . . .	64
4.8	Fracture surfaces of the <i>PH 13-8 Mo</i> specimens MU2 (A-C) and MC1 (D-F), the red squares indicate where the respective magnified area below is located. . . . .	66

4.9	Fracture surfaces of the <i>AISI 303</i> specimens AU1 (A-C) and AC3 (D-F), the red squares indicate where the respective magnified area below is located.	67
A.1	Corrosive attack on an <i>AISI 303</i> specimen charged for 90 h at 1 mA/cm <sup>2</sup> in the sulfuric acid electrolyte according to Table 3.3.	xv
A.2	Hydrogen desorption rate as a function of temperature for the TDS measurements of the <i>PH 13-8 Mo</i> specimens.	xvii
A.3	Hydrogen desorption rate as a function of temperature for the TDS measurements of the <i>AISI 303</i> specimens.	xvii
A.4	Fracture surfaces of the MC2 (A-C) and MCA (D-F) specimens, the red squares indicate where the respective magnified area below is located.	xviii
A.5	Fracture surfaces of a charged, but invalid specimen, which is not listed in Table 3.2 (A-C) and the ACA2 specimen (D-F), the red squares indicate where the respective magnified area below is located.	xix
A.6	Surface cracks on the lateral surface of the MC2 specimen as overview ( <b>top</b> ) and in detail ( <b>bottom</b> ).	xx



# List of Tables

2.1	Overview of the materials, approaches, test methods and parameters covered by the codes and standards in this chapter [50, 57, 59–62]. . . . .	30
3.1	Chemical compositions of the investigated alloys in mass percentages [66, 67].	42
3.2	Specimen assignment to the applied condition/measurement. . . . .	46
3.3	Hydrogen charging parameters and electrolyte compositions. . . . .	48
4.1	Estimated hydrogen solubility ( $S$ ) at room temperature, as well as hydrogen diffusivity at 20 °C ( $D_{20}$ ) and 50 °C ( $D_{50}$ ), with a color code to visualize the influence of each property on the HE resistance of the materials [75–78]. . . . .	52
4.2	Mean, $\mu$ , and standard deviation, $\sigma$ , of EAF, ROA, UTS, and $Rp_{0.2}$ of the charged (C) and uncharged (U) samples and the individual values of the charged & annealed (CA) samples. . . . .	57
4.3	$HEI_{\delta}$ and $HEI_{\phi}$ of all charged (C) specimens, including mean, $\mu$ , and standard deviation, $\sigma$ , values. . . . .	57
4.4	Total amount of hydrogen measured in the TDS samples. . . . .	61
A.1	EAF, ROA, UTS, and $Rp_{0.2}$ of the charged (C), uncharged (U), and charged & annealed (CA) PH 13-8 Mo (M) and AISI 303 (A) tensile specimens. . . .	xvi

# Appendix

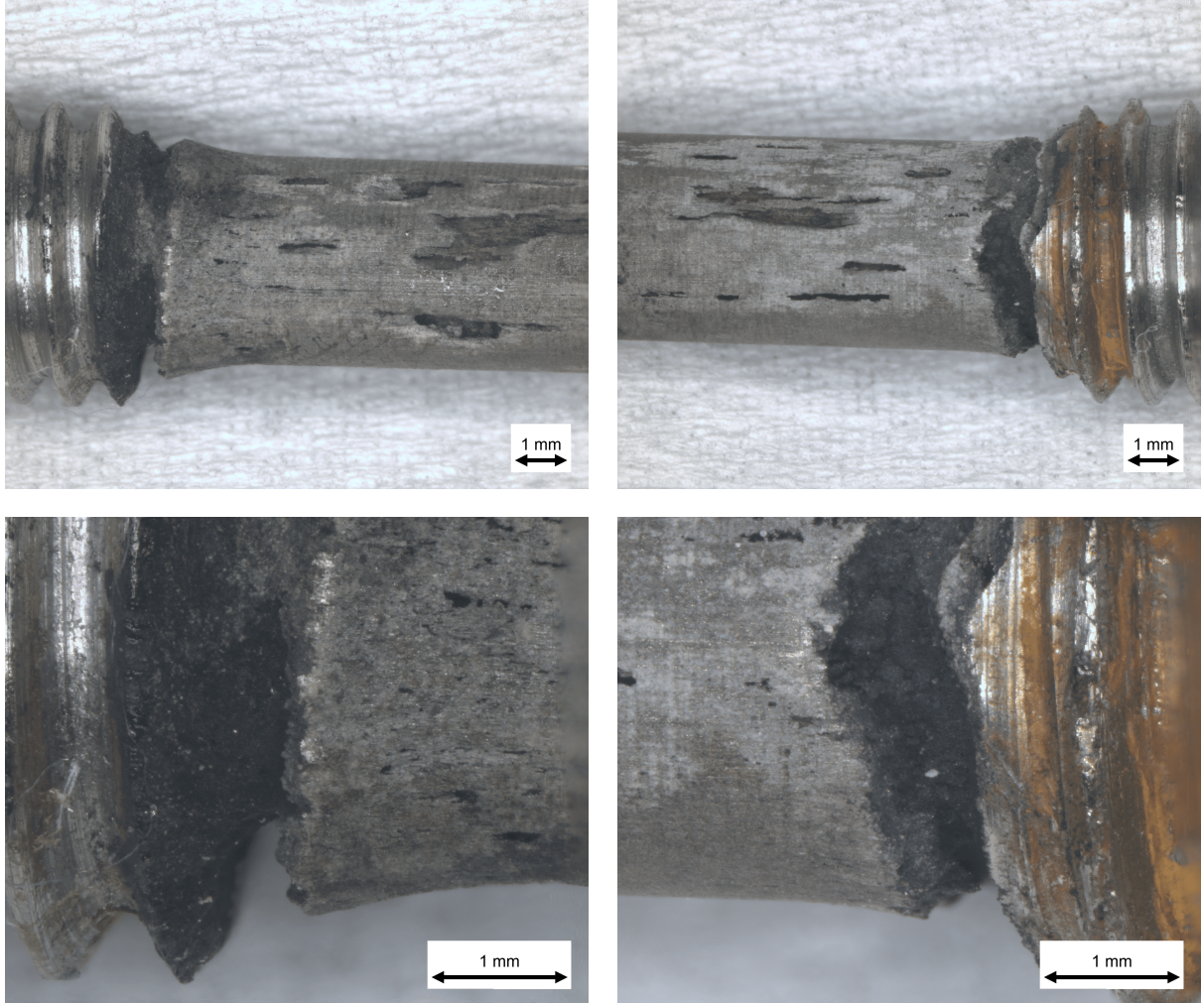


**Figure A.1:** Corrosive attack on an *AISI 303* specimen charged for 90 h at  $1 \text{ mA/cm}^2$  in the sulfuric acid electrolyte according to Table 3.3.

**Table A.1:** EAF, ROA, UTS, and  $R_{p0.2}$  of the charged (C), uncharged (U), and charged & annealed (CA) PH 13-8 Mo (M) and AISI 303 (A) tensile specimens.

Sample	EAF [%]	ROA [%]	UTS [MPa]	$R_{p0.2}$ [MPa]
MU1	14.18	66.61	1399	1367
MU2	14.01	67.69	1408	1373
MU3	14.64	68.04	1391	1346
MC1	6.359	9.520	1408	1371
MC2	10.42	45.93	1405	1371
MC3	10.54	46.46	1410	1385
MC4	12.48	58.14	1397	1371
MCA	14.07	67.61	1398	1372

Sample	EAF [%]	ROA [%]	UTS [MPa]	$R_{p0.2}$ [MPa]
AU1	50.11	57.35	809.8	497.5
AU2	50.92	59.17	826.0	521.9
AU3	49.84	56.72	818.1	522.3
AC1	37.65	29.51	797.5	512.6
AC2	38.57	32.08	795.4	544.8
AC3	40.23	33.36	803.7	521.8
AC4	38.23	30.45	804.5	475.8
ACA1	50.68	60.13	818.5	558.8
ACA2	47.45	50.04	823.6	571.5

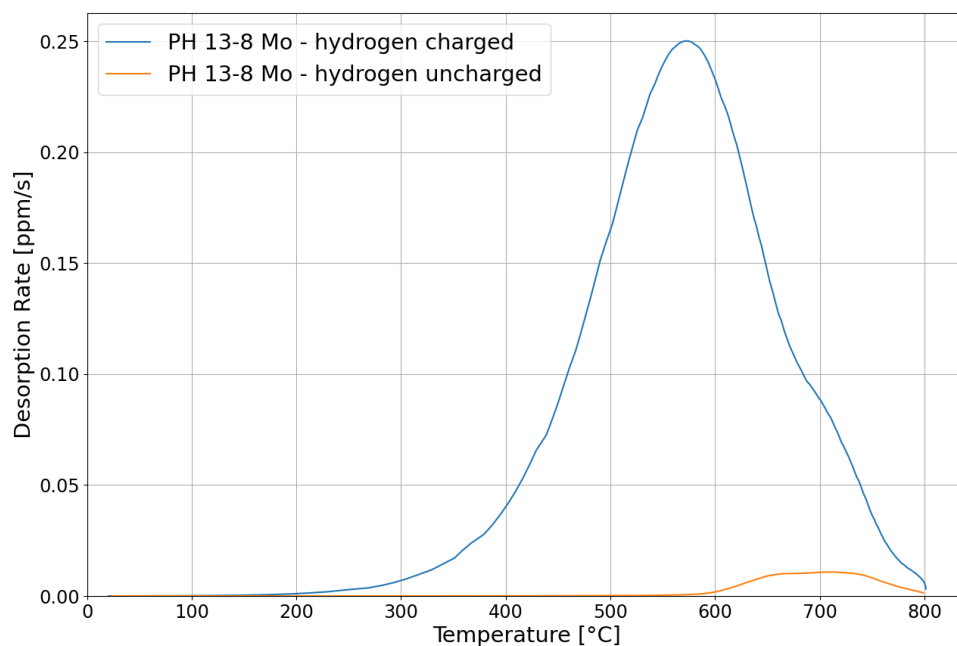


**Figure A.2:** Hydrogen desorption rate as a function of temperature for the TDS measurements of the *PH 13-8 Mo* specimens.

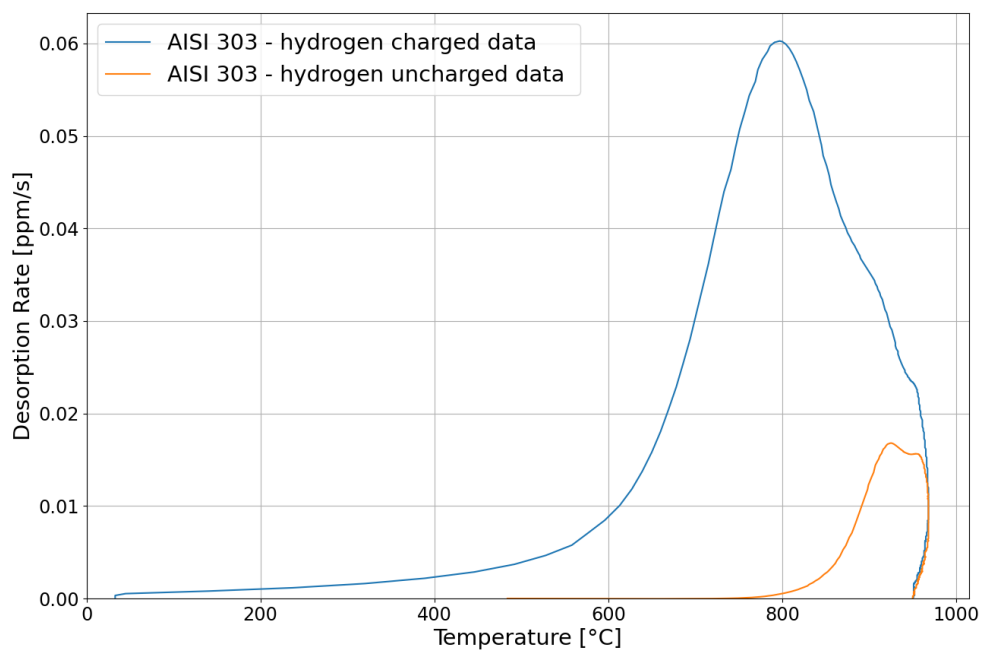


**Figure A.3:** Hydrogen desorption rate as a function of temperature for the TDS measurements of the *AISI 303* specimens.



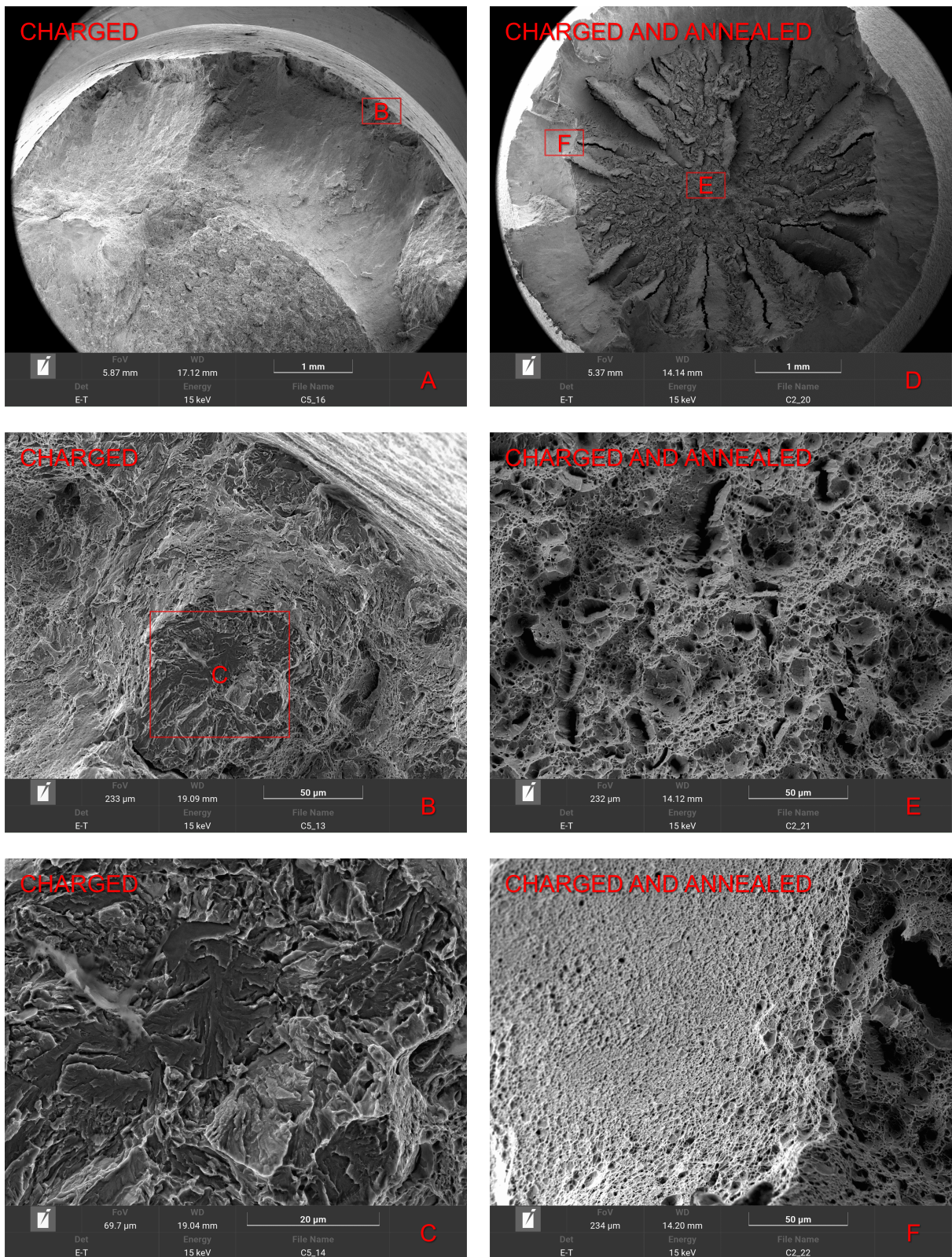


**Figure A.4:** Fracture surfaces of the MC2 (A-C) and MCA (D-F) specimens, the red squares indicate where the respective magnified area below is located.



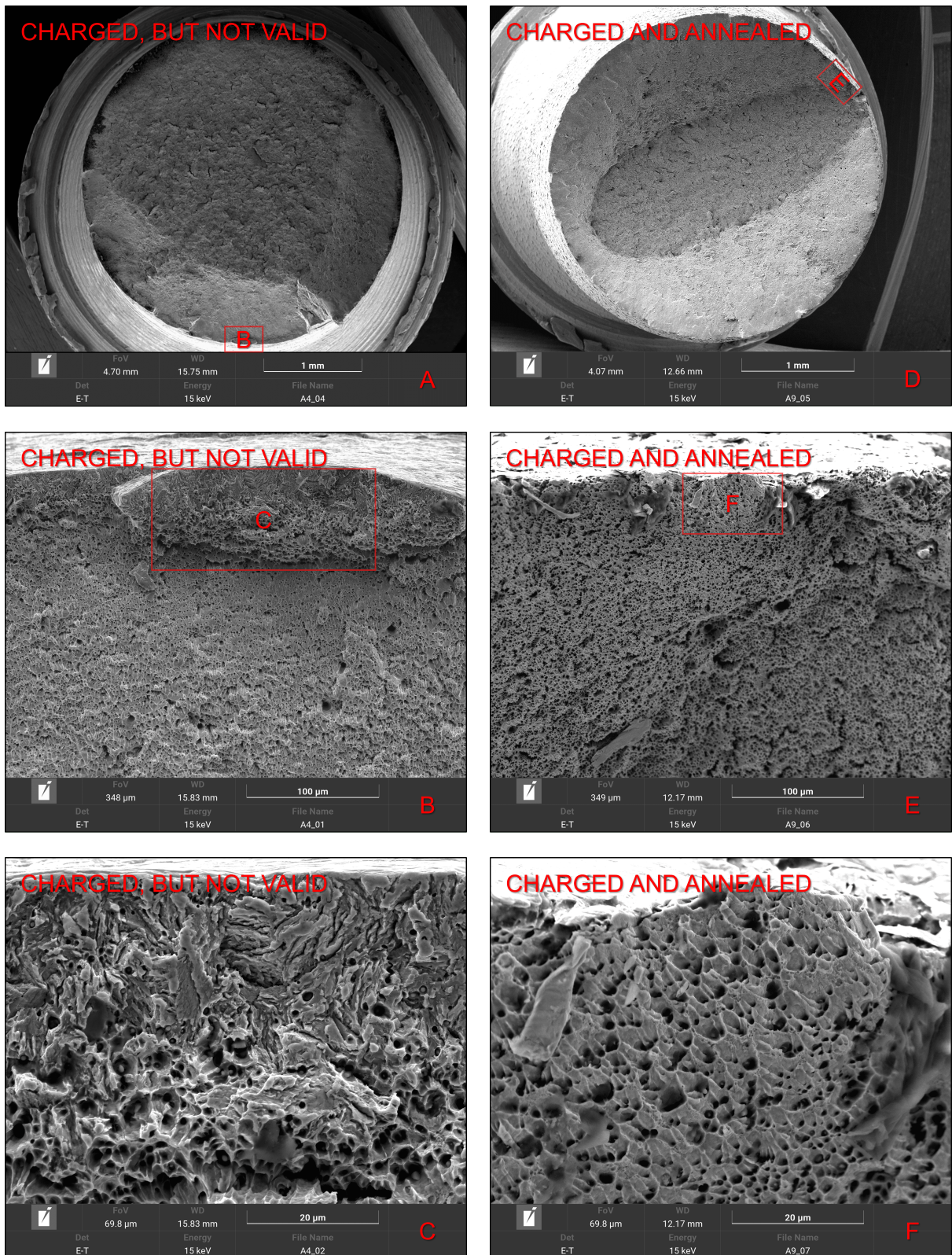


**Figure A.5:** Fracture surfaces of a charged, but invalid specimen, which is not listed in Table 3.2 (A-C) and the ACA2 specimen (D-F), the red squares indicate where the respective magnified area below is located.



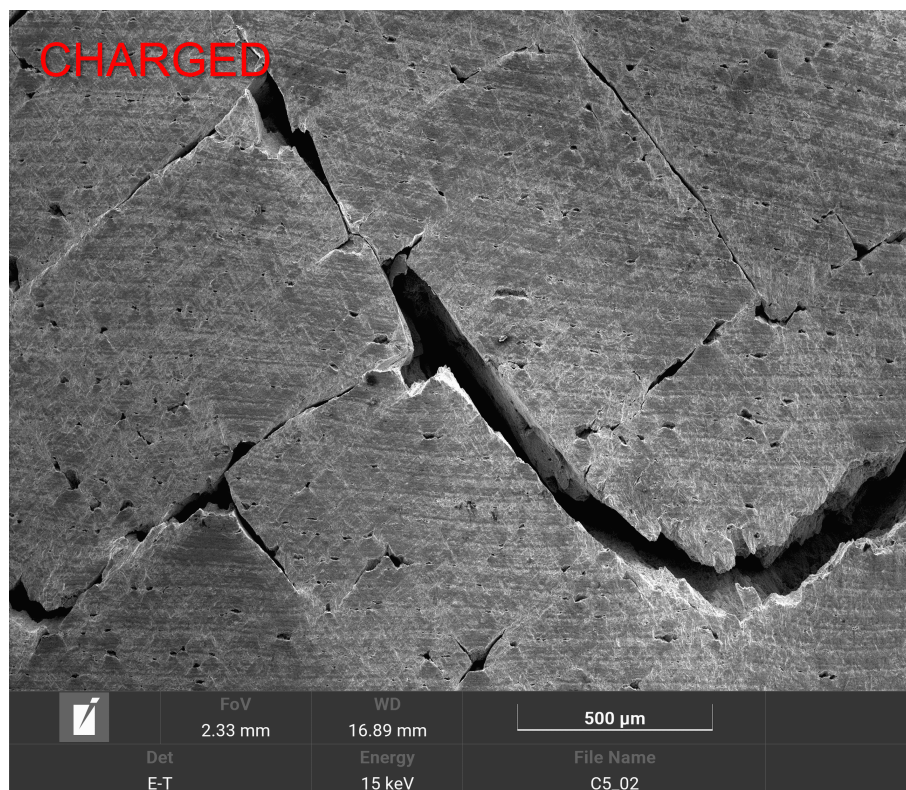
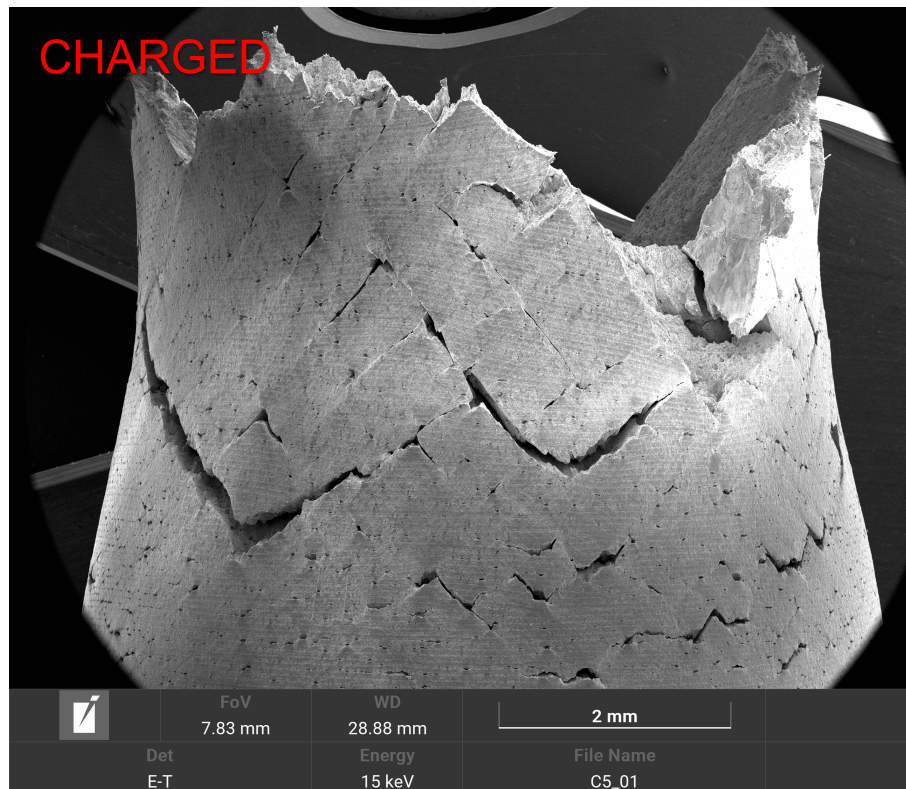


**Figure A.6:** Surface cracks on the lateral surface of the MC2 specimen as overview (**top**) and in detail (**bottom**).